united nations
educational, scientific
and cultural
organization

international atomic
energy agency

the
abdus salam
international centre for theoretical physics

SMR/1108 - 22

COURSE ON "MEDITERRANEAN SEA(S) CIRCULATION & ECOSYSTEM FUNCTIONING" 2 - 20 November 1998

Trieste, Italy

"Principles of Ecosystem Dynamics and Modeling"

T. OGUZ
Institute of Marine Sciences
Middle East Technical University
Erdemli, Icel
Turkey

Lecture Series on the Principals of Ecosystem Dynamics and Modeling

16-17 November 1998

Contents

CHAPTER 5. Vertically- Resolved Coupled-Physical-Biological Models.

1. Basic Ecological Concepts

1.1 Classification of Marine Environments and Marine Organisms

Marine environment can be separated into two basic regions as "pelagic" and "benthic" environments. The **pelagic environment** covers the biological life within the water column from the surface to the greatest depths. The **benthic environment** encompasses the life near the seafloor. Another environmental division is the separation of coastal zone from open ocean regions. The coastal zone up to the continental shelf break (at about 200 m) is defined as the **neritic environment**. The open ocean or offshore waters are terms as the **oceanic environment**.

Pelagic environment supports two basic types of marine organisms which are called **plankton** and **nekton**. Plankton are usually small organisms unable to swim against currents and are transported passively by currents in the water. Planktonic organisms are termed as **phytoplankton** or **zooplankton** depending upon whether they are plant or animal, respectively. The remaining inhabitants of the pelagic environment form the nekton. They are free-swimming animals and can act independent of water movemeents. This category includes fish, squid and marine mammals.

The environment consists of both nonliving **abiotic** (physical and chemical) components like temperature and nutrient concentrations, and **biotic** components that include the other organisms and species with which an organism interacts. The **ecosystem** is the highest level of ecological integration encompassing one or more communities in a large geographic area in addition to the surrounding abiotic environment. Examples of ecosystem include estuaries, total pelagic water column (with different communities at different depths).

1.2 Phytoplankton

The great majority of plants in the ocean are various types of unicelluar algae which are called phytoplankton. They have usually microscopic sizes, although some phytoplankton are large enough to be collected in fine-mesh nets. They live in lighted portion of the water column and constitute an essential role in the marine food chain is of paramount importance.

Diatoms are the most dominant phytoplankton group in temperate and high latitudes. They have cell size ranging from about 2 μm to over 1 mm. The second most abundant phytoplankton group are called **dinoflagellates**. Only about half of them are able to carry out photosynthesis, which is the consumption of solar energy to reduce carbon dioxide. The rest are produced by feeding on phytoplankton

and small zooplankton. This group forms essentially a part of the zooplankton. bf Coccolithophorids are the next common phytoplankton group living predominantly in warmer seas and can grown in reduced light intensities. *Emiliania huxlei* is the most widespread coccolithophorid species present in all oceans except in polar seas. Sometimes they form enormous blooms covering an area of 1000 km by 500 km.

Phytoplankton **blooms** develop when a species increases in numbers under favorable conditions. Dinoflagellates are capable of rapid reproduction, and when they may become so abundant the water has their red-brown color, producing so-called **red tides**. The bloom continues until all the nutrients are consumed by dinoflagellates, after which the bloom decays, but a large amount of organic material is produced. The bacterial decomposition of large amounts of organic material depletes the available oxygen and consequently massive fish deaths may take place.

1.3 Zooplankton

The animals making up the zooplankton range in size from microscopic, unicellular organisms to jellyfish several meters in diameter. they are capable of movement, by definition they can not make their way against a current. Also, they require organic materials (carbon and other essential chemicals) as sources of chemical energy in order to grow. They differ in how they obtain the food necessary for their growth. **Herbivores** consume phytoplankton. **Carnivores** are capable of eating other zooplankton. Some species are predominantly **detrivores** which consume dead organic material. Many of the zooplankton, however, are **omnivores** with mixed diets of plants and animal material.

1.4 Photosynthesis and Primary Production

Phytoplankton are the dominant primary producers of the pelagic community. They convert inorganic nutrients into new organic material (lipids, proteins) by the process of **photosynthesis** (using light energy) and thus initiates the marine food chain. The amount of plant produced by the primary produces is referred to as **primary production**, and the primary production per unit time per unit area (or volume) is called **primary productivity**. In photosynthesis, dissolved CO_2 is utilized by algae to produce high-energy organic substances (plant carbohydrates, $C_6H_{12}O_6$) as well as free oxygen (which is derived from the water molecule, not from CO_2). The reaction for this process is given by

$$6CO_2 + 6H_2O \xrightarrow{light} (C_6H_{12}O_6) + 6O_2 \qquad (1)$$

The energy required for the photosynthesis is derived through the absorption of light

by photo-synthetic pigments contained in algae. They absorb the light mainly in the visible region from 400 to 720 nm, but each showing different absorption spectrum. For example, for chlorophyll-a, which is the most common pigment in phytoplankton, the maximum absorption takes place in the red (650-700 nm) and blue-violet (450 nm) range (see Fig. 3.1). The colors of phytoplankton (green, brown, golden, red) are characterized by dominant pigments present in the cells.

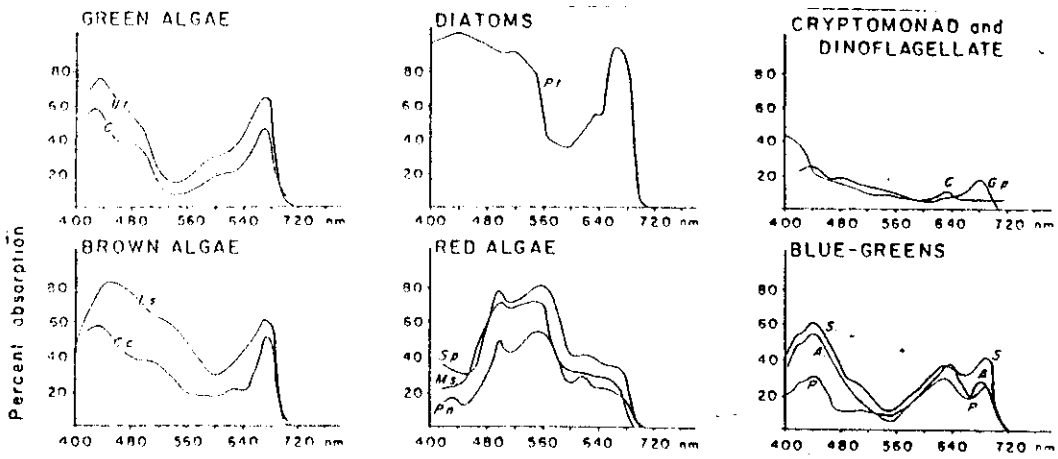

Figure 1.1 The absorption spectra of several marine photosynthetic organisms

Photosynthetic products are partly consumed by **respiration**. It is the reverse photosynthesis reaction of O_2 consumption and CO_2 production. The respiration is typically around 10% of the gross photosynthesis, even though some algal species can have high respiration rates upto 50% of P_{max}. Photosynthesis is usually expressed as mg C (mg Chl)$^{-1}$ hr^{-1}.

1.5 Latitudional and Seasonal Differences in Marine Productivity

There are latitudional and seasonal differences in marine productivity that result from differences in light and nutrient availability. There are also regional differences in how primary production is utilized by zooplankton.

When primary production increases, it is generally accompanied by a measurable increase in the standing stock of phytoplankton over a period of several days. In some areas, however, the zooplankton may graze immediately phytoplankton as fast as they are produced. Thus, the increase in primary productivity does not show any discernible increase in the phytoplankton stock. This situation is observed in **North Pacific Ocean** at about 50°N (Fig. 1.2c), where there is virtually no change in phytoplankton biomass throughout the year (typicall about 0.5 mg Chl-a m^{-3}). The primary production, on the other hand, increases from winter values of less than 50

mg C m^{-2} day^{-1} to more than 250 mg C m^{-2} day^{-1} in July. The excess primary productivity is grazed by zooplankton which increase their biomass in summer right after the peak primary production.

In contrast, in the **North Atlantic** at the same latitude, the spring bloom is characterized by a ten-fold increase in biomass from 0.1 to 1.0 mg Chl-a m^{-3} (Fig. 1.2b). Primary productivity increases as in the Pacific Ocean, but the zooplankton are less efficient for consuming phytoplankton. In much of the North Atlantic, there is also an autumn bloom of phytoplankton and subsequent increase in zooplankton biomass.

Two other annual cycles of phyto- and zooplankton are shown in Fig. 1.2. One shows the pattern in the Artic Ocean (Fig. 1.2a) where a single pulse of phytoplankton occurs soon after the disappearance of the ice and is followed somewhat slowly by a single pulse in the biomass of zooplankton. This time lag is due to relatively slow growth rates in cold water. On the other hand, in tropical waters, the biomass of phytoplankton and zooplankton do not show any substantial changes throughout the year (Fig. 1.2d). However, the storm activities can disturb this type of stable environment and small pulses in plankton biomass may occur irregularly throughout the year. In warm tropical water, any increase in phytoplankton standing stock is quickly tracked by the fast growing zooplankton.

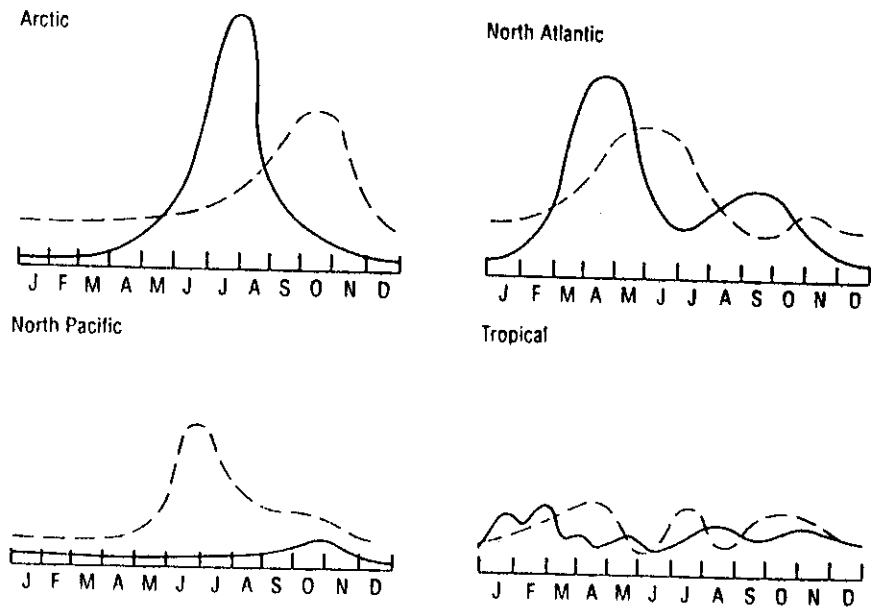

Figure 1.2 A sketch for various type of annual cycles of plankton communities in different regions. The solid lines represent changes in phytoplankton biomass; the dashed lines indicate changes in zooplankton biomass.

1.6 Pelagic Food Chains and Food Webs

Food chains are linear arrangements showing the transfer of energy and organic material through various **trophic levels** of marine organisms. Each trophic level is composed of organisms that obtained their energy in a similar manner. The first trophic level of the pelagic food chain is formed by phytoplankton, which are **primary producers** building organic materials from inorganic elements. Herbivorous species of zooplankton (protozoa, copepods, etc.) which feed directly on phytoplankton make up the second trophic level, and they are referred to as **primary consumers**. Subsequent trophic levels are formed by the carnivorous species of zooplankton that feed on herbivores (**secondary consumers**), and by the larger carnivores that feed on smaller carnivores (**tertiary consumers** including jellyfish and fish). The highest trophic level include sharks, squid, mammals which have no predators other than humans. The total amount of animal biomass produced in all higher trophic levels per unit are and per unit time is called **secondary production**. **Trophodynamic** studies examine the factors that affect transfers of energy and materials between trophic levels, and that ultimately control secondary production.

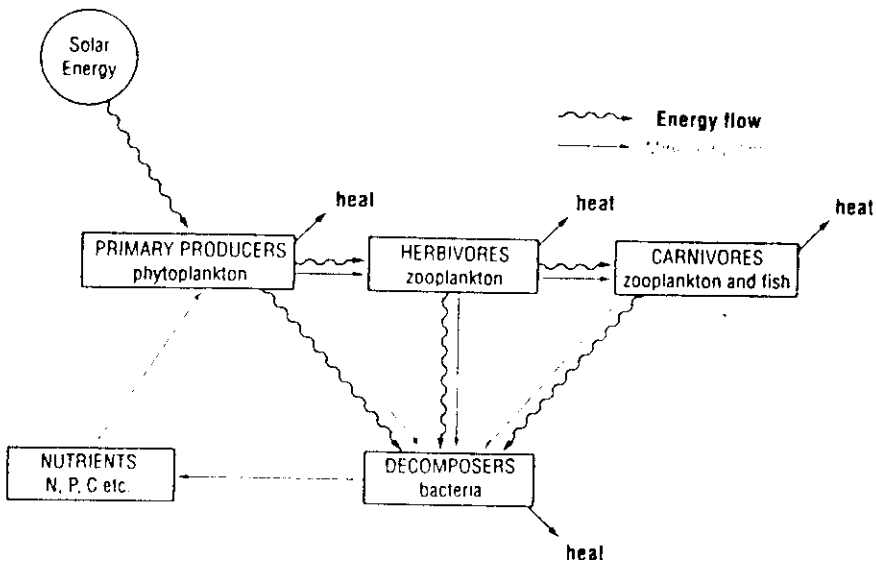

Figure 1.3. A schematic representation of mineral cycling and energy flow in marine ecosystems

Once the inorganic elements such as nitrogen, carbon and phosphorus are incorporated in plants and animal tissues, they undergo a cyclical flow through food chains

(Fig. 1.3). Bacteria decompose waste materials and dead organisms. Decomposition releases inorganic elements which then become available again for consumption by phytoplankton. Contrary to cyclical nature of the mineral flow in food chains, energy flow is unidirectional (Fig. 1.3). Apart from its consumption for growth at each trophic level, some energy is lost at each transfer to the next trophic level (as it is converted to heat energy and dissipated in respiration). As a consequence, the total energy will diminish at each trophic level.

The concept of a food chain is an attempt to reduce a complex natural system to simple dimensions. In reality, an ecosystem possesses a much more complicated interactions and energy flows between organisms. Many species do not conviniently fit into the conventional trophic levels. Some species are omnivorous, feeding on both phytoplankton and zooplankton. Some also feed on detritus, and some species change diets (and trophic levels) as they grow. A schematic depiction of all these multiple and shifting interactions is called **food web**.

The ratio of productions between two consequtive trophic levels defines the **transfer efficiency**, E_T:

$$E_T = \frac{P_t}{P_{t-1}} \tag{2}$$

where P_t is the annual production at trophic level t, and P_{t-1} is the annual production in the preceeding trophic level $t-1$. For example, for the energy transfer between phytoplankton and herbivores, E_T will equal to amount of herbivore production divided by the primary production. At the next step, the transfer efficiency will be the annual production of secondary consumers (i.e. carnivores) divided by the annual production of herbivores. Typically, in marine ecosystems, E_T from plants to herbivores is about 20%, and $10-15\%$ for the higher levels. This means that there are about respiration (the heat losses shown in Fig. 1.3).

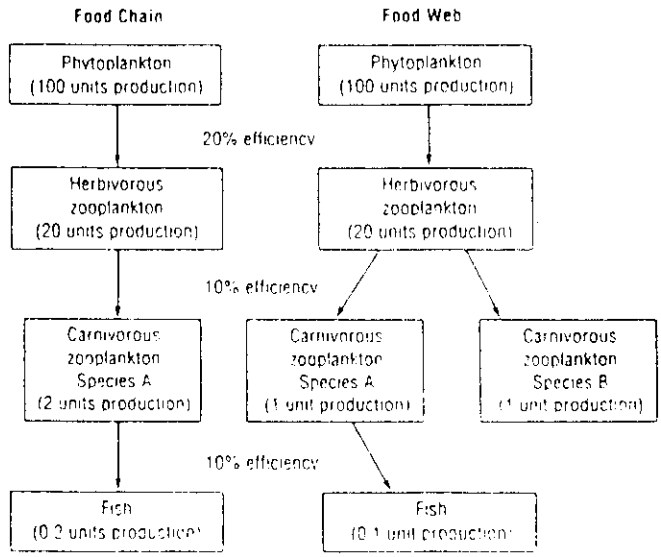

Figure 1.4. A comparision of a hypothetical marine food chain and food web

A comparision of a hypothetical marine food chain and food web is shown in Fig. 1.4. They both begin with 100 arbitrary units of phytoplankton primary production. The food chain produces 0.2 units of fish from this primary production, whereas the food web produces only one-half of this amount of fish, because two carnivore species compete for the supply of herbivores. Half of the herbivores are consumed by carnivore species A, and the other half by the species B. Fish do not eat species B, so their principal food supply becomes less by 50%.

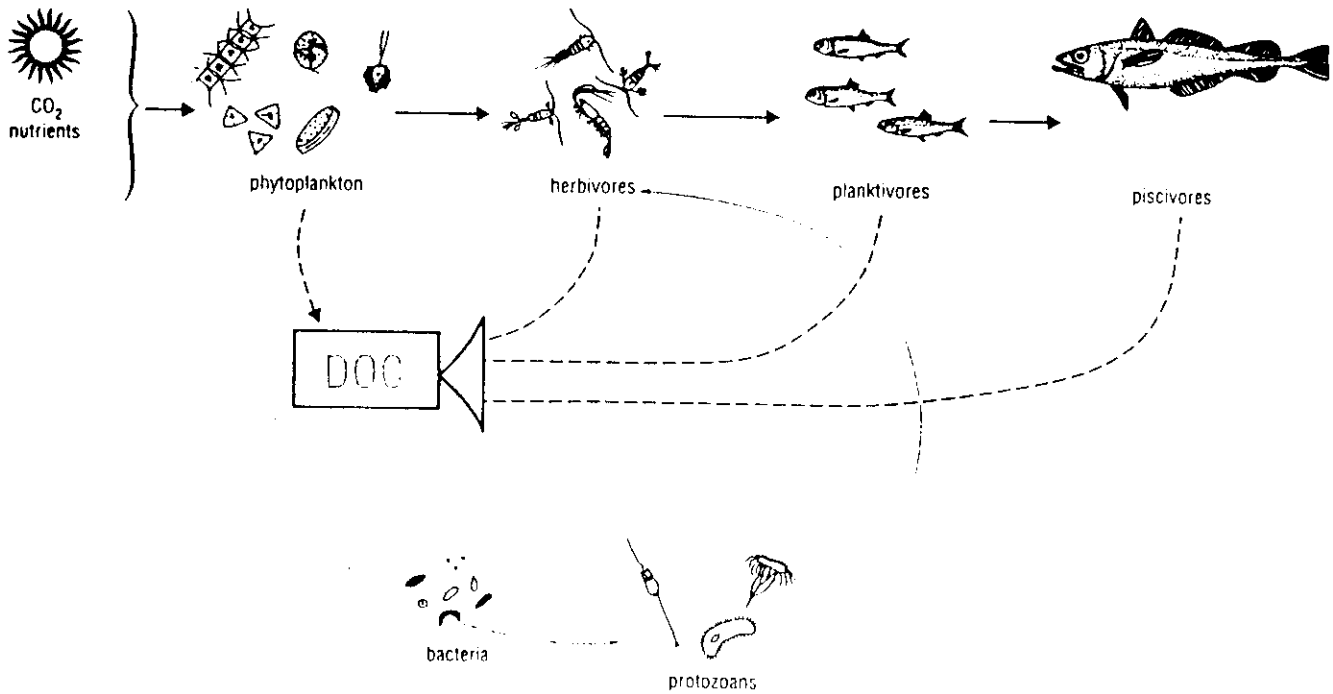

Figure 1.5. A schematic illustration of the coupling of the pelagic food chain and microbial loop. Dashed arrows indicate dissolved organic matter (DOC) release as metabolic by-products. The DOC is utilized as a source of carbon by bacteria. The bacteria are consumed by protozoans, which are in turn are eaten by larger zooplankton.

The regeneration of nutrients in the sea is a vital part of the interaction between higher and lower trophic levels. The organic materials present in the detritus pool are eventually recycled on different time scales. The process of transforming organic materials back to inorganic forms is called **mineralization**. Recycling of organic materials may take place relatively rapidly within a season in the euphotic zone, or much more slowly, over geological time scales, on the sediment. The mineralization accomplished coupling of the **microbial loop**, formed by bacteria and protozoans, with the

classic food chain of phytoplankton-zooplankton-fish (Fig. 1.5). In the oxygenated water column, decomposition of organic material takes place via aerobic decomposition through the action of heterotrophic bacteria. By this process, carbon dioxide and nutrients are returned for re-utilization by the phytoplankton. Ecologically, recycling of growth-limiting nutrients are most important. Among the nutrients, nitrate, phosphate and silicate are the limiting ones and are often found in concentrations well below the half saturation levels required for maximum phytoplankton growth. Compared with silicate and phosphorus, the recycling of nitrate is relatively more complex process.

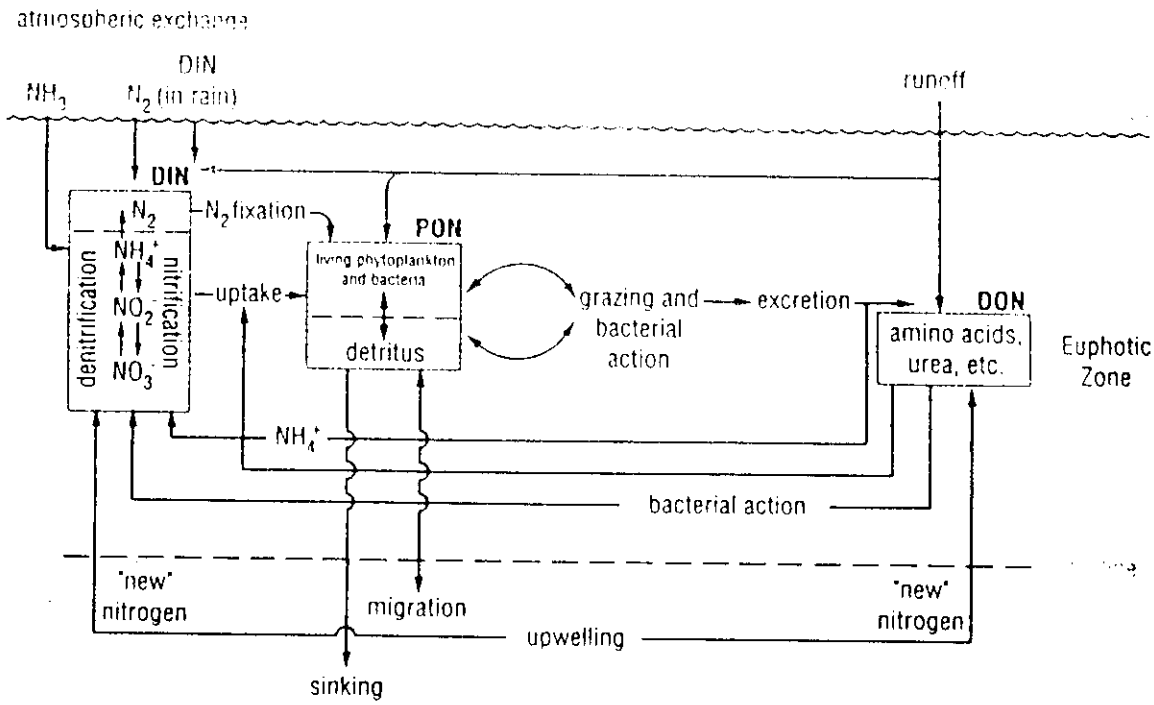

Figure 1.6. A schematic representation of a planktonic food web structure and processes.

Bacteria decompose particulate detritus formed through natural mortality of phyto- and zooplankton, or through production of faecal pellets. Bacteria can also utilize dissolved organic materials released by zooplankton excretion and phytoplankton exudation. In this way, bacteria efficiently convert dissolved organic nutrients into dissolved inorganic nutrients which eventually are converted to phytoplankton biomass. In the presence of the microbial loop, the major pathways of transfer, regeneration of organic materials and major processes related with them are shown schematically in Fig. 1.6.

The marine nitrogen cycle involves conversion between its various forms; ammonia (NH_4), nitrite (NO_2), nitrate (NO_3) and dissolved molecular nitrogen (N_2). the most dominant form that is taken up by phytoplankton is nitrate, although many species can also utilize nitrite and ammonia. Regeneration of nitrogen in the water column results from bacterial activities and excretion by zooplankton. As illustrated in Fig. 1.6, the oxidation of ammonia to nitrite and then to nitrate is referred to as **nitrification**. the bacteria that mediate this process are called **nitrifying bacteria**. The reverse process of forming reduced nitrogen compounds from nitrate is called **denitrification** which occurs in the oxygen depleted waters. These changes are carried out by**denitrifying bacteria**. The nitrogen cycle also innvolves **nitrogen fixation**, in which the nitrogen gas is converted to organic nitrogen compounds. this process is carried out mainly by cyanobacteria.

An important aspect of the marine nitrogen cycle concerns the source of nitrogen used in the primary production. Some fraction of the primary production is derived from nitrogen recycled from organic matter within the euphotic zone. This is called **regenerated production**. Another fraction is derived from **new nitrogen** which comes from subsurface waters below the euphotic zone by vertical mixing. This is called **new production**. The ratio of the new production to total (new+regenerated) production is referred to as the **f-ratio**. This number is as low as 0.1 in oligotrophic waters, but may be as high as 0.8 in upwelling zones.

The definition of the processes shown in Fig. 1.6 are given below.

Grazing: The consumption of phytoplankton by herbivores.

Excretion: The elimination of wastes produced from metabolic processes, usully in the form of urea or ammonia.

Exudation: the release of dissolved metabolites by phytoplankton.

Nitrification: The oxidation of ammonia to nitrate.

Decomposition: The breakdown of organic materials into inorganic elementsby the mediation of bacteria.

2. Factors Affecting Photosynthesis

2.1 Solar Radiation

Solar radiation is crucial for life in the sea. Light in the sea controls the maximum depth distribution of plants and of some animals. Some fraction of the solar radiation penetrating into the sea is absorbed by plants during photosynthesis, and this energy is used in the conversion of inorganic matter to organic compounds. Some wavelengths of light are absorbed by water molecules and are converted to heat, which then establishes the temperature regime of the oceans.

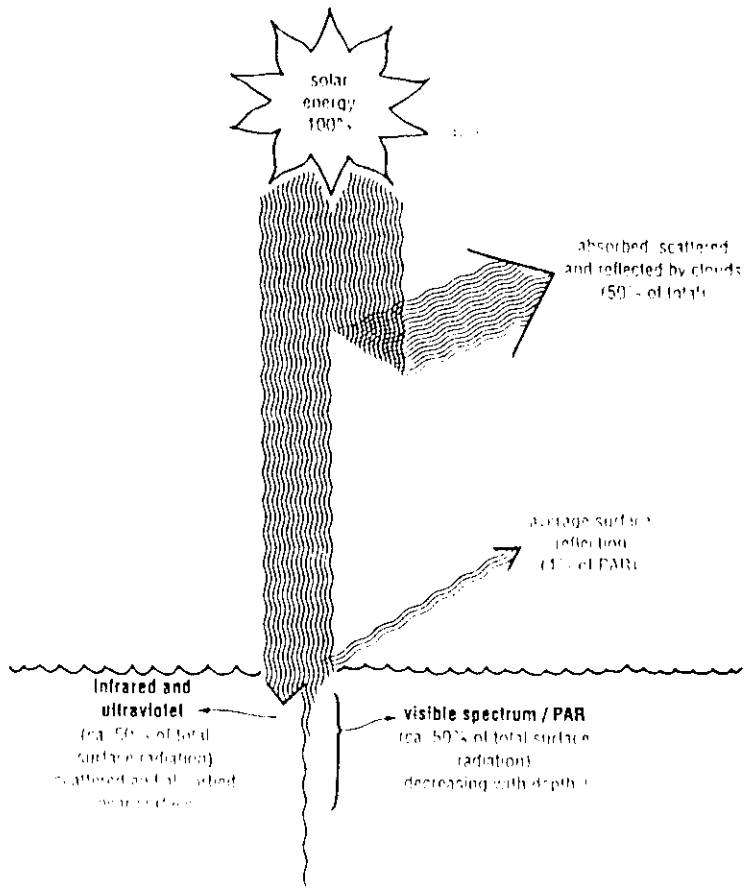

Figire 2.1 A schematic illustration of the passage of solar radiation throught the atmosphere and sea surface.

A schematic illustration of the passage of solar radiation through the atmosphere and sea surface is shown in Fig. 2.1. Solar radiation coming from the Sun to the top of the atmosphere is fairly constant at about 1360 watts/m2. About half of this energy

is absorbed and scattered within the atmosphere. The amount of radiation reaching the sea surface thus is only about 50% of total radiation. Some of this incoming radiation is reflected back into the atmosphere from the sea surface. During any day, the actual amount of radiation reaching at the sea surface at any point is a function of the sun angle, the length of the day, and the weather conditions.

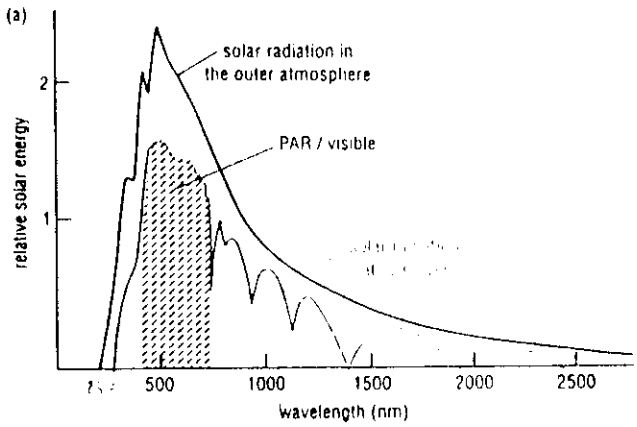

Figure 2.2 Solar radiation spectra before and after passage through the atmosphere, showing the zone of PAR or visible light.

About 50% of the solar radiation penetrating the sea surface is composed of wavelengths longer than about 780 nm. This infrared radiation is quickly absorbed and converted to heat in the upper few meters. Ultraviolet radiation (with wavelengths less than 380 nm) forms only a small fraction of the total incoming radiation, and it is also usually rapidly scattered and absorbed near the surface. The remaining 50% of the radiation comprises the visible spectrum, with wavelengths of between approximately 400 and 700 nm. This part of the radiation can penetrate deeper in the sea and is of particular importance for the biological life in the sea. These part of the radiation is often refereed to as photosynthetically active radiation (PAR). Solar radiation spectra before and after passage through the atmosphere and the zone of PAR are shown in Fig. 2.2.

As the PAR passes through water, it is both scattered and absorbed and thus it penetrates to different depths with different wavelengths (Fig. 2.3). Red light ($\sim$ 650 nm) is quickly absorbed with only about 1% still remaing at 10 m in clear water. Blue light ($\sim$450 nm) penetrates deepest, with about 1% remaing at 150 m in clear water.

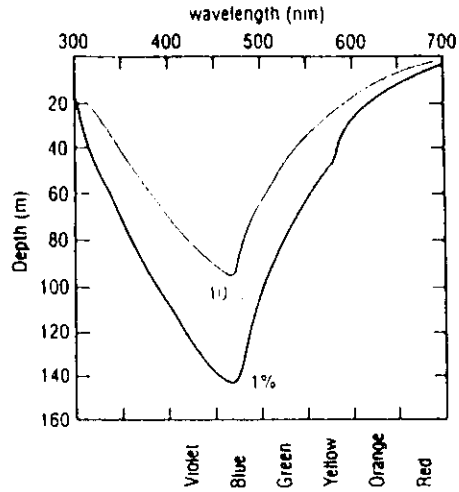

Figure 2.3 The penetration of light of different wavelengths into clear oceanic water. The lines indicate the depths of penetration for 10% and 1% of the surface light levels.

Light intensity decreases exponentially with depth, but the rate of decrease is different for each wavelength. The intensity of light at the wavelength λ at depth z can be calculated from the intensity of light at the sea surface, I_0, as:

$$I(z) = I_0 exp(-k(\lambda)\, z) \tag{1}$$

where the absorbtion coefficient $k(\lambda)$ is a function of wavelength, increasing from 0.004 m^{-1} for blue light to 0.4 m^{-1} for red light and to 20 m^{-1} in the far infrared at λ=1000 nm. Thus, the intensity of blue light at any particular depth is the larger fraction of its surface value than that of the longer wavelength light. Fig. 2.4 shows three different exponential rates of attenuation with depth, calculated using eq. 1. The absorbtion coefficient is also called the extinction coefficient.

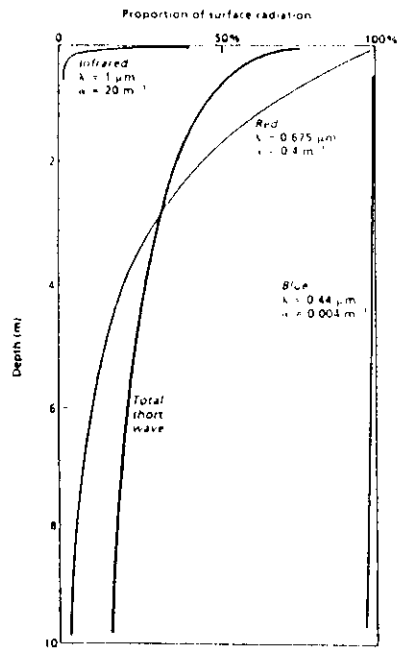

Figure 2.4 Vertical profiles of light intensity in the sea water relative to the sea surface for three wavelengths and for the total incoming short-wave radiation.

The shallowest vertical zone of the water column where the light is sufficient to support the growth and reproduction of phytoplankton is called euphotic zone. Below the euphotic zone is the dimly lighted disphotic zone, where the light is too low for photosynthesis and phytoplankton production but fish and some invertabrates can see. Living phytoplankton which have sunk from the euphotic zone may be present there. The deepest and largest part of the water column is the dark aphotic zone. This extends from below the disphotic zone to the bootom. Here, light intensity is too low to be detected by any biological system, and therefore does not support plant life.

2.2 Photosynthesis-Light Relationship

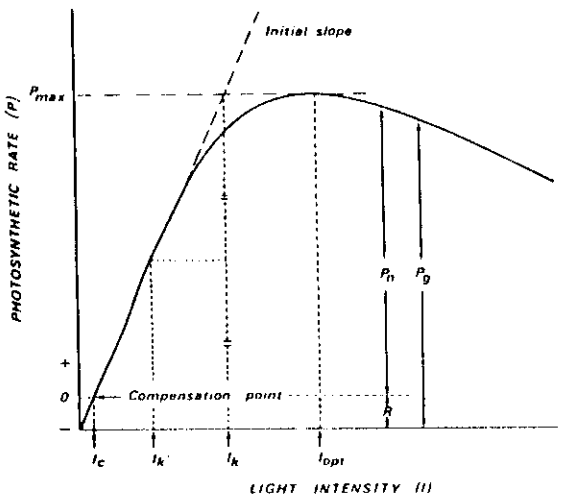

Figure 2.5 A schematic diagram of photosynthesis-light relationship. P_{max}, maximum photosynthesis; I_k, light intensity at the compensation point; R, respiration; P_n, net photosynthesis; P_g, gross photosynthesis; I_{opt}, light intensity at P_{max}; I_k, see text.

Photosynthesis rate increases with increasing light intensity. This increase is rapid and almost linear at low light intensities up to some maximal value, P_{max}, which is also called **assimilation number (or index)** (Fig. 2.5). The light intensity at the intersection of the initial slope of the P-I curve with P_{max} is designated as I_k in Fig. 2.5. At still higher light intensities, phytoplankton can not use any more light as the phytoplankton becomes light saturated. In this case, the photosymnthesis does not increase any more and continues to keep its maximal value P_{max}. At high light

intensities, on the other hand, there may be a significant decrease in photosynthesis caused by a number of physiological reactions such as shrinkage of chloroplasts in bright light. This decrease is called **photoinhibition**. Various photosynthesis-light curves from experiments on natural assemblages of marine phytoplankton are shown in Fig. 2.6.

Fig. 2.5 also shows the difference between **total photosynthesis** (or **gross photosynthesis**, P_g) and **net photosynthesis**, P_n is P_g minus respiration R. When P_g equals R, P_n is zero and the photosynthetic system is at the **compensation point**. The light intensity at the compensation point is called the **compensation light intensity**, I_c. Phytoplankton acquiring light equal or less than I_c show no growth.

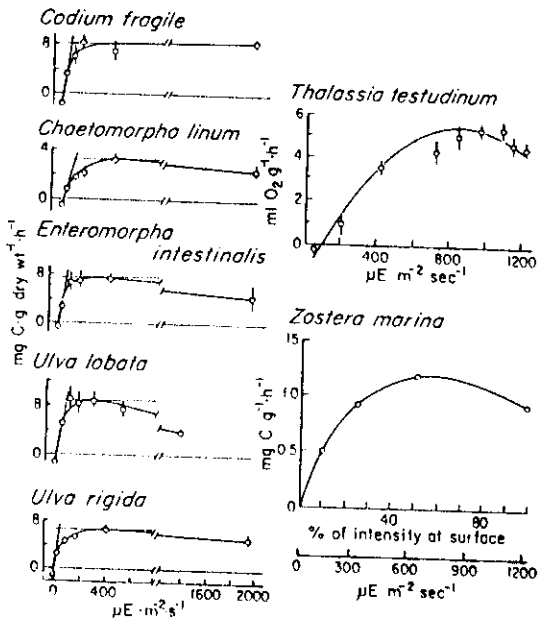

Figure 2.6 Net photosynthesis-light curves for various algae groups

The initial slope of the photosynthetic curve depends usually on cellular properties of phytoplankton. Fig. 2.7 shows P-I curves for three different phytoplankton groups; green algae, diatoms and dinoflagellates. It is shown that the maximum photosynthesis is attained at lower light intensities for green algae as compared with diatoms and dinoflagellates. Photoinhibition is apparent in all three algal groups, although it occurs at different light intensities for each group.

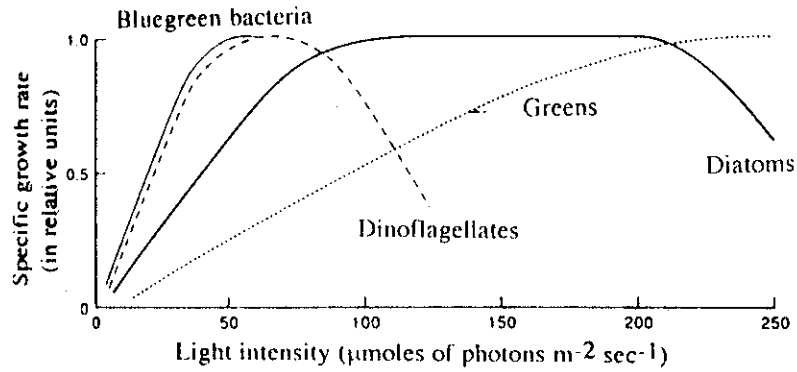

Figure 2.7 Specific growth rates versus light intensity in four major groups of marine phytoplankton

The P-I curves has beeen formulated in many ways, usually through emprical fits to curves like those shown in Fig's. 2.6 and 2.7. The simplest formulation is the hyperbolic tangent

$$P_g(I) = P_{max} tanh\left(\frac{\alpha I}{P_{max}}\right) \tag{2}$$

where I is the irradiance in W m^{-2}, α is the initial slope of the P-I curve expressed in mg C [mg Chla]$^{-1}h^{-1}$. It produces a curve like the one in Fig. 2.7c with no photoinhibition. Similar curve may also be expressed by an exponential function

$$P_g(I) = P_{max}\left[1 - exp(-\alpha I/P_{max})\right] \tag{3}$$

or, a hyperbolic function

$$P_g(I) = P_{max}\frac{I}{K_I + I} \tag{4}$$

where K_I is the half saturation value of the light intensity for which $P_g = P_{max}/2$. A slightly modified version of this function is proposed as

$$P_g(I) = P_{max}\frac{I/K_I}{\left[1 + (I/K_I)^2\right]^{1/2}} \tag{5}$$

In the case of photoinhibition, a commonly accepted expression for the P-I curve is given by an exponential function of the form

$$P_g(I) = P_{max}(I/I_{opt})\,exp(1 - I/I_{opt}) \tag{6}$$

where I_{opt} is the light intensity at which P_g equals to P_{max} (see Fig. 2.5).

The primary productivity is represented above by the assimilation index, in which growth is expressed as mg of carbon produced per mg of chlorophyll-a per hour. This value is useful for comparing photosynthesis from different regions because it normalizes all measurements to a unit of chlorophyll-a. Primary productivity is also represented as the amount of carbon per unit volume per unit time. This is actually what is measured in the sea using the C^{14} method.

Another useful way of describing phytoplankton growth rate is to express growth as an increase in cell numbers. If S_0 is the cell population at time t_0, the number of cells ΔS produced during time t is expressed by the relation

$$(S_0 + \Delta S) = S_0 e^{\mu t} \tag{7}$$

where μ is the growth constant of the population per unit of time. This expression can be used to define the **doubling time**, which is defined as the time taken for a population to increase by 100%. Thus, the time required for S_0 to double, t_d is given as

$$t_d = \frac{ln2}{\mu} = \frac{0.69}{\mu} \tag{8}$$

2.3 Nutrients

Phytoplankton production is also controlled by the concentrations of essential nutrients in seawater. For example, oligotrophic regions with poor nutrient concentrations have low productivity. On the other hand, eutrophic waters with high nutrient availability support high numbers of phytoplankton. Among the principal nutrients required for phytoplankton growth, only certain elements may be short in supply. In general, magnesium, calcium, potassium, sodium, sulphate, chloride, etc. are in all sufficient quantities for growth of phytoplankton. However, some essential inorganic substances, like nitrate, phosphate, silicate, iron may be present in concentrations that are low enough to be limiting phytoplankton production.

The observational evidence suggests that effects of nutrient concentration on the growth rate, μ, can be described by the hyperbolic function of the form (Fig. 2.8)

$$\mu = \mu_{max} \frac{N}{K_N + N} \tag{9}$$

where μ is the specific growth rate at nutrient concentration N, μ_{max} is the maximum growth rate of the phytoplankton, and K_N is a half saturation constant that is equal to the concentration of nutrients at $1/2\mu_{max}$. This expression is known as the Michaelis-Menten relation of the nutrient uptake. μ and μ_{max} are expressed in units of $time^{-1}$.

K_N attains larger values for large cells, and smaller values for smaller cells. Its typical values vary between 0.1 to 1.0 $\mu M/l$ for nitrate and between 0.1 to 0.4 $\mu M/l$ for ammonium. μ_{max} attains values of 0.1-0.2 day^{-1} for oligotrophic waters, and 0.4-1.0 day^{-1} for temperate, eutrophic waters.

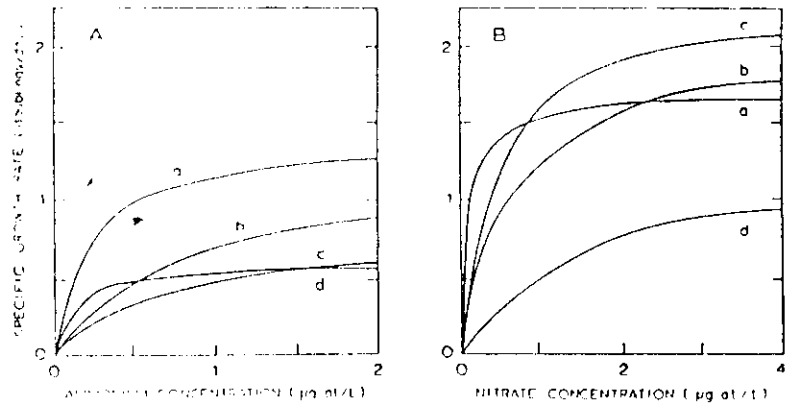

Figure 2.8 Specific growth rate versus nitrogen concentrations at two light intensities; (B) approximately 4 times (A). Curves denoted by (a) are for Coccolithus huxleyi. (b) Ditylum brightwellii, (c) Skeletonema costatum, (d) Dunaliella tertiolecta.

Differences in K_N values coupled with differences in the ability of phytoplankton species to reach their maximum growth rate at different light intensities are two important factors in determining species succession in phytoplankton blooms. An example of this is shown in Fig. 2.8a,b for four different phytoplankton species at lower and higher light intensities. In Fig. 2.8a it may be seen that *Coccolithus huxleyi* doubles its growth as compared with the others at a concentration of 0.5 $\mu M/l$. However, in Fig. 2.8b, at a higher light intensity, both *Skeletonema costatum* and *Ditylum brightwellii* grow faster than *Coccolithus huxleyi* at concentrations above 2 $\mu M/l$.

The roles of species-specific K_N and μ_{max} on the growth rates is further illustrated in Fig. 2.9 for two hypothetical phytoplankton species (S_1 and S_2) with half saturation constants $K_N(S_1)$, $K_N(S_2)$ and maximum growth rates $\mu_{max}(S_1)$, $\mu_{max}(S_2)$. Fig. 2.9a shows the case with species 1 having a higher growth rate than species 2, but both having the same value of K_N. Because K_N is the same for both species, they grow at the same rate to a certain level of nutrient, beyond which species 1 continues to its higher maximum growth rate. In the second example (Fig. 2.9b), two different species have the same value for μ_{max}, but species 1 has a lower value for K_N. In this case, species 1 reaches the maximum growth rate at a lower nutrient concentration.

In the last example (Fig. 2.9c), both species have different K_N and μ_{max} values with $K_N(S_1) < K_N(S_2)$ and $\mu_{max}(S_1) > \mu_{max}(S_2)$. In this case, competitive advantage shifts between the species as the nutrient concentration changes. At lower nutrient concentrations, species 2 dominates because it grows faster. But at higher nutrient concentrations, species 1 becomes dominant because it achieves a higher maximum growth rate.

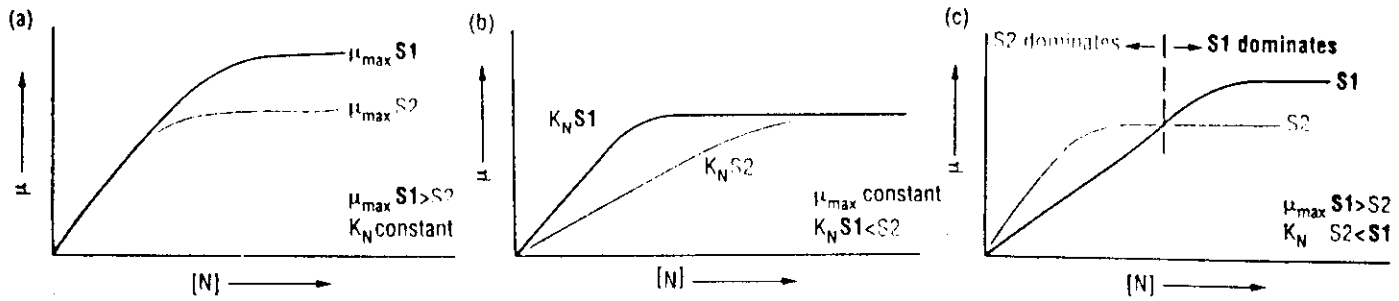

Figure 2.9 Three possible cases of nutrient versus growth curves for two different phytoplankton species with different half saturation constants and maximum growth rates.

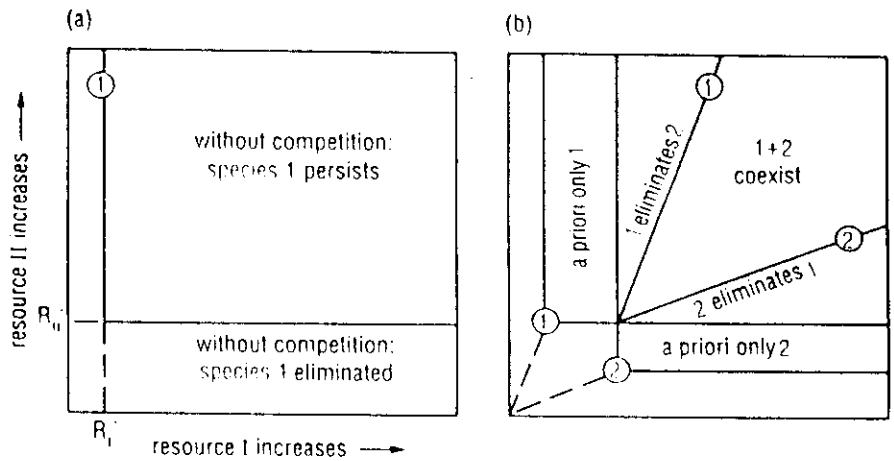

Figure 2.10 Coexistence of phytoplankton species when limited by two nutrient resources.

If there are more than one growth-limiting nutrients in the water body, and there are also differences in light and other physical properties (e.g. temperature), then

phytoplankton growth will be limited by a combination of different factors. Fig. 2.10a shows a hypothetical example for conditions with a single phytoplankton species and two potentially limiting nutrients (e.g. nitrate and phosphate). Let's consider that this phytoplankton species require a certain minimum concentrations of each nutrients (which are denoted in Fig. 2.10a by R_1^* and R_2^*). If concentrations R_1 and R_2 drop below these levels, the species cannot exist even without competition with other species. Above these minimal nutrient levels, it can survive and grow. If a second phytoplankton species with different nutrient requirements is introduced to this system (Fig. 2.10b) the situation becomes more complex. Each species can be limited by a different nutrient. If species 1 is a superior competitor for nutrient R_1, and the species 2 for the superior competitor for R_2, then only species 1 is capable to exist at low R_1 concentrations, and species 2 is the only survivor at low concentrations of R_2. At higher concentrations above the minimal R_1 and R_2, both species can coexist. But species 1 will dominate the species 2 at slightly higher concentrations of R_1, whereas the species 2 dominates the species 1 at slightly higher concentrations of R_2.

2.4 Temperature

Water temperature is the most important physical properties of the marine environment influencing the biological events, distribution of marine species, and controlling the rates at which biological processes take place. There is a continuous exchange of heat betweem the ocean and atmosphere. The seas are heated primarily by the infrared wavelengths of solar radiation. 98% of the infrared spectrum is absorbed and provides heat within about the first one meter of the water column.

Turbulent mixing produced by winds and waves transfers heat downward from the surface. This mixing creates a surface mixed layer with vertically uniform temperature. The mixed layer thickness may vary from a few meters to several hundred meters. The mixed layer deepest during winter season of intense vertical mixing, and becomes much shallower during summer which is characterized by weak mixing and more intensified solar radiation. Consequently, a thermal stratification is set up in the near-surface waters, and a seasonal thermocline separates the shallow surface mixed layer from the subsurface waters. This phenomenon persists until autumn, when the surface water is cooled again, and increased turbulent mixing destroys the seasonal thermocline and mixes the upper layer waters towards much deeper levels.

Below the mixed layer, the temperature decrease rapidly with a steep temperature gradient. This zone is known as the permanent thermocline and occurs usually between 200 and 1000 meters at temperate latitudes. The temperature difference across this layer may be as large as 20 C. Below the permanent thermocline, temperature de-

creases more gradually. A generalized temperature profile showing all these features of the vertical temperature structure is shown in Fig. 2.11.

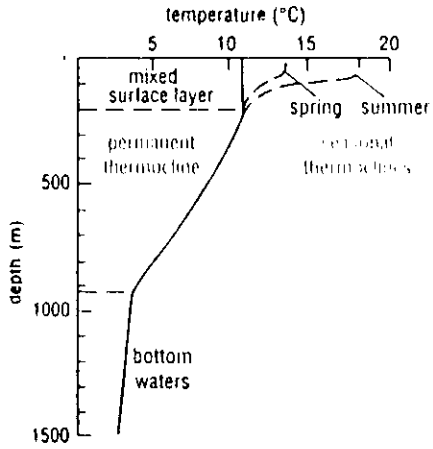

Figure 2.11 A generalized temperature profile for temperate latitudes. The solid line shows the winter condition with a mixed surface layer of homogeneous temperature overlying the permanent thermocline. The dashed lines show the formation of seasonal thermoclines that develop in the surface water in spring and summer due to elevated solar radiation and warming, coinciding with weaker winds.

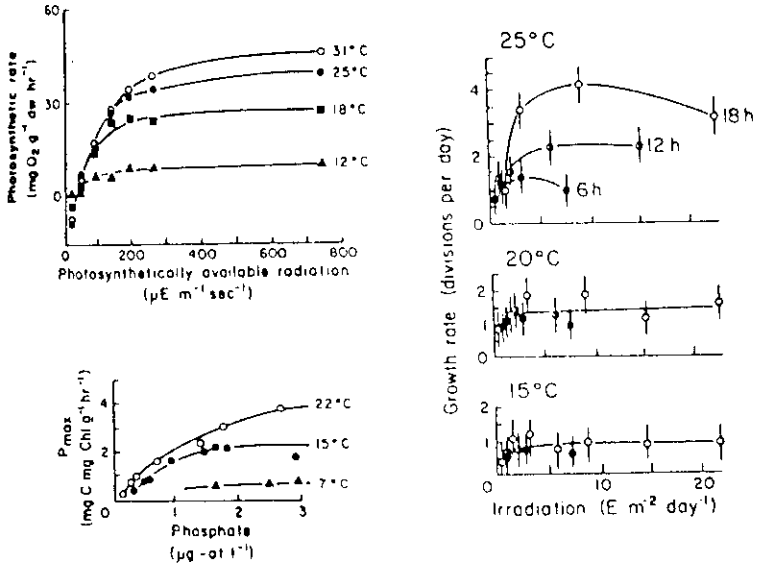

Figure 2.12 Interaction of temperature with light and nutrients. (a) Photosynthetic rate of Cladophora albida under different light intensities and temperatures in estuarine waters, (b) growth rates of Talassiosira fluviatilis at three temperatures and daylengths, (c) maximum photosynthetic rate of natural phytoplankton in Tokyo Bay under varying phosphate concentrations and temperatures.

Observations show effect of temperature on the primary production rates in the sea. This effect is not particularly pronounced as an independent factor, but become more important when combined with other factors, such as light and nutrients. For example, as the growth rates of algae are changed by the light intensity, increase in the water temperature cause somewhat higher growth rate at any level of light intensity (Fig. 2.12a). In certain species, the day length may change significantly the growth rates, but this occurs only at high temperatures (Fig. 2.12b). Higher temperatures also facilitate higher nutrient uptake rates so that the maximum photosynthetic rate increases with warmer temperatures (Fig. 2.12c).

3. The Mechanism of the Spring Phytoplankton Production

3.1 Sverdrup Model

Primary productivity varies with depth, and the the vertical distribution of phytoplankton biomass may change seasonally. This is illustrated over a time sequence in Fig. 3.1 for temperate latitudes. During the winter months, phytoplankton will be well mixed in the surface layer because of the strong vertical mixing in the water column, and any photosynthesis will follow a light attenuation curve except some photoinhibition near the surface (Fig. 3.1a). As the spring progresses, primary productivity will increase near the surface, and this will generally be accompanied with an increase in the standing stock of phytoplankton (Fig. 3.1b,c). In the late summer, as the system runs of nutrients near the surface, maximum primary productivity will shift deeper in the water column where there some nutrient are available for photosynthesis, resulting in a subsurface maximum in phytoplankton biomass.

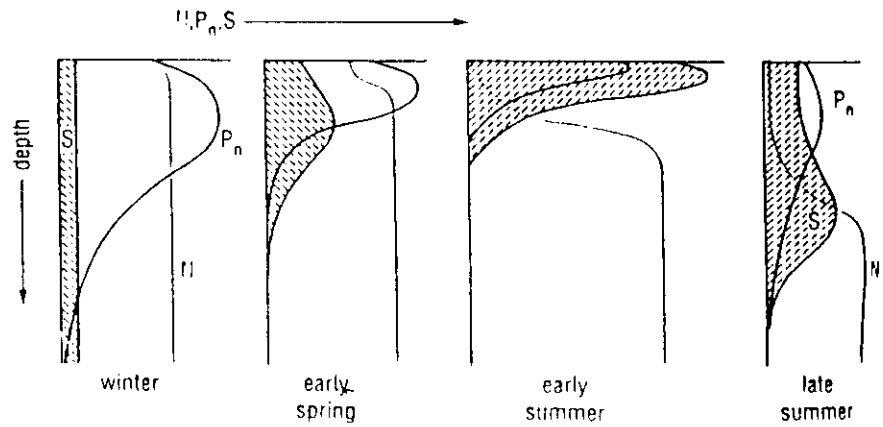

Figure 3.1 Schematic seasonal depth changes in phytoplankton biomass (S), daily net photosynthetic rate (P_n), and nutrient concentration (N) in stratified temperate water. S (shaded area) usually expressed in mg Chl-a m^{-3}. P_n usually expressed in mg C per mg Chl-a per day, N usually expressed as μM nitrate.

The role of vertical mixing in winter months and subsequent stabilization of water column by thermal stratification in early spring on the phytoplankton production was recognized for a long time. A quantitative exposition of this mechanism was presented by Sverdrup (1953). He considered the situation of the water column as shown in Fig. 3.2. The mixed layer extends to depth D_m where (i) the turbulence is sufficiently strong to distribute the phytoplankton cells uniformly, (ii) nutrients are not limiting and (iii) the light extinction coefficient is a constant. Since photosyn-

thesis is proportional to light intensity and assuming that the light intensity at the surface is not high enough to inhibit photosynthesis, the expected vertical distribution of the daily rate of phytoplankton production will have a maximum value at the surface, decreasing logarithmically to a low level at depth, as the irradiance decreases exponentially with depth. On the other hand, the rate of respiration, being more or less independent of light, will be constant throughout the mixed layer. At some depth D_c, the daily rate of photosynthesis is balanced by the daily rate of respiration. This is the **compensation depth** as we defined before. Experiments have shown that for commonly occuring diatom, the light intensity at the compensation depth is $I_c \simeq 1.5 - 1.7 Wm^{-2}$.

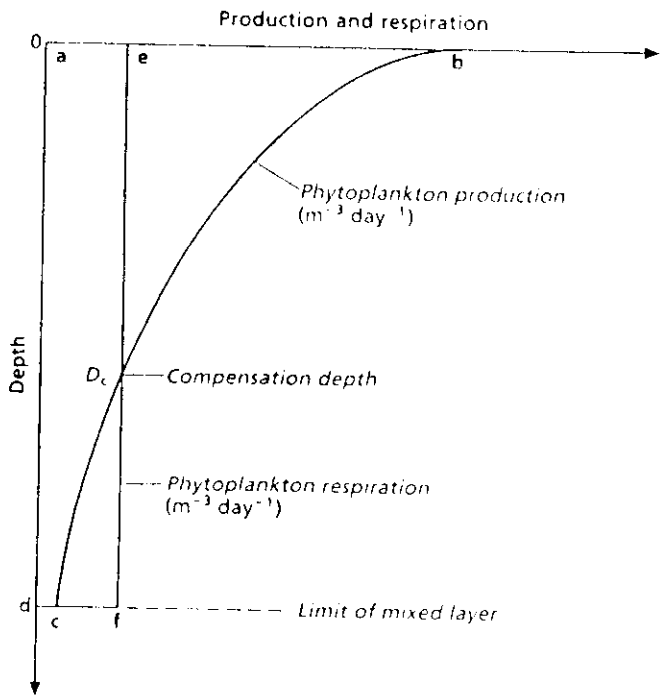

Figure 3.2 Diagram illustrating theoretical distribution of phytoplankton production and respiration.

Now consider a phytoplankton cell circulating randomly throughout the mixed layer because of the vertical mixing. When it is near the surface (i.e above the compensation depth), the photosynthetic production rate will exceed respiration. When it is near the bottom of the mixed layer (below the compensation depth) the reverse will be true. The conditions for the net positive growth is that the integrated production over the mixed layer, represented by the area *abcd*, be greater than the integrated respiration,

represented by the area $acfd$. As the depth of the mixed layer increases, respiration increases proportionately, but production increases by a small amount, or not at all. There is therefore a **critical depth** of the mixed layer at which the integrated production just equals integrated respiration. At shallower mixed layer depths, the phytoplankton population has an excess of production and therefore grows. At greater depths of the mixed layer, it fails to grow. We note that the effect of grazers has not been considered in this analysis. As the stratification develops during the spring heating season, the mixed layer may become sufficiently shallow that its thickness may be less than the critical depth. This is the Sverdrup condition for the initiation of the spring bloom.

Assuming that daily photosynthetic production at any depth is proportional to the mean daily light intensity at that depth, the integrated photosynthesis above the critical depth is given by

$$I_0 \int_{D_{cr}}^{0} exp(-kz)\,dz = I_0 \left[1 - exp(-kD_{cr})\right]/k \tag{10}$$

The integrated respiration above the critical depth is given by

$$\int_{D_{cr}}^{0} R dz = I_c D_{cr} \tag{11}$$

Equating these two expressions yields an expression for the critical depth D_{cr}:

$$D_{cr} = \frac{I_0}{kI_c}\left[1 - exp(-kD_{cr})\right] \tag{12}$$

If $kD_{cr} \gg 0$, then this expression can be simplified to:

$$D_{cr} = \frac{I_0}{kI_c} \tag{13}$$

Thus, by using this simple formula based on the amount of radiation at the surface (I_0), the extinction coefficient (k), and a known compensation light intensity (I_c), it is possible to estimate when the spring phytoplankton production can start in temperate latitudes. Sverdrup (1953) applied this concept to calculate the values of D_{cr} for ocean weather ship M in the Norwegian Sea in the spring of 1949. When plotted with data for the mixed layer depth and the numbers of phytoplankton and zooplankton (Fig. 3. 3), it became clear that the critical depth increased from about 30 m at the begining of March to nearly 300 m at the end of May. The major increase of phytoplankton and zooplankton populations occured when the depth of the mixed layer was much less then the critical depth, during May. We recall once again that Sverdrup's model applies to temperate latitudes where, after the winter deepening of the mixed layer, surface waters contain a good supply of nutrients, and where spring warming leads to a shallowing of the mixed layer.

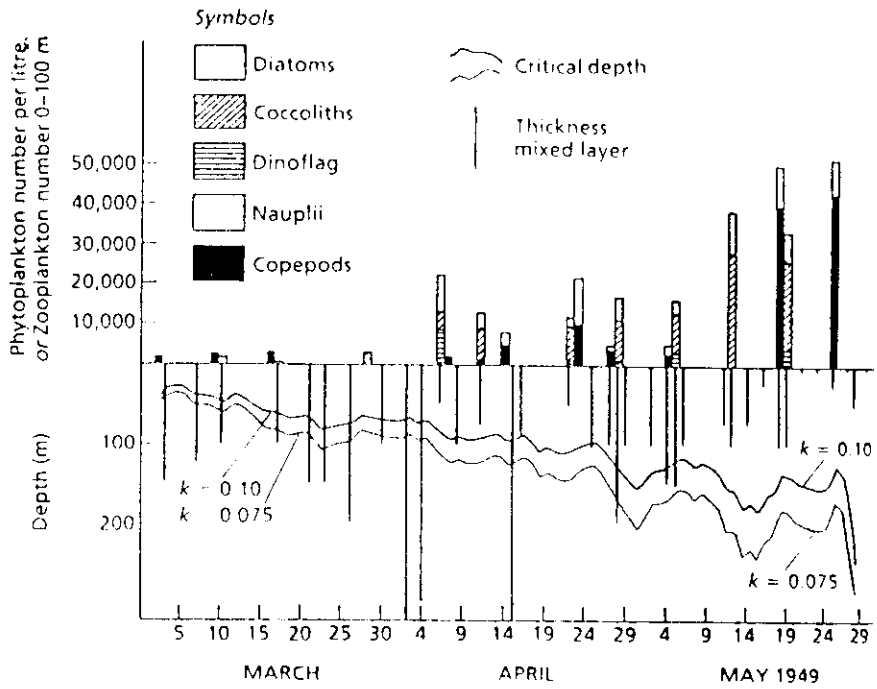

Figure 3.3 Data from ocean weather ship **M** *in the Norwegian Sea on plankton biomass, mixed layer thickness and critical depth.*

3.2 Formulation of Phytoplankton Growth

In its most general form, the photosynthesis can be expressed as

$$P(I, N, T) = P_{max} e^{r(T-T_0)} \Psi(I, N) B \tag{14}$$

where $\Psi(I, N)$ describes a function representing the light and nutrient limitations, B is phytoplankton biomass, P_{max} is the maximum growth rate (in units of time^{-1}) and the exponential term represents the temperature effect on the photosynthesis rate. It indicates that the phytoplankton growth rate P_{max} increases exponentially with the rate r above the temperature T_0 and decreases below.

$\Psi(I, N)$ can be represented in two different ways, depending on how the nutrient and light limitations are formulated. One approach is to express the light and nutrient limitation functions in a multiplicative form as

$$\Psi(I, N) = f(I) f(N) \tag{15}$$

where $f(I), f(N)$ are the light and nutrient limitation functions, respectively. $f(I)$ is given by any one of the functions described earlier by eq's (2)-(6). For any nutrient (e.g., nitrogen, silicate, phosphate), $f(N)$ is described by the Mihaelis-Menten type hyperbolic function as given previously by eq. (9). In the case of more than one nutrient limiting the phytoplankton growth (e.g. nitrate N_1 and silicate N_1), the net nutrient limitation function is taken to be the smaller of the individual nutrient resource limitation functions:

$$f(N) = min\left[f(N_1), f(N_2)\right] \tag{16}$$

The other approach is to consider the minimum of the light and nutrient limitation functions controlling the photosynthesis rate. In this case, $\Psi(I, N)$ is expressed by

$$\Psi(I, N) = min\left[f(N), f(I)\right] \tag{17}$$

It the nitrate is the limiting nutrient, the nutrient limitation function should involve contributions of both nitrate and ammonium:

$$f(N) = f(NO_3) + f(NH_4) \tag{18}$$

where

$$f(NH_4) = \frac{NH_4}{K_a + NH_4} \tag{19}$$

$$f(NO_3) = \frac{NO_3}{K_n + NO_3} e^{-\varepsilon NH_4} \tag{20}$$

where K_a, K_n are the half saturation constants, and the exponential term in the nitrate limitation function represents inhibition of nitrate uptake due to the presence of ammonium. It is generally believed that the nitrate uptake rate by phytoplankton is severely reduced by the presence of ammonium. This effect represents preference of phytoplankton ammonium uptake.

4. Fundamentals of Ecosystem Modeling

This lecture will not be an exhaustive treatment nor a how-to lesson on modeling. Its main purposes are to introduce basic concepts of the pelagic ecosystem modeling and to provide some examples.

The mechanistic modeling on the plankton ecology explores response of organisms in predictable ways to external forces, while obeying the rules of thermodynamics and conservation of mass. The models can be divided into mainly two categories as **diagnostic** and **prognostic**. Both of these approaches are examples of **compartmental** modeling, in which populations or functional groups of organisms and pools of nutrients are treated as compartments with specified inputs and outputs. If the inputs and outputs are equal, the system is said to be in the **steady-state**; if they are not, it changes in time so that a compartment either increases or decreases in size.

Diagnostic Models: are the kind of models used to diagnose the state of ecosystem based on a particular set of data. The purpose is to help us to understand the structure and functioning of the ecosystem, but not to predict their future states. Diagnostic models are useful to explore ecosystem characteristics with limited number of measurements and to find plausible values for the unmeasured quantities which obey certain rules and criteria.

Prognostic Models: simulate the temporal and spatial behaviour of plankton systems solely from the set of equations, given external forcing functions and parameters and starting from a prescribed initial state.

A prognostic ecosystem model should consist of five components:

a) Forcing functions, or external variables: These are the functions and variables which are specified externally, and influence the biotic and abiotic components of the ecosystem and the process rates. Examples for forcing functions are the daily PAR values over the year, the nitrate distribution below the euphotic zone, inflow and outflow, etc.

b) State variables: They characterize the structure of the ecosystem. For instance, if we want to model functioning of a regional pelagic food web structure, the state variables will be the most important organisms of the regional food web, and concentrations of limiting nutrients.

c) Mathematical Equations: They are used to represent the biological, chemical and physical processes, and describe the relationship between forcing functions and state variables.

d) Parameters: They are coefficients of the functions in the mathematical representation of processes, such as growth, mortality, excretion rates, etc. One of the important steps in constructing a numerical model is to specify the values of the parameters relevant for the particular ecosystem. The parameters are obtained by choosing values from the observations from the ecosystem under investigation or from those given for similar ecosystems. Further adjustment on the estimation of parameters are done by tuning of the model parameters on the basis of a series of numerical sensitivity studies.

e) Universal constants: e.g. gravitational acceleration, atomic weights, etc.

The initial focus of the research is the **definition of the problem**. This is the only way in which the limited research resources can be correctly allocated , instead of being dispersed into irrelevant activities. The term "definition" implies identification of space, time characteristics and of subsystems. It is important to determine the optimum number of subsystems and/or state variables to be included in the model. It is often argued that a more complex model should represent the real ecosystem more accurately, but this is not necessarily true. Additional factors involved. A more complex model contains more parameters, which increase the level of uncertainity since they are never completely free of errors.

Once the model complexity, at least at the first attempt, has been selected, the next step is a formulation of the processes as mathematical equations, and to carry out calibration and verification procedure. Calibration is an attempt to find the best correspondence between computed and observed data, obtained by variation of some parameters in the model. It may be caaried out by trial and error, or by some methods helping to find the best fit between observed and computed values. Verification is the test of the "internal logic" of the model. Typical questions in the verification phase are: Does the model react as expected?, Is the model stable for the long term?, Does the model obey the mass conservation? Verification is largely a subjective assessment of the behaviour of the model. The verification is basically done during the use of the model before the calibration phase.

Validation and sensitivity analysis follow verification. Through the sensitivity analysis, the modeler gets a good overview of the most sensitive components of the model. Thus, the sensitivity analysis attempts to provide a measure of sensitivity of either parameters, or forcing functions, or submodels to the state variables of grestest interest in the model. In practice, the sensitivity analysis is carried out by changing the parameters, the forcing functions and/or the submodels. The corresponding response on the selected state variables is observed. On the other hand, validation is to

compare the model outputs to known values of properties and rates at the simulated site. It is an objective test on how well the model outputs fit the data. It is required to get a picture of the reliability of the model. The validation criteria are formulated based on the objectives of the model and the quality of the available data.

Mixed Layer versus Vertically-Resolved Models

The biological models are developed along two lines. A more simplified approach is to consider the mixed layer averaged properties of the ecosytem. It assumes vertically homogeneous structures of the biological system in the mixed layer, and the interaction with the subsurface layer are done through the diffusion and entrainment processes specified at the base of the mixed layer. A more sophisticated modeling approach is to resolve the vertical variability of the ecosystem characteristics by incorporating the z-dependence in the system of biological equations. In the discretized version of the model, the z- variations are represented at a series of vertical levels, taken usually at a distance of less than 5 m. Examples for each type of models are given below.

Evans-Parslow (1985) Model of Annual Plankton Cycles

G.T. Evans and J.S. Parslow (1985) presented one of the early predictive numerical ecosystem modeling work. They investigated the features common to annual plankton cycles in different places by considering a fairly simple, two trophic level ecosystem model consisting of nitrogen nutrient N, phytoplankton P and herbivores Z in a mixed layer of varying depth over the year (Fig. 4.1). The model does not include horizontal effects implying that it is appropriate for large, horizontally uniform areas of open ocean.

This model does not also include explicitely mixed layer dynamics. Instead, the water column is divided into two completely mixed layers: an upper, biologically active mixed layer containing nutrients and plankton; and a lower, inactive layer containing only nutrients, but no plankton. The rate of change of mixed layer thickness was prescribed externally by a function $w_e(t)$ so that

$$\frac{\partial h}{\partial t} = w_e(t) = given \tag{1}$$

As the mixed layer deepens ($h(t) > 0$), water from inactive zone is mixed with the surface water, therefore entraining nutrients and phytoplankton from the deep layer, and increasing their concentrations in the mixed layer. On the other hand, as the mixed layer shallows, no new water is mixed from the lower layer, thus the nutrient

and phytoplankton concentrations do not change in the mixed layer. This condition is expressed in mathematical terms as

$$w_e^+ = max\,(w_e, 0) \tag{2}$$

Furthermore, it is assumed that herbivores can both entrain and detrain into the mixed layer. Nutrients and phytoplankton are also subject to vertical diffusion across the base of the mixed layer.

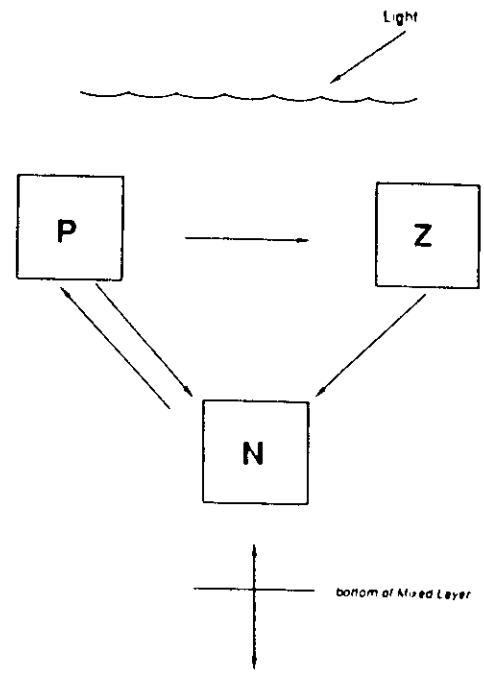

Figure 4.1 A two trophic level food chain for plankton dynamics. Arrows indicate nutrient flow pathways between phytoplankton (P), herbivorous zooplankton (Z) and dissolved inorganic limiting nutrient (N) in the mixed layer

The phytoplankton equation is given by

$$\frac{\partial P}{\partial t} = \sigma\alpha\,(I)\left[\frac{N}{K_N + N}\right]P - rP - g\left[\frac{(P - P_0)}{K_Z + (P - P_0)}\right]Z - \left(A_v + w_e^+\right)P/h \tag{3}$$

where the first term represent the phytoplankton growth according to the depth averaged light limitation $\alpha(I)$, and Michaelis-Menten uptake kinetics of dissolved nutrient, with a maximal growth rate σ and a half saturation canstant K_N. The growth is reduced by a linear death rate r, and losses due to grazing of phytoplankton by

herbiovores. The herbivore grazing is modeled by a Michaerlis-Menten hyperbola above a threshold phytoplankton concentration P_0, using the maximum ingestion rate g and the half saturation constant K_Z. The phytoplankton death is a gross parameterization of many processes including physiological death, exudation of organic substances, and losses of phytoplankton due to sinking of cells through the bottom of the mixed layer.

The herbivore equation reads

$$\frac{\partial Z}{\partial t} = \gamma g \left[\frac{(P - P_0)}{K_Z + (P - P_0)}\right] Z - mZ - w_e Z/h \tag{4}$$

which implies that the zooplankton dynamics include assimilated fraction of the food grazed by herbivores (the first term), losses of herbivores due to predation by carnivores and natural mortality with a rate m, etc.

The equation for nitrate is given by

$$\frac{\partial N}{\partial t} = -\sigma\alpha(I)\left[\frac{N}{K_N + N}\right] P - rP + \left(A_v + w_e^+\right)(N_0 - N)/h \tag{5}$$

where the first term is the loss of nutrient during the phytoplankton growth, and the second term represents the rate of nutrient concentration entrained and diffused from the lower layer. Table 1 gives the meaning and the values of the parameters used in the model.

According to this model setting, the sum of unassimilated fraction of ingested phytoplankton $(1 - \gamma)g[\frac{(P-P_0)}{K_Z+(P-P_0)}]Z$, and zooplankton mortality mZ are balanced by vertical diffusion and mixing terms.

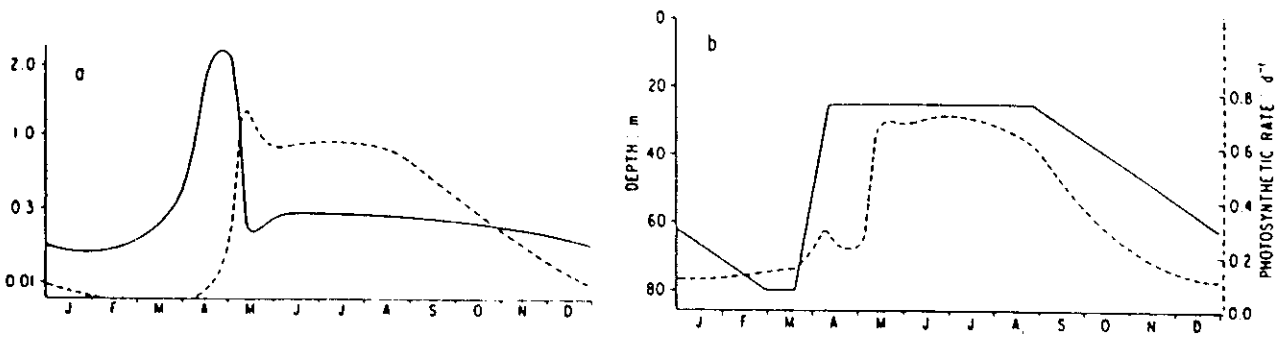

Figure 4.2 (a) The annual cycle of phytoplankton and herbivores, expressed in mmol of nitrogen per cubic meter. (b) The annual cycle of mixed layer depth in m and photosynthesis rate in day^{-1}.

The equilibrium solution of the model, using the values of parameters given in Table 1, is shown in Fig. 4.2 for a given annual cycle of the mixed layer depth. The phytoplankton distribution provides a bloom in April at the times of the shallowing of the mixed layer. As the bloom weakens in May, the herbivore biomass begins to increase. It stays uniform for the entire summer and then decreases gradually during the autumn season.

Table 1. The model parameters

Parameter	Definition	Value
k_w	Light extinction coefficient for PAR	0.1 m^{-1}
k_c	Phytoplankton self-shading coefficient	0.12 m^2 $(mmol)^{-1}$
r	Phytoplankton metabolic loss rate	0.07 day^{-1}
m	Herbivores loss rate	0.07 day^{-1}
σ	Maximum phyotplankton growth rate	2.0 day^{-1}
g	Maximum grazing rate	1.0 day^{-1}
γ	Assimilation efficiencies	0.5
K_N	Half saturation constant in nitrate uptake	0.5 mmol N m^{-3}
K_g	Half saturation constant for zooplankton grazing	1.0 mmol-N m^{-3}
A_v	Background diffusion rate	3.0 m day^{-1}
N_0	Deep nutrient concentration	10.0 mmol N m^{-3}
P_0	Phytoplankton grazing threshold	0.1 mmol N m^{-3}

Evans (1988) Model of Annual Plankton Cycles: Extention of Evans-Parslow model

Evans (1988) extended Evans-Parslow (1985) model by including a second phytoplankton group. The main motivation of the use of second phytoplankton group is to investigate seasonal successsion of different phytoplankton communities. Under the presence of two phytoplankton groups (P_1, P_2), the governing equations are written as

$$\frac{\partial P_1}{\partial t} = \sigma\alpha(I)\left[\frac{N}{K_N+N}\right]P_1 - rP_1 - g\left[\frac{(P_1-P_0)}{K_Z+(P_1-P_0)}\right]Z - \left(A_v + w_e^+\right)P_1/h \quad (6)$$

$$\frac{\partial P_2}{\partial t} = \sigma\alpha(I)\left[\frac{N}{K_N+N}\right]P_2 - rP_2 - g\left[\frac{(P_2-P_0)}{K_Z+(P_2-P_0)}\right]Z - \left(A_v + w_e^+\right)P_2/h \quad (7)$$

$$\frac{\partial Z}{\partial t} = \gamma g\left[\frac{(A-P_0)}{K_Z+(A-P_0)}\right]Z - mZ - w_e Z/h \quad (8)$$

$$\frac{\partial N}{\partial t} = -\sigma_1 \alpha(I)\left[\frac{N}{K_{1N}+N}\right] P_1 - \sigma_2 \alpha(I)\left[\frac{N}{K_{2N}+N}\right] P_2 - r(P_1+P_2) + \left(A_v + w_e^+\right)(N_0 - N)/h \tag{9}$$

where $A = a_1 P_1 + a_2 P_2$ is the total phytoplankton as percieved by herbivores with a_1, a_2 denoting food preferences of herbivores on two phytoplankton groups. The rest of the symbols and the terms are as decsribed in the previous model. In the specification of parameter values, the phytoplankton group P_1 is characterized by less growth limitation by low nutrients or low light and lower respiration rate. Therefore, this group grows more favorably in early spring period as shown in Fig. 4.3. The spring bloom occurs during the second half of April, and continues throughout the May and lasts at the begining of June. The bloom degradation period coincides with the rapid increase in the zooplankton biomass. As the zooplankton biomass decreases towards July, the second phytoplankton group P_2 starts growing during late summer. Both phytoplankton groups attain their background biomass values in winter months. The increased plankton biomass in the summer months are the major difference of this model as compared with the souktions of the previous model.

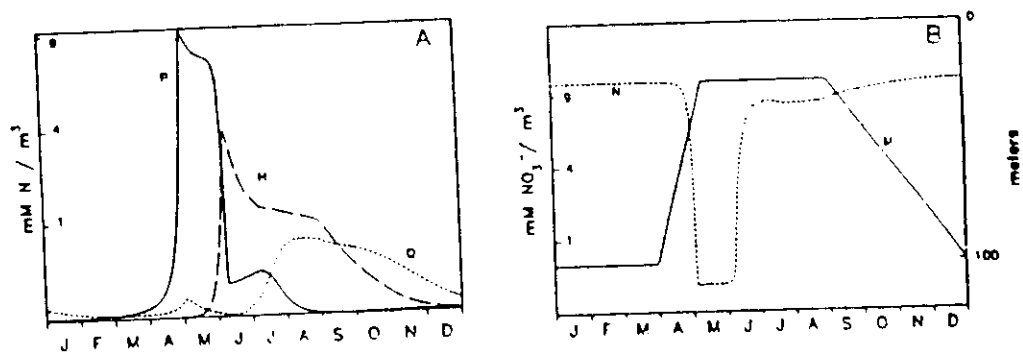

Figure 4.3 (a) The annual cycles of two phytoplankton groups and herbivorous zooplankton expressed in mmol of nitrogen per cubic meter. (b) The annual cycle of mixed layer depth in m and nutrient concentrations in mmol m^{-3}. Note that the y-axes are square-root transformed, compressing peak abundances and expanding those near zero.

Fasham et al. (1990) model

It is also a mixed layer model of plankton dynamics, essentially modified form of the Evans-Parslow (1985) model with the inclusion of more compartments. The diagrammatic representation of the model showing the compartments and the modeled nitrogen flows among compartments is shown in Fig. 4.4. The model involves single

compartments of phytoplankton and zooplankton, bacteria, detritus as well as dissolved organic nitrogen, ammonium and nitrate. The major significance of this model is to include a simple microbial loop to the main linear food chain. The food web also includes explicitely a detritus compartment formed by fecal materials and dead plankton. A part of the detritus sinks to lower layer whereras the rest is recycled within the mixed layer by reingestion by zooplankton and breakdown into dissolved organic nitrogen form and subsequent uptake by bacteria. Further details on the model is provided by Fasham et al. (1990).

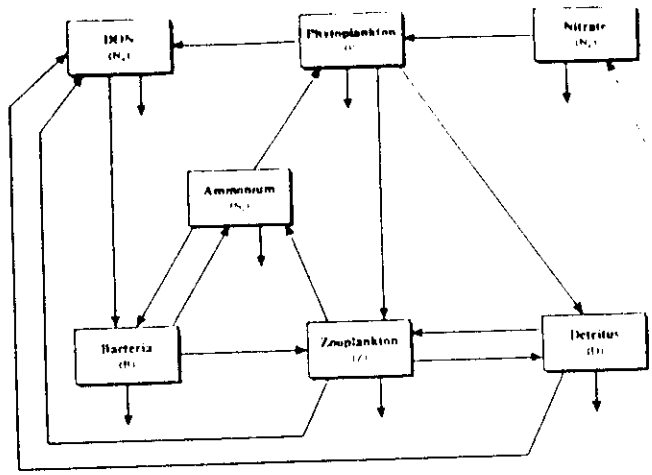

Figure 4.4 Diagrammatic representation of a nitrogen based model of mixed layer plankton and nitrogen cycling, showing the compartments and the modelled nitrogen flows among compartments, and between compartments and the deep ocean

The phytoplankton equation:

$$\frac{\partial P}{\partial t} = (1-\kappa)\,\sigma\alpha\,(I)\,\beta_t\,(N,A)\,P - rP - G_1 - \left(A_v + w_e^+\right)P/h \qquad (10)$$

where the first term represents the average daily phytoplankton growrth, the second term G_1 is the loss of phytoplankton due to herbivore grazing, r is the total loss rate due to natural mortality, respiration etc., κ is the fraction of total net primary production exuded by phytoplankton as DON. The form of grazing function is as defined earlier by the Evans-Parslow model.

The zooplankton equation:

$$\frac{\partial Z}{\partial t} = \gamma_1 G_1\,(P) + \gamma_2 G_2\,(B) + \gamma_3 G_3\,(D) - \mu_z Z - mZ - w_e Z/h \qquad (11)$$

where G_1, G_2, G_3 are the grazing rates of zooplankton on phytoplankton, bacteria and detritus respectively; $\gamma_1, \gamma_2, \gamma_3$ represent the corresponding assimilation efficiencies. μ_z denotes the zooplankton excretion rate, m is the mortality rate.

The bacteria equation:

$$\frac{\partial B}{\partial t} = U_1(DON) + U_2(A) - G_2(B) - \mu_b B - \left(A_v + w_e^+\right) B/h \tag{12}$$

This equation indicates that bacteria take up ammonium and DON, are grazed by zooplankton. These processes are represented by the first three terms on the right hand side of the bacteria equation. μ_b denotes the bacterial excretion rate which also includes contribution from the bacterial mortality.

The detritus equation:

$$\frac{\partial D}{\partial t} = (1-\gamma_1) G_1(P) + (1-\gamma_2) G_2(B) - \gamma_3 G_3(D) + rP + \Omega m Z - \varepsilon D - \left(A_v + w_e^+ + W_s\right) D/h \tag{13}$$

where the first two terms represent the fecal pellets derived from zooplankton grazing of phytoplankton and bacteria, respectively. The third term signifies the loss of detritus by zooplankton grazing. The fourth term represents the contribution of dead phytoplankton to detrital pool whereas the fifth term is the fraction of dead zooplankton included into the detrital pool. The sixth term is the breakdown of detritus to the DON form. The last term also includes the sinking of detritus with the fall speeed W_s.

The dissolved organic nitrogen equation:

$$\frac{\partial DON}{\partial t} = \kappa\sigma\alpha(I)\beta_t(N,A) P + \varepsilon D + (1-\lambda)\mu_z Z - U_1(DON) - \left(A_v + w_e^+\right) DON/h \tag{14}$$

The first four terms represent the production of DON by phytoplankton exudation, detrital breakdown, and zooplankton excretion and mortality, respectively, while U_1 is the uptake of DON by bacteria.

The ammonium equation:

$$\frac{\partial A}{\partial t} = -\sigma\alpha(I)\beta_a(A) P - U_2(A) + \mu_b B + \lambda\mu_z Z + (1-\Omega) m Z - \left(A_v + w_e^+\right) A/h \tag{15}$$

The first two terms represent the uptake of ammonium by phytoplankton and bacteria, respectively, the third and fourth are the ammonium source due to excretion of bacteria and zooplankton, the fifth is the contribution from the mortality of zooplankton.

The nitrate equation given below is described previously when we discuss the Evans-Paslow model.

$$\frac{\partial N}{\partial t} = -\sigma\alpha(I)\beta_n(N)P + \left(A_v + w_e^+\right)(N_0 - N)/h \qquad (16)$$

The external parameters are specified to predict the annual plankton production and nitrogen cycling in the Bermuda station. The model simulations are run until a steady-state annual cycle is achieved. The model is not very sensitive to initial conditions and it usually takes about 3 years to achieve a steady state. The main physical forcings in the model are the annual cycles of mixed layer depth and solar radiation. They are obtained by interpolating from monthly mean values.

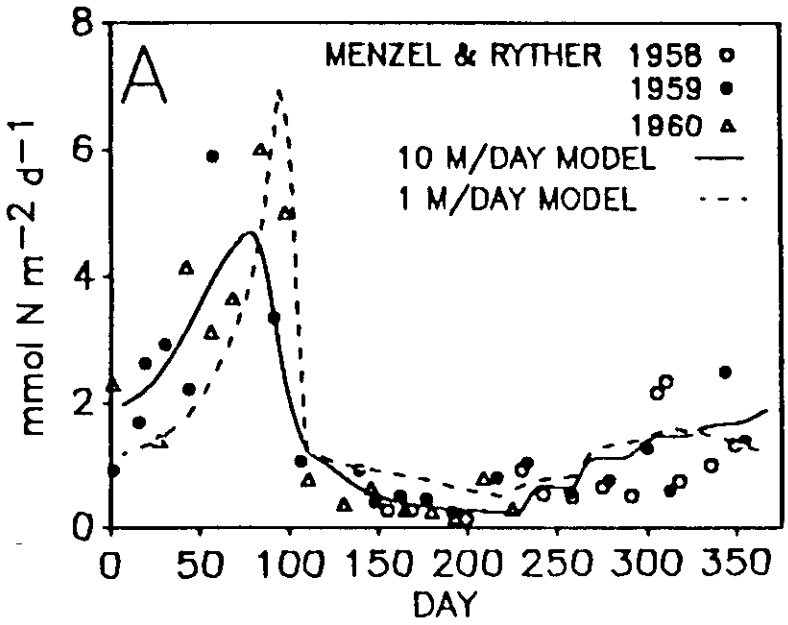

Figure 4.5 Comparision of observed and simulated mixed layer integrated primary production over the annual cycle

Fig. 4.5 shows the simulated seasonal cycle of vertically integrated mixed layer primary production (PP), for the two detrital sinking rates, compared with the data from the Bermuda station. The 10 m day^{-1} simulation appears to give a better overall fit to the observations, especially during the early part of the year and during the summer. Both simulations reproduce well the late winter/early spring increase in PP and the decline after the day 100. The annual cycles of the simulated nitrate, phytoplankton and bacteria and their comparision with the observations are given in Fig. 4.6

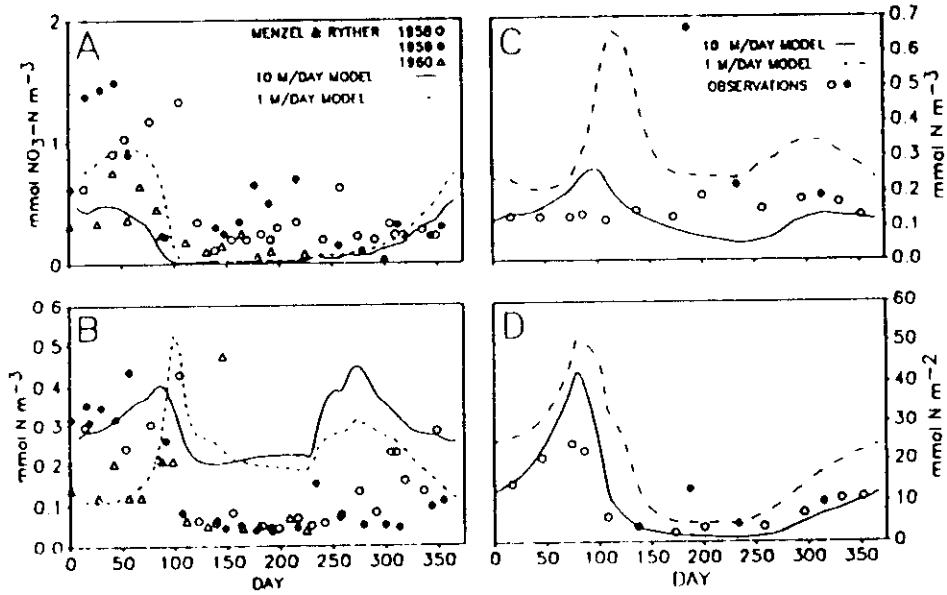

Figure 4.6 Comparision of observed and simulated nitrate concentration (a), phytoplankton biomass (b), and bacterial biomass (c) in the mixed layer. The observed and simulated mixed layer integrated bacterial biomass is shown in (d).

Size-fractionated plankton food web dynamics (Moloney and Field, 1991)

Moleney and Field (1991) introduced more sophisticated model of planktonic ecosystem by considering a more complex phytoplankton and zooplankton structures as well as carbon and nitrogen cycling. The double currency is introduced because, although nitrogen is usually the limiting nutrient in marine ecosystems, carbon also can limit growth of bacterioplankton, and there are close couplings between growth of bacterioplankton and phytoplankton.

The model plankton community structure (Fig. 4.7) consists of 3 size groups of phytoplankton (pico-; 0.2-2 μm, nano-; 2-20 μm, net-; 20-200 μm), bacterioplankton, three zooplankton groups (microflagellates; 2-20 μm, microzoo-; 20-200 μm, mesozoo-; 200-2000 μm), a detrital pool and dissolved nutrient (nitrate and carbon) pools. Autotroph carbon is obtained by carbon fixation during photosynthesis, and nitrate through its uptake from the nitrogen pool. Carbon is released as photosynthetically produced dissolved organic carbon ($PDOC$), and further C losses occur as a result of respiration, grazing, and sinking. Starting from a given set of initial conditions, the

model investigates the evolution of the plankton structure within 20 days.

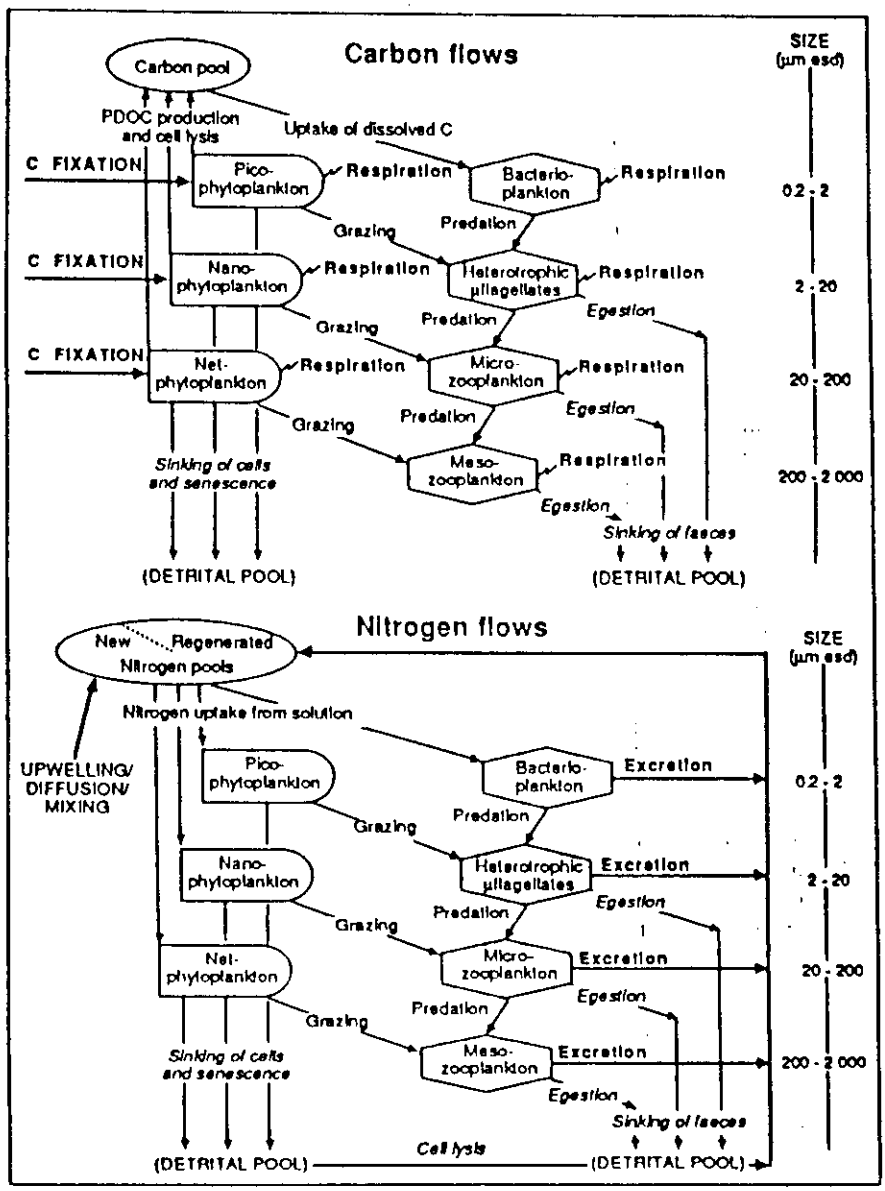

Figure 4.7 Diagrammatic representation of the model plankton community, and the flows of carbon and nitrogen.

Temporal changes in the standing stocks of are shown in Fig. 4.8. The phytoplankton community increases to a maximum of ~900 mg C m^3 after 1 day, and undergoes a

number of fluctuations before decreasing to <50 mg C m^3 by day 20 (Fig. 4.8a). Pico-phytoplankton group undergoes seven pronounced fluctuations during that period, whereas nano- and net- phytoplanktondisplay only one bloom each. These blooms are also shown in expanded scale in Fig. 4.9. The zooplankton community displays similar fluctuations to the phytoplankton community (Fig. 4.8b), with most peaks due to the nanoflagellates. The fluctuations observed in the zooplankton groups can be explained in terms of grazing pressure and nutrient limitation. For example, pico-phytoplankton growth is limited by nitrogen availability when N concentrations decrease to near-zero after 1 day (Fig. 4.8c). Pici-phytoplankton standing stocks then decrease as a result of predation by heterotrophic nanoflagellates, which also prey on the bacterioplankton (Fig. 4.8a). The fluctuations of the heterotrophic nanoflagellate standing stock (Fig. 4.8b) closely follow those of their pico-phytoplankton prey, lagging by$\sim$0.2 days (Fig. 4.9a). The nano-phytoplankton bloom is grazed down by micro-zooplankton (Fig. 4.9b), which also prey on the nanoflagellates. Net-phytoplankton standing stocks increase much slower than those of pico- and nano-phytoplankton (Fig. 4.9c). The net-phytoplankton and micro-zooplankton are grazed down by mesozooplankton (Fig. 4.9c). The mesozooplankton group has no predators, and their stock starts to decrease slowly after day 19, as a result of carbon and nitrogen losses through respiration and excretion.

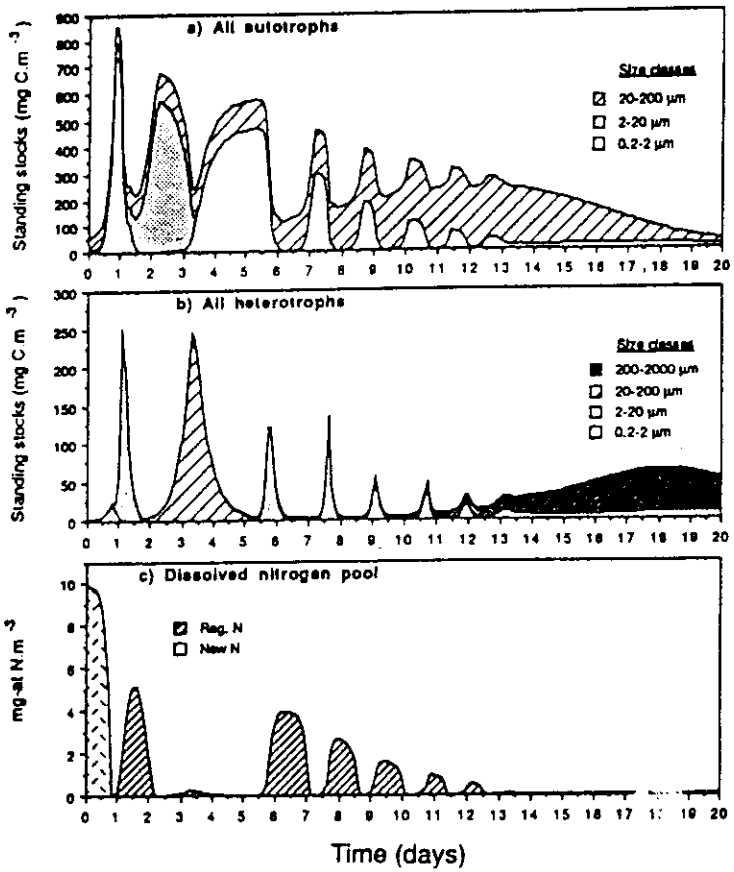

Figure 4.8 Changes with time of the standing stocks of (a) autotrophs (i.e. phytoplankton), (b) heterotrophs (zooplankton), (c) dissolved nitrogen pools.

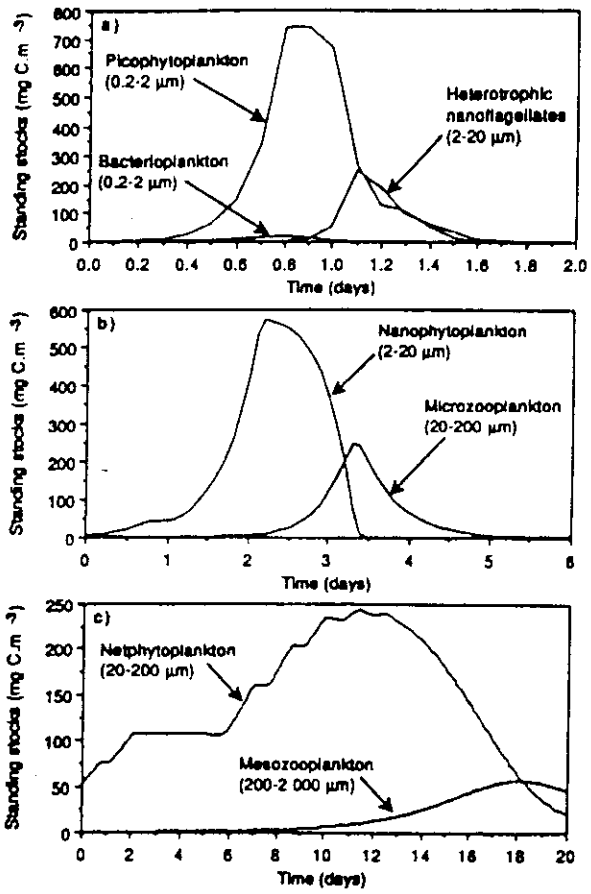

Figure 4.9 Changes with time of the standing stocks of (a) picophytoplankton, bacterioplankton and their predators (i.e heterotrophic nanoflagellates), (b) nano-phytoplankton and their microzooplankton grazers, (c) net-phytoplankton and their mesozooplankton grazers.

5. Vertically-Resolved, Coupled Physical-Biological Models

5.1 Oguz et al (1996) One-Dimensional, 5 Compartment model for the Black Sea

For a horizontally homogeneous, incompressible, Boussinesq and hydrostatic sea with no vertical water motion, the horizontal momentum equation is expressed as

$$\frac{\partial \vec{u}}{\partial t} - f\hat{k}x\vec{u} = \frac{\partial}{\partial z}\left[(K_m + \nu_m)\frac{\partial \vec{u}}{\partial z}\right] \tag{1}$$

where t is time, z is the vertical coordinate, $\vec{u}$ is the horizontal velocity of the mean flow with the components (u, v), $\hat{k}$ is the unit vector in the vertical direction, ∂ denotes the partial differentiation, and f is the Coriolis parameter. K_m denotes the viscosity coefficient for the vertical turbulent diffusion process of momentum. ν_m represents its background value associated with internal wave mixing and other small scale mixing processes. The vertical advective motion is neglected, for simplicity.

The temperature, T, and the salinity, S, are determined from transport equations of the form

$$\frac{\partial C}{\partial t} = \frac{\partial}{\partial z}\left[(K_h + \nu_h)\frac{\partial C}{\partial z}\right] \tag{2}$$

where C denotes either T or S, K_h are the coefficient for the vertical turbulent heat and salt diffusions, and ν_h is its background value. The solar irradiance which penetrates into the water column is not parameterized separately in the temperature equation, for simplicity. Its effect, together with other components of the total heat flux, is represented through the surface boundary condition given in eq. (4). One implication of this simplification is to neglect a relatively minor effect of the feedback of the biological model on the evolution of the mixed layer depth and temperature via the attenuation of radiation by phytoplankton. The density is expressed as functions of the potential temperature, salinity and pressure, $\rho = \rho(T, S, p)$, using an equation of state. The vertical mixing coefficients are determined from Mellor and Yamada (1982) level 2.5 turbulence model.

The equations (1) and (2) are subject to the following boundary conditions at the sea surface, $z = 0$:

$$\rho_0 K_m \left(\frac{\partial u}{\partial z}, \frac{\partial v}{\partial z}\right) = (\tau_{su}, \tau_{sv}), \tag{3}$$

$$K_h \frac{\partial T}{\partial z} = \frac{Q_H}{\rho_0 c_p}, \tag{4}$$

$$S = S_0 \tag{5}$$

where τ_{su}, τ_{sv} are the wind stress components, Q_H is the net surface heat flux, S_0 is the surface salinity, ρ_0 is the reference density, and c_p is the specific heat of water. The bottom of the model is taken at the 200 m depth corresponding to the base of the permanent pycnocline. No-stress and no-heat and no-salt flux conditions are specified there.

The biological variables considered are the phytoplankton biomass P, the herbivorous zooplankton biomass H, and the pelagic detritus D, the nitrate N, and ammonium A. Low

nitrate to phosphate ratio in the layer below the euphotic zone implies nitrogen as the limiting nutrient for the primary productivity in the central Black Sea due to its intense utilization in the heterotrophic denitrification process. The local changes of the biological variables are expressed by an equation of the form

$$\frac{\partial B}{\partial t} = \frac{\partial}{\partial z}\left[(K_h + \nu_h)\frac{\partial B}{\partial z}\right] + F_B \tag{6}$$

where B represents any of the five biological variables in the model, t is time, z is the vertical coordinate, ∂ denotes the partial differentiation. F_B represents the biological interaction terms expressed for the phytoplankton, herbivore, detritus, ammonium, and nitrate equations, respectively, as

$$F_P = \Phi(I, N, A)P - G(P)H - m_p P \tag{7}$$

$$F_H = \gamma G(P)H - m_h H - \mu_h H \tag{8}$$

$$F_D = (1-\gamma)G(P)H + m_p P + m_h H - \epsilon D + w_s \frac{\partial D}{\partial z} \tag{9}$$

$$F_A = -\Phi_a(I, A)P + \mu_h H + \epsilon D - \Omega A \tag{10}$$

$$F_N = -\Phi_n(I, N)P + \Omega A \tag{11}$$

where the definition of parameters and their values used in the main experiment are given in Table 1. The functions $\Phi(I, N, A)$ and $G(P)$ denote the phytoplankton growth and grazing by zooplankton, m_p is the phytoplankton mortality rate, m_h represents losses due to dead zooplankton leading to detritus production, μ is the rate of zooplankton excretion in the form of nitrogen, γ is the assimilation efficiency of zooplankton grazing on phytoplankton, ϵ is the detrital remineralization rate, Ω is the ammonium oxidation rate, w_s denotes the downward sinking velocity of detritus.

The phytoplankton production process is parameterized in terms of the Liebig's law of the minimum which assumes either light or a nutrient, but not both, controls growth rate at any instant. The total production, $\Phi(I, N, A)$, is defined by

$$\Phi(I, N, A) = \sigma_m min[\alpha(I), \beta_t(N, A)] \tag{12}$$

where min refers to the minimum of either $\alpha(I)$ or $\beta_t(N, A)$ representing, respectively, the light limitation function and the total nitrogen limitation function of the phytoplankton uptake. $\beta_t(N, A)$ is given in the form

$$\beta_t(N, A) = \beta_n(N) + \beta_a(A) \tag{13}$$

with $\beta_a(A)$ and $\beta_n(N)$ signifying contributions of the ammonium and nitrate limitations respectively. They are expressed by the Michaelis-Menten uptake formulation

$$\beta_a(A) = \frac{A}{R_a + A} \tag{14}$$

$$\beta_n(N) = \frac{N}{R_n + N} \exp(-\psi A) \tag{15}$$

where R_n and R_a are the half-saturation constants for nitrate and ammonium, respectively. The individual contributions of the nitrate and ammonium uptakes to the phytoplankton production are represented, respectively, by

$$\Phi_n(I, N) = \sigma_m min[\alpha(I), \beta_t(N, A)] \left(\frac{\beta_n}{\beta_t}\right) \tag{16}$$

$$\Phi_a(I, A) = \sigma_m min[\alpha(I), \beta_t(N, A)] \left(\frac{\beta_a}{\beta_t}\right) \tag{17}$$

The light limitation is parameterized by

$$\alpha(I) = tanh[aI(z,t)] \tag{18}$$

$$I(z,t) = I_s \exp[-(k_w + k_c P) z] \tag{19}$$

where a denotes photosynthesis efficiency parameter controlling the slope of $\alpha(I)$ versus the irradiance curve at low values of the photosynthetically active irradiance (PAR). I_s denotes the surface intensity of the PAR taken as the half of the climatological incoming solar radiation. k_w is the light attenuation coefficient due to sea water, and k_c is the phytoplankton self-shading coefficient. In the above formulation, k_w and k_c are taken to be constant with depth. The daily variation of the light irradiance, and hence the phytoplankton growth, are neglected since the biological processes we consider have time scales much longer than a day.

The zooplankton grazing ability is represented by the Michaelis-Menten formulation

$$G(P) = \sigma_g \frac{P}{R_g + P} \tag{20}$$

where σ_g is the maximum ingestion rate, R_g is the half saturation ratio for the zooplankton grazing.

No-flux conditions $[(K_h + \nu_h)\frac{\partial B}{\partial z} = 0]$ are specified both at the surface and the bottom. For the case of detritus equation, the surface boundary condition is modified to include the contribution of downward sinking flux so that $(K_h + \nu_h)\frac{\partial D}{\partial z} + w_s D = 0$. The same condition is also prescribed at the lower boundary of the model which is taken at 200 m depth, well below the euphotic zone comprising only the upper 40-50 m. The advantage of locating the bottom boundary at considerable distance away from the euphotic layer is to allow the complete regeneration of the detrital material being exported from the euphotic layer. Considering our choice of relatively low sinking rate ($w_s = 1.0 m/day$), the material exported out from the euphotic layer is remineralized until it reaches the lower boundary of the model. As seen from equations (7)-(12), the vertically integrated biological model is fully conservative. The state of the system at time t is governed by its evolution through the internal dynamical processes from the specified initial conditions.

The momentum and temperature equations are forced, respectively, by the monthly varying wind stress and surface heat flux climatologies. The monthly surface salinity values are stipulated as the boundary condition in the salinity equation. This condition implies to restore the salinity in the top grid layer with an infinite restoring time scale. As compared with the flux boundary condition, it leads to predicting a more realistic salinity structure, in a better agreement with the observations during the year. The climatological heat flux data is adjusted to make the net annual flux zero.

The model is initialized with the stably stratified upper ocean temperature and salinity profiles representative of the autumn climatological conditions for the interior part of the Black Sea. The initial nitrate profile is similar to those shown by the observations. Initial phytoplankton, zooplankton, detritus and ammonium distributions are taken vertically uniform within the euphotic layer.

A total of 51 vertical levels is used for the water column of 200m depth. The grid spacing is compressed slightly towards the surface to increase the resolution within the uppermost levels. The numerical scheme is implicit to avoid computational instabilities due to small grid spacing. The separation of solutions associated with the leapfrog time differencing is avoided by using a time filter. A time step of 1 hour is used in the numerical integration of the equations.

First, the physical model is integrated for five years. An equilibrium state with repeating yearly cycle of the dynamics is achieved after three years of integration in response to the imposed external forcings and to the internal processes in the system. Using the results of the fifth year of the physical model, the biological model is then integrated for four years to obtain repetative yearly cycles of the biological variables. The quantitative measure of testing the attainment of the cyclical state is to check whether the depth integrated total nitrogen content, N_T(=N+A+P+H+D), approaching to a constant value over the annual cycle.

Simulation of the Upper Layer Physical Structure

The seasonal temperature variations (Fig. 5.1a) reveal a convectively formed 50 m deep mixed layer during winter, followed later by a shallow summer mixed layer (less than 20 m) and very sharp seasonal thermocline. During its winter formation period, the cold water mass situated immediately below the thermocline is colder than the underlying water mass by about 1.5 °C. Following the onset of spring warming, the upper 20 m part of this cold water mass gradually warms up and is isolated from the cold water core through a sharp seasonal thermocline. Below the thermocline, the cold water core subducts gradually towards slightly deeper levels during the rest of the season. In summer months, when the surface temperature becomes as high as 24-25 °C, temperature difference of about 18 °C occurs within approximately 20 m below the shallow surface mixed layer. This very sharp seasonal thermocline plays a crucial role in the evolution of the summer phytoplankton structure.

October is a transitional period after which cooling of the surface waters gradually erodes the summer stratification. The end of December and beginning of January are times of weakest temperature stratification; the temperature of the entire upper layer water column varies around 8.5±0.5 °C. This is followed by the next cycle of cold water mass formation during January-February period. The formation and maintenance of the Cold Intermediate Water (CIW) mass are well-known features of the Black Sea thermohaline structure and discussed in many publications.

Fig 5.1b reveals great seasonal variability of the vertical mixing within the upper 50 m layer. Vertical eddy diffusivity is only a few $cm^2\ s^{-1}$ above the thermocline during the summer season, decreasing to its background value of 0.1 $cm^2\ s^{-1}$ below. This characterizes the detrainment phase of the mixed layer. Once the atmospheric cooling starts and the winds intensify in September, vertical mixing strengthens, the mixed layer entrains water from below and consequently deepens. Gradual development of this process is noted in Fig. 5.1b by a two order of magnitude increase in the value of the vertical eddy diffusivity in October. Late autumn and winter are the strongest cooling period of the year, in which the vertical diffusivity exceeds values of 1000 $cm^2\ s^{-1}$. The convective overturning process generates complete mixing, and cools the uppermost 50 m part of the water column. At the base of the mixed layer, on the other hand, the turbulence dies off quickly and vertical eddy diffusivity decreases to its background value. This level of the vertical eddy diffusivity therefore provides a quantitative measure of the mixed layer depth.

Simulation of the Euphotic Zone Biological Structure

The temporal and vertical distributions of the phytoplankton (Fig. 5.2a), zooplankton (Fig. 5.2b), detritus (Fig. 5.2c) and nitrate and ammonium (Fig. 5.2d,e) reveal several phases within the year in harmony with the surface layer physical structure. The entire summer and early autumn period is characterized by the nutrient depletion (N < 0.5 $mmol/m^3$) and the phytoplankton biomass (~0.1 $mmol/m^3$) within the mixed layer. Phytoplankton biomass is low because, with the decline of K_h from its winter values of >100 cm^2/s to <10 cm^2/s, the nutrient supply from nutrient rich waters below the mixed layer is no longer possible, and all the phytoplankton biomass is consumed by herbivores in the surface waters. The nitrate concentrations at depths immediately below the seasonal thermocline increase rapidly which, together with the sufficient light availability, allow some subsurface phytoplankton biomass production in the layer between the seasonal thermocline and the base of the euphotic zone during the May-July period. The phytoplankton patches are mostly concentrated immediately below the surface mixed layer between the depths of about 20-30 meters, but may extend up to ~50m.

As the seasonal thermocline weakens and the deepening of the mixed layer begins by the end of October, the surface layer starts to be enriched with nutrients entrained from below. The late autumn phytoplankton bloom is developed later during the second half of November. This is identified with the peak phytoplankton concentrations of about 0.35 $mmol/m^3$ within

the upper 30-35 m layer. The bloom terminates within the first half of December after which the entire winter season, until the end of February, is characterized by low concentrations (~0.10 mmol N/m^3) of phytoplankton biomass. The nutrients used up in the euphotic layer during the autumn bloom period are compensated immediately by the continuous supply from the lower levels, as a result of vertical mixing generated by the winter convective overturning mechanism.

The mid-winter phase, from the begining of January to the end of February, is identified by very low phytoplankton concentration. The mixed layer nitrogen concentration increases gradually to maximum values of about 2 mmol N/m^3 at the end of February (Fig. 5.2e) when the water column is overturned completely and a deeepest and coolest mixed layer formation is established. The spring bloom initiates within the first week of March. The bloom reaches its maximum intensity of ~1.9 mmol N/m^3 in the euphotic layer a week later. The major part of the bloom takes place within the upper 30 m of the water column, even though it extends to the depth of 50m forming approximately the base of the euphotic zone. The bloom event continues about a week-to-ten days, and then begins to degrade with phytoplankton concentrations of about 0.1-0.2 mmol N/m^3 towards the end of the month. As the nitrogen is consumed almost completely in the upper 25 m layer during the bloom, the zooplankton and detritus biomasses attain their peak concentrations simultaneously (Fig. 5.2b,c).

The detrital material is remineralized immediately and produces ammonium with typical concentrations of about 0.5 mmol N/m^3. A part of the ammonium concentration is used in the regenerated production process, the rest is converted to the nitrate form through the nitrification process. The contribution of this process is evident in Fig. 5.2e by the 20 m thick band of relatively uniform nitrate concentrations from immediately below the thermocline to the depths of about 50 meters during April to November period. In the model, the nitrification is considered as a direct conversion from the ammonium to the nitrate without having the intermediate step of the nitrite formation. In reality, however, a small fraction of the nitrate concentrations within this zone should appear in the nitrite form. The nitrate accumulation in the 30-50 m zone form eventually the main nutrient source which is later brought up to the surface during the convective overturning process and used during the next spring bloom. A typical nitrate profile in this period is thus characterized by very low values within the surface layer, increasing gradually below the thermocline up to about 50 m depth and then a rapid increase to its subsurface maximum further below.

The third phytoplankton growth process takes place during the second week of April, above two-three weeks after the complete termination of the March bloom. The ammonium, produced as a product of the March bloom and trapped within the recently formed mixed layer about the seasonal thermocline, leads to a short-period (about one week) phytoplankton production comparable with the intensity of the late-fall bloom episode (P~0.30 mmol N/m^3). This is surface intensified bloom extending only to the depths of 20m. The summer season is the period of low production. The stratification and subsequent formation of the

strong seasonal thermocline inhibit nutrient flux into the shallow mixed layer from below. Since the regenerated products have already been utilized in the mixed layer, severe nutrient limitation prohibits the development of the bloom during the summer season. However, some phytoplankton production (P~0.20 mmol N/m^3) occurs until July in deeper levels where a favourable balance of light and nutrient availability still exists.

The yearly distributions of zooplankton and detritus follow closely that of the phytoplankton with a time lag of approximately two weeks. The maximum zooplankton concentrations of about 0.2, 0.4 and 0.3 mmol N/m^3 occur following the late autumn and winter blooms as well as the period of summer subsurface phytoplankton maximum, respectively. The detrital material sinking with the fall speed of 1.0 m/day reveals a diffusive vertical distribution within the euphotic layer for most of the year. Its concentrations are almost twice the zooplankton's during the summer months following the major spring bloom event. The material is continuously remineralized and converted to the nitrogen form which becomes available for recycling into the upper levels by the late autumn.

Annual Nitrogen Budget

One way of checking internal consistency of the model dynamics is to evaluate the balance of terms governing the plankton dynamics, when integrated over the depth of the euphotic zone and over the year. This computation also provides the intercompartmental transfer rates and the fluxes across the base of the euphotic layer, which constitute a crucial part of our understanding of the biogeochemical cycle of the upper layer of the Black Sea. Though not impossible, this is extremely difficult to achieve by measurements.

Defining the total particulate organic nitrogen content PON as the sum of phytoplankton, herbivore and detritus concentrations, and the total nitrogen content NA as the sum of nitrate and ammonium concentrations;

$$PON = P + H + D, \qquad NA = N + A \tag{21}$$

equations 7-12 can be reduced to the following forms when integrated over the euphotic zone and over the year, together with using the zero-flux conditions at the sea surface.

$$\int\int \Phi(I,N,A)\,P dz dt = \int\int (\mu H + \epsilon D)\,dz dt - \int (\Gamma_{PON} + w_s D)_h dt \tag{22}$$

$$\int\int \Phi(I,N,A)\,P dz dt = \int\int (\mu H + \epsilon D)\,dz dt + \int (\Gamma_{NA})_h dt \tag{23}$$

where Γ_{PON} and Γ_{NA} are the vertical diffusive fluxes of PON and NA, respectively, and the subscript h refers to the base of the euphotic layer.

The annual budget (Fig. 5.3) given by eq.'s 22 and 23 implies an approximate balance between the external input of total nitrogen flux into the euphotic layer from below (Γ_{NA}=41.5 mmol m^{-2} yr^{-1}) and the sum of the total particulate organic matter flux (Γ_{PON}=5.7 mmol m^{-2} yr^{-1}) and the detrital sinking flux ($w_s D$=35.3 mmol m^{-2} yr^{-1}) from the base of the euphotic zone. They further indicate that the total production (ΦP=532 mmol m^{-2} yr^{-1})

is compensated by the ammonium generated within the euphotic zone through the remineralization of detritus (ϵD=304.2 mmol m^{-2} yr^{-1}) and zooplankton excretion (μH=196.7 mmol m^{-2} yr^{-1}) plus the external input of total nitrogen flux into the euphotic zone from below (Γ_{NA}=41.5 mmol m^{-2} yr^{-1}). The nitrate and ammonium uptakes are 193.5 mmol m^{-2} yr^{-1} and 338.5 mmol m^{-2} yr^{-1}, respectively, which account 36% and 64% of the annual gross primary production. However, because a large part of the nitrate uptake is derived from the ammonium oxidation, all of the nitrate uptake can not be accounted for the new generation. It is therefore more appropriate to define the *f ratio* as the ratio of nitrate flux across the base of the euphotic layer to the total primary production. The annual mean value of this ratio is 41.5/532 = 0.08. Furthermore, 58% of the primary production was assimilated by zooplankton and 20% is lost to detritus as fecal pellet egestion. The detritus remineralization of 304.2 mmol m^{-2} yr^{-1} accounts for almost all the annual ammonium production, whereas the contribution of the zooplankton excretion (196.7 mmol m^{-2} yr^{-1}) is comparable with the ammonium oxidation flux of 175.3 mmol m^{-2} yr^{-1}. Finally, we note that the yearly mean detrital sinking flux estimate of 35.3 mmol N m^{-2} yr^{-1} at the base of the euphotic layer compare well with the observed value of 11.5 mmol N m^{-2} yr^{-1} obtained from the sediment trap measurements during May 1988.

Dynamics of the Phytoplankton Blooms

The main mechanisms controlling the initiation, development and the degradation of the March and November blooms, as well as the subsurface maxima of the summer season are described briefly in this section. We first consider the relative roles of light and nutrient uptake in the primary production process. The control of the phytoplankton growth by either light or nutrient limitation during the year is highlighted in Figs. 5.4a,b. The most striking feature of the nutrient limitation function $\beta_t(N, A)$ (Fig. 5.4b) is the presence of very sharp, narrow high gradient zone. This is situated approximately at 30-40 meter depths for most of the year, except during the January and February period, and separates the low β_t region near the surface from the region of its high values (close to one) immediately below. The light limitation function $\alpha(I)$, on the other hand, has the opposite structure with decreasing values toward the deeper levels (Fig. 5.4a). The net growth function (Fig. 5.4c), computed by chosing the minimum of these two, is thus governed by the nitrogen limitation near the surface and by the light limitation at deeper levels. A subsurface maxima region is present in between, at the depths of about 30-40 m where they both have the moderate values. During the summer season, this is responsible for the subsurface phytoplankton production (c.f. Fig. 5.2a).

We note from Fig. 5.4c that highest values of the net growth function within the upper 25 m layer occur during the January and February months. But, the bloom development takes place at a later time, during the early March. The absence of bloom generation in the mid-winter period has two dynamical reasons. First, although the net growth function has the exceptionally high values, the amount of phytoplankton biomass in the water column is not sufficient to keep the primary production above a certain level sufficient to initiate the

bloom. Second, the surface layer has relatively strong downward diffusion, which counteracts against primary production and therefore prevents the bloom development. However, as soon as the intensity of the vertical mixing diminishes at the end of February (Fig. 5.5a), a new balance is established between the primary production (Fig. 5.6a) and the time change of the phytoplankton biomass (Fig. 5.6d) with almost no contributions from the grazing and the mortality terms. This new balance leads to an exponential growth of the phytoplankton concentration in the mixed layer. Soon after the initiation phase, the zooplankton grazing (Fig. 5.6c) starts dominating the system and balances the primary production. This continues until the nitrate stocks in the mixed layer are depleted and the nitrate-based primary production weakens. At the same time, rapid recycling of the particulate material allows for the ammonium-based production, also contributing to the bloom development (Fig. 5.6b). The bloom terminates abruptly towards the end of March when the ammonium stocks are also no longer available for the regenerated production.

Termination of the convective mixing process at day 65 is implied in Fig. 5.5a by sudden reduction of K_h values from the order of 1000 to the order of 10 cm^2/sec^2. Further shown in Fig. 5.5b and 5.5c that the period of high K_h values is identified with the vertically uniform temperature structure of about 6.8°C and the phytoplankton structure of approximately 0.1 mmol N/m^3. Following the termination of convective overturning, the detrainment process, which is indicated by the zone of high K_h values at 40-50 meter depths after day 65 begins establishing the subsurface stratification. As the mixed layer temperature increases by about 0.3°C (from 6.90 to 7.2°C), the bloom attains its peak amplitude within the next 10 days (Fig. 5.5c).

The similar process of bloom generation repeats during November. Again, a week balance between the nitrate-based production and the time rate of change of phytoplankton concentration initiates the exponential phytoplankton growth, which in turn strengthens the new production. The bloom terminates as soon as the nitrate stocks are depleted in the euphotic zone. The ammonium based regenerated production plays little role in the autumn bloom. It, however, contributes more to the subsurface phytoplankton development during the summer months (Fig. 5.6a,b).

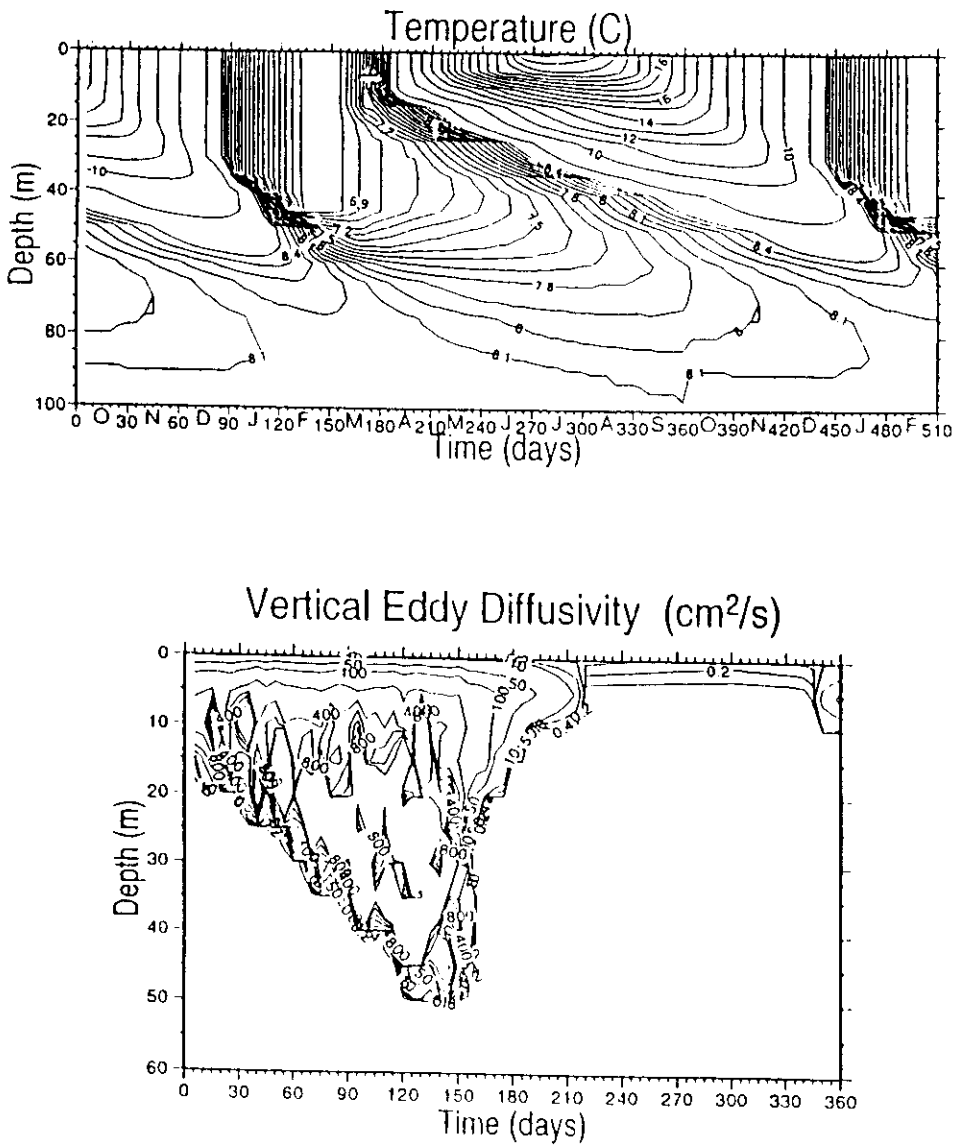

Figure 5.1 The depth and time variations of the (a) temperature (°C), and (b) vertical eddy diffusivity (cm^2/s).

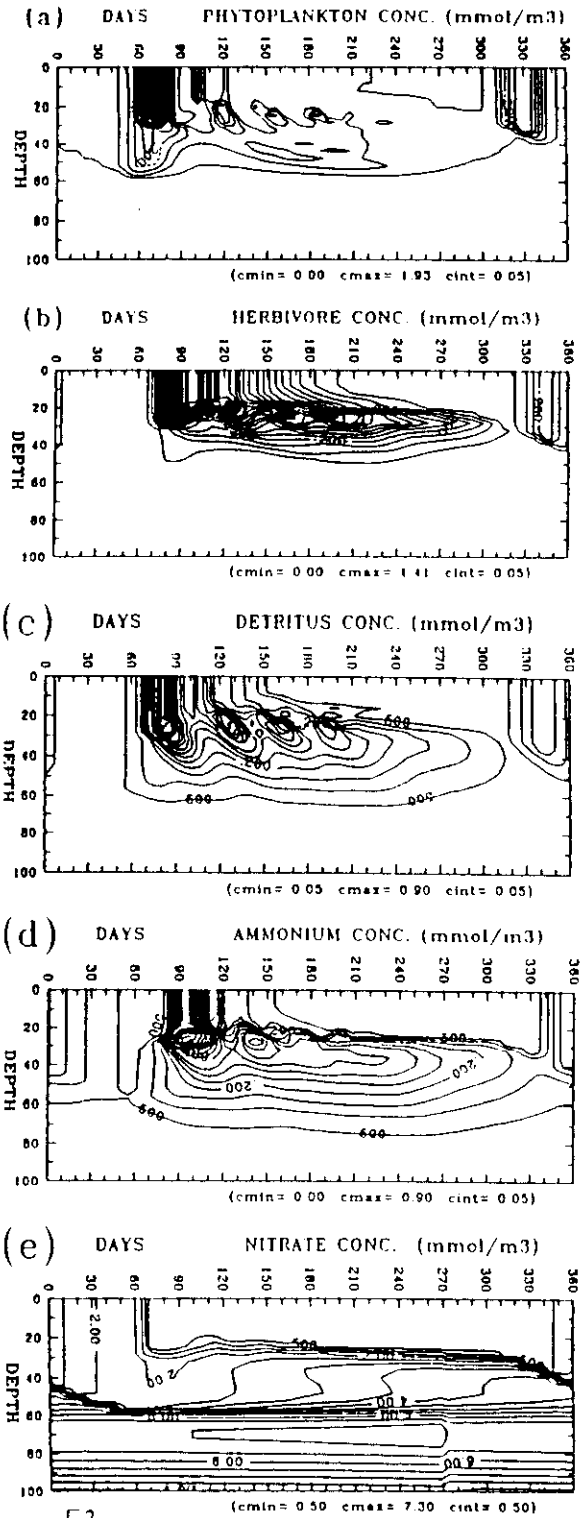

Figure 5. Depth and time variations of the (a) phytoplankton, (b) zooplankton, (c) detritus, (d) ammonium, and (e) nitrate concentrations (micromoles of N per cubic meter) computed by the model.

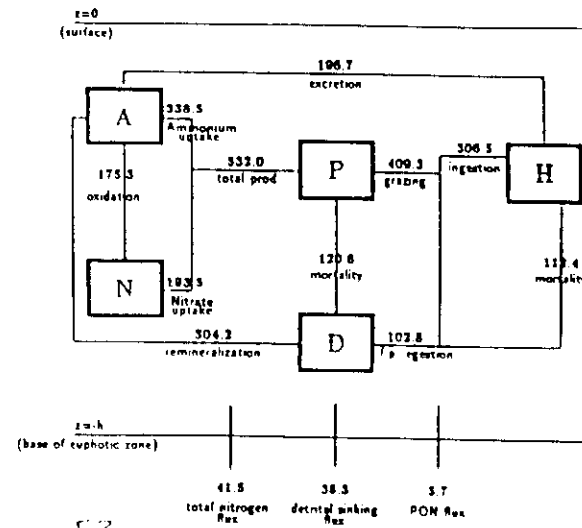

Figure 6. The annual nitrogen budget (micromoles of N per square meter per year) in the euphotic zone. PON is particulate organic nitrogen.

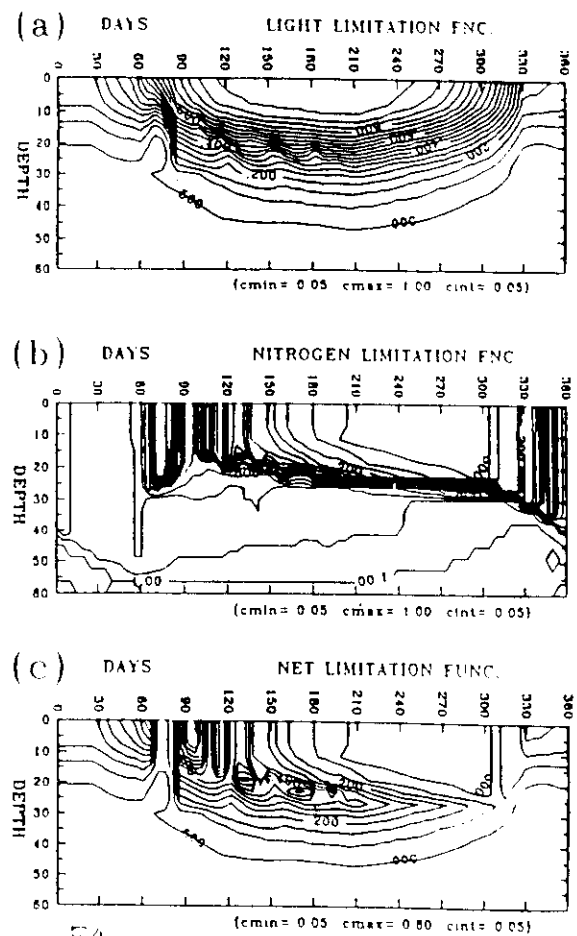

Figure 7. The depth and time variations of the (a) nondimensional light limitation function, (b) nondimensional nutrient limitation function, and (c) the net limitation function within the year.

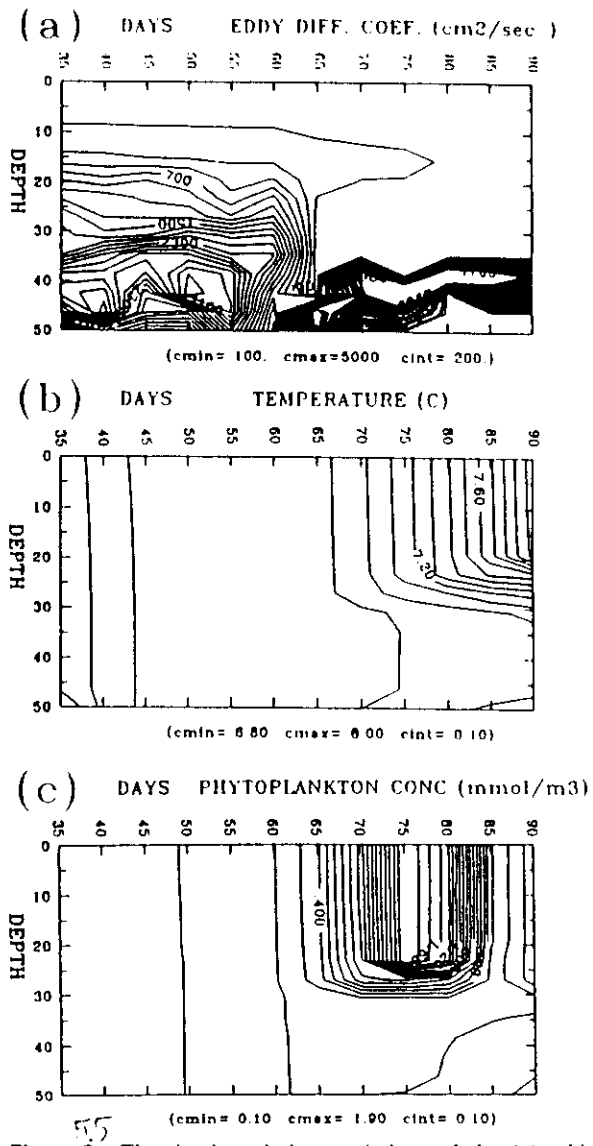

Figure 8. The depth and time variations of the (a) eddy diffusion coefficient (square centimeters per second), (b) temperature (degrees Celsius), and (c) phytoplankton concentration (micromoles of N per cubic meter) during the February–March period.

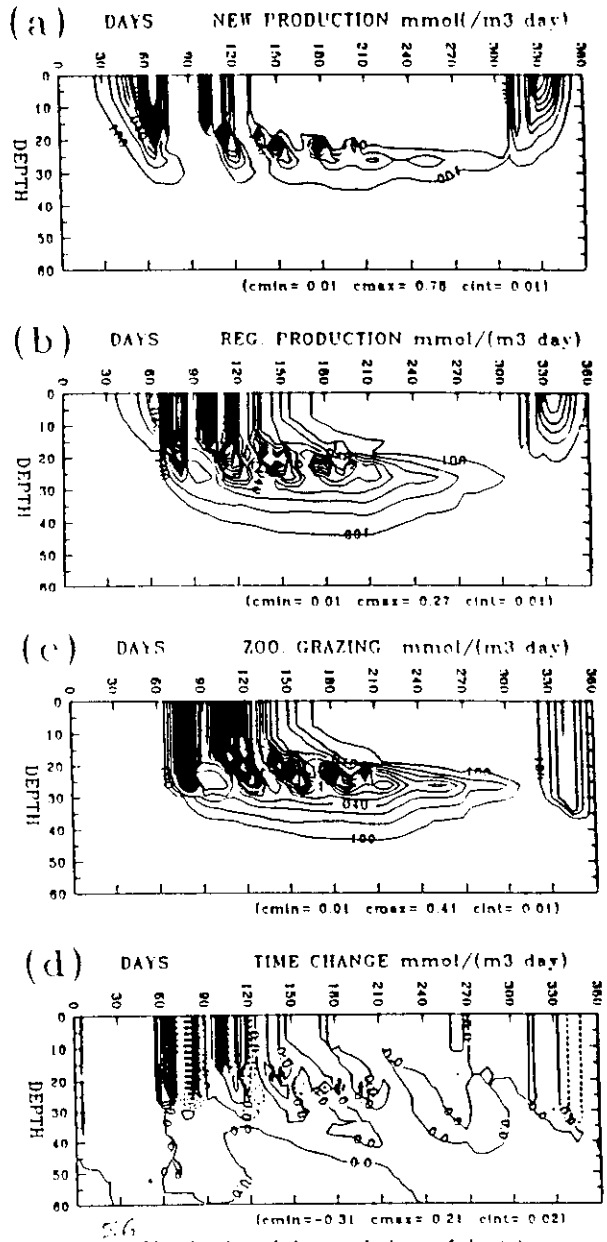

Figure 9. The depth and time variations of the (a) new production, (b) regenerated production, (c) zooplankton grazing, and (d) time change of phytoplankton (micromoles of N per cubic meter per day).

5.2 Application of Oguz et al (1996) One-Dimensional, 5 Compartment model to the Eastern Mediterranean

The Ionian and Rhodes basins (Fig. 5.7a,b) reflect two constrasting ecosystems; while the former represents a typical oligotrophic environment, the latter is known to be one of the most productive region of the Mediterranean Sea. These two basins also differ substantially by their dynamical regimes which govern ultimately their ecosystem characteristics. The Ionian Sea, identified as the region from the Sicily Strait to the Cretan passage, is a transition basin across which different water masses (e.g. Modified Atlantic Water, MAW; Levantine Intermediate water, LIW; Eastern Mediterranean Deep Water, EMDW) undergo transformations along their pathways between the Eastern and Western Mediterranean . At the near-surface levels which is the most important part of the water column with regard to the biological production, the MAW enters the western Ionian basin advected by the Atlantic Ionian Stream (AIS) which steers northward along the steep topographic slope on the eastern side of Sicily. The AIS jet then bifurcates at ~37°N, 17°E into two branches. The first branch turning directly southward encloses multiple centers, forming an overall anticyclonic area in the western Ionian basin. The second AIS branch extends further into the northeastern Ionian, and then turns southward and crosses the central Ionian basin meridionally as the intense mid-Ionian jet, which finally flows across the Cretan passage as the Mid-Mediterranean Jet. A scheme of these circulation features is shown in Fig. 5.7a. The existing information on the biochemical characteristics of the Ionian basin is very poor.

The Rhodes cyclonic gyre is, on the other hand, the most persistent feature of the Levantine basin circulation located in the northern Levantine basin to the west of Cyprus (Fig. 5.7b). Its dynamical and chemical characteristics are reasonably well-explored by a series of systematic surveys of the R.V. Bilim during the last decade. As far as the nutrient and chlorophyll properties are concerned, the data set is quite sufficient to calibrate and validate the model results.

The physical model is forced by daily climatological atmospheric fluxes. The heat flux data is adjusted slightly to provide the zero annual mean over the year, even though this net zero balance may be in contradiction with the actual negative heat budget measured for the entire Mediterranean as well as for its Western and Eastern sub-basins. This adjustment is however necessary to avoid the drift of the model from its perpetual state due to continuous warming/cooling of the water column during the time integration of the temperature equation.

Although the atmospheric forcing functions used in the model are rather idealized, they are adequate for the purpose of the present work since the surface layer dynamics is introduced to the biological model only indirectly by specification of the vertical eddy diffusivity. There is no other feed back mechanism between the physical and biological models.

Simulation of Rhodes Basin ecosystem

The annual variations of the temperature and sigma-t for the upper 150 m of the water

column are shown in Fig. 5.8a,b. The temperature structure (Fig. 5.8a) exhibits all the major features of its observed variations in the Rhodes gyre during the summer and winter months. Starting with the autumn season, the water column begins to cool gradually and, at the same time, homogenizes to greater depths as a result of convective overturning induced by the atmospheric cooling. At the end of January, the mixed layer water temperature is around 15.0°C and the mixed layer thickens to the depth of 100 m. In February, the temperature attains its lowest value of about 14.3°C, and the mixed layer homogenizes throughout the water column of 400 m taken as the lower limit of the model. The corresponding density of this water mass is 29.19 kg/m^3 (Fig. 5.8b) which, together with the temperature, represent typical characteristics of the LIW known to be formed in the gyre during the winter months. With our given idealized atmospheric forcing, cooling of the water column continues until mid-March after which the warming season starts and the seasonal thermocline begins to establish during spring and summer months. The surface temperature increases up to 24.5°C during August, whose corresponding density value is about 26.5 kg/m^3. The seasonal thermocline is located at its shallowest position of 15-20 m depth during this period. Thus, the mixed layer in the model changes over a depth range between 20 m and 400 m, as shown in Fig. 5.9. The seasonal thermocline is followed by a 50 m deep highly stratified zone across which the temperature decreases below 15.0°C whereas the density increases to more than 29.1 kg/m^3. They represent typical characteristics of the LIW in this region.

The annual temperature and density distributions shown in Fig.'s 5.8a,b agree fairly well with the observations. We note that reproduction of such highly variable water column thermohaline structure is largely because of the implementation of a fairly sophisticated turbulence parameterization in the model.

In agreement with its vertical mixing and stratification characteristics, the water column nitrate structure undergoes considerable variations during the year (Fig. 5.10a). The mixed layer waters of the entire summer and autumn seasons are extremely poor in nutrients, and characterized by only trace level nitrate concentrations of about 0.1 mmol/m^3. The nitrate depletion arises due to lack of supply from the subsurface levels because of the presence of strong seasonal thermocline/pycnocline. The zone of high stratification below the seasonal thermocline (c.f. Fig. 5.8a,b) coincides with the strong nitrate variations (the so-called the nitracline). Approximately below 80-90 m depths, the nitrate attains its typical deep water values in excess of 5.0 mmol/m^3. This structure undergoes substantial modification during the winter months as the convective overturning mechanism brings the nitrate rich subsurface waters to near-surface levels. Under such conditions, nitrate concentrations attain their maximum values of 4.5 mmol/m^3 over the 400m deep homogeneous water column in February.

The phytoplankton structure exhibits a major algae production during the first half of March (Fig. 5.10b) immediately after the cessation of the strong mixing, shallowing of the mixed layer (c.f. Fig. 5.9) and higher rate of solar irradiance penetrating to deeper levels. Since the water column was already replenished by nitrate, all these conditions favor phytoplankton

bloom, shown in Fig. 5.10b as an exponential increase of algae concentrations during the second week of March. High nitrate concentrations, built up in the water column during the winter, lead to generation of a very intense bloom with maximum biomass of about 3.8 mmol/m^3. It extends to the depth of 120 m, but its major part is confined to the upper 65 m because of the increasing role of self-shading effect on the light limitation. Following a week-long intense period, the bloom weakens gradually within the last week of March and terminates completely by the end of that month.

The early spring phytoplankton bloom initiates other biological activities on the living and non-living components of the pelagic ecosystem. Soon after the termination of the phytoplankton bloom, mesozooplankton biomass increases up to 2.2 mmol/m^3 during April (Fig. 5.10c). This period also coincides with increased detritus and ammonium concentrations (Fig. 5.10d,e) supported by excretion and mortality of phytoplankton and mesozooplankton communities. The major detritus accumulation in the water column in fact proceeds termination of phytoplankton bloom at begining of April. Moreover, sinking particles are remineralized completely within the upper 300 m before reaching bottom of the model at 400 m depth. All the detrital material is therefore preserved within the water column without any loss from the system. This is the reason for which the bottom boundary was taken at 400 m whereas the pelagic planktonic processes are confined within the upper 100 m of the water column.

The role of remineralization responsible for transforming the particulate organic nitrogen to inorganic dissolved nitrogen is indicated by increased ammonium concentrations up to 0.7 mmol/m^3 in March-April period in Fig. 5.10e. Its eventual oxidation due to nitrification process leads to nitrate accumulation primarily in the mixed layer and to a less extent in the nitracline, and causes a short-term increase in phytoplankton biomass up to about 0.5 mmol/m^3 within the mixed layer during the first half of May (Fig. 5.10b). As in the previous case, this secondary bloom is also followed by a small increase in mesozooplankton biomass, as well as in detritus and ammonium concentrations. The surface-intensified phytoplankton bloom event continues below the seasonal thermocline for another month by consuming available nitrate and ammonium within the nitracline zone. The subsurface biomass diminishes gradually towards the end of July as the contribution of losses from mesozooplankton grazing and phytoplankton mortality exceeds production.

The annual phytoplankton structure exhibits another weak bloom from mid-December to mid-January. This is associated with the consumption of nitrate which are made readily available by the convective mixing initiated in the water column with the begining of cooling season. Once again, it is followed by increase in mesozooplankton stocks in January-February.

It is interesting to examine the role of the strength of atmospheric cooling on the phytoplankton production since this directly affects the intensity of vertical mixing in the winter months. We have therefore repeated the Rhodes simulation by halving the heat flux forcing over the entire year, and thus reducing the maximum cooling to 100 W/m^2. The comparision of the euphotic zone averaged total nitrogen concentration and phytoplankton biomass

with those of the previous case is shown in Fig. 5.11. As expected, the reduced cooling results in weaker vertical mixing in the water column and hence development of a shallower mixed layer and weaker entrainment. The mixed layer deepening is now limited to the upper 150 m depth. The maximum nitrogen concentration in the euphotic zone prior to the March bloom is reduced from 5 μM of the previous case to about 3 μM (Fig. 5.11a), giving rise to a weaker early-spring phytoplankton bloom confined more towards the free surface. The euphotic zone averaged phytoplankton biomass decreases from $\sim 2.5\mu M$ of the previous case to $\sim 0.8\mu M$ (Fig. 5.11b). As pointed out before, the reduced mixing also causes its earlier development by about 12 days. The significance of this solution is the possible interannual variabilities on the intensity of the phytoplankton bloom according to strength of winter atmospheric conditions. Milder and warmer winters should tend to generate sooner and weaker phytoplankton blooms.

Simulation of Ionian Basin ecosystem

The temperature and salinity distributions for the upper 150 m depth of the water column of the western Ionian Sea (Fig. 5.12a,b) exhibit considerable differences from those of the Rhodes basin, especially during the winter season. As compared to 400 m deep convection in the Rhodes case, the water column deepens at most to 100 m depth as shown by the 15°C isotherm in Fig. 5.12a and 37.8 isohaline in Fig. 5.12b, followed by a sharp salinity gradient zone at the base of the mixed layer. Atmospheric cooling can not make the water dense enough (over 29 kg/m^3) to break the pycnocline and mix to deeper levels because of the presence of the less saline MAW with 37.5 ppt in the near surface levels of the western Ionian Sea. The mixed layer deepening continues until mid-April, and the upper layer water column begins to shallow only after the end of April, as the heating begins to intensify over the region. The period from mid-March to mid-April constitutes a transition period with almost no cooling or heating. The water column physical properties of the Rhodes and Ionian basins reveal two further important differences. The first one is related with the water column stratification below the 100 m depth. The Ionian thermohaline structure reveals a strong stratification contrary to the vertically uniform conditions observed in the Rhodes gyre. The second difference is associated with the presence of relatively homogeneous properties from the seasonal thermocline to the 100 m depth in the Ionian gyre whereas the same zone is characterized by strong stratification in the Rhodes gyre. Fig. 5.13 displays the model simulated mixed layer temperature distribution together with the surface temperature data from all available observations.

Similar to their physical characteristics, a substantial difference in the water column nitrate structure of the western Ionian and Rhodes basins is indicated by Fig. 5.14a. The weak vertical mixing in the winter months imply lack of sufficient nitrate supply from the subsurface levels to support the biological production in the subsequent early spring season. Fig. 5.14a clearly shows no nitrate accumulation inside the mixed layer during the winter. Whatever nitrate is entrained into the mixed layer from the subsurface levels is consumed immediately in the phytoplankton production process. This is initiated during

mid-January and gradually increased to its peak at the end of February (Fig. 5.14b). The phytoplankton biomass can attain in this period only 0.25 mmol N/m^3 which is an order of magnitude lower than the typical spring bloom values of the Rhodes simulation. The degradation of the phyoplankton bloom occurs during March. April is the period of intense nitrogen cycling followed by surface-intensified regenerated production during early May and its continuation at the subsurface levels below the thermocline in June with the maximum biomass of 0.16 mmol/m^3. The response of subsurface production can be traced in the nitrate field by the slight increase of isolines during early summer period (Fig. 5.14a). The annual distribution of zooplankton stock (Fig. 5.14c) reveals maximum biomass value of about 0.15 mmol/m^3 within the year. This is again one order of magnitude smaller than the values given in the Rhodes simulations.

The way in which the intensity of vertical mixing controls timing of the early spring phytoplankton bloom was described in the previous section in the context of the Black Sea plankton production model. It was shown that even though the light and nutrient conditions may be favorable for initiation of the bloom in winter, it can be delayed depending on the intensity of the vertical mixing. In the absence of any zooplankton grazing pressure and other losses due to phytoplankton mortality and excretion during winter, the vertical mixing is the only sink term which can balance the production. The initiation of phytoplankton bloom therefore depends on the relative intensities of these two terms during winter-early-spring period. The biological production will therefore be initiated whenever the vertical mixing weakens and its magnitude is exceeded by that of the production term. In our simulations, the Rhodes case is a good example for the delay of the bloom until the weakening of the intense mixing event taking place during the winter. The Ionian case, on the contrary, favors biological conditions weakly-controlled by the vertical mixing. Thus, the bloom initiates earlier in winter and intensifies gradually until the net limitation factor $\Phi(I, N, A)$ attains its maximum value.

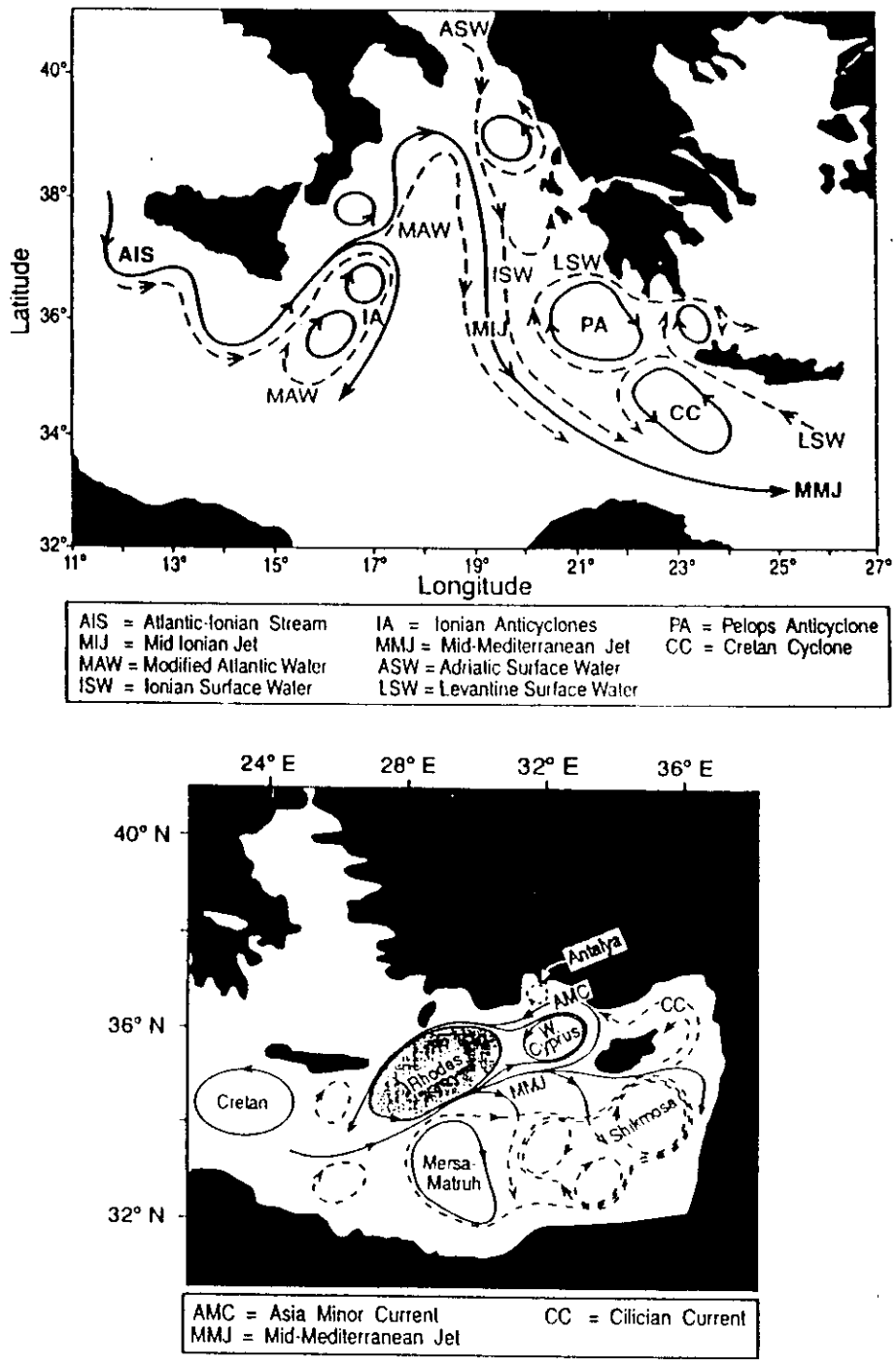

Figure 5.7 Schematic diagram of the upper thermocline circulation and water mass pathways in the (a) Ionian basin, (b) Levantine basin. The shaded areas signify the Rhodes and western Ionian gyres.

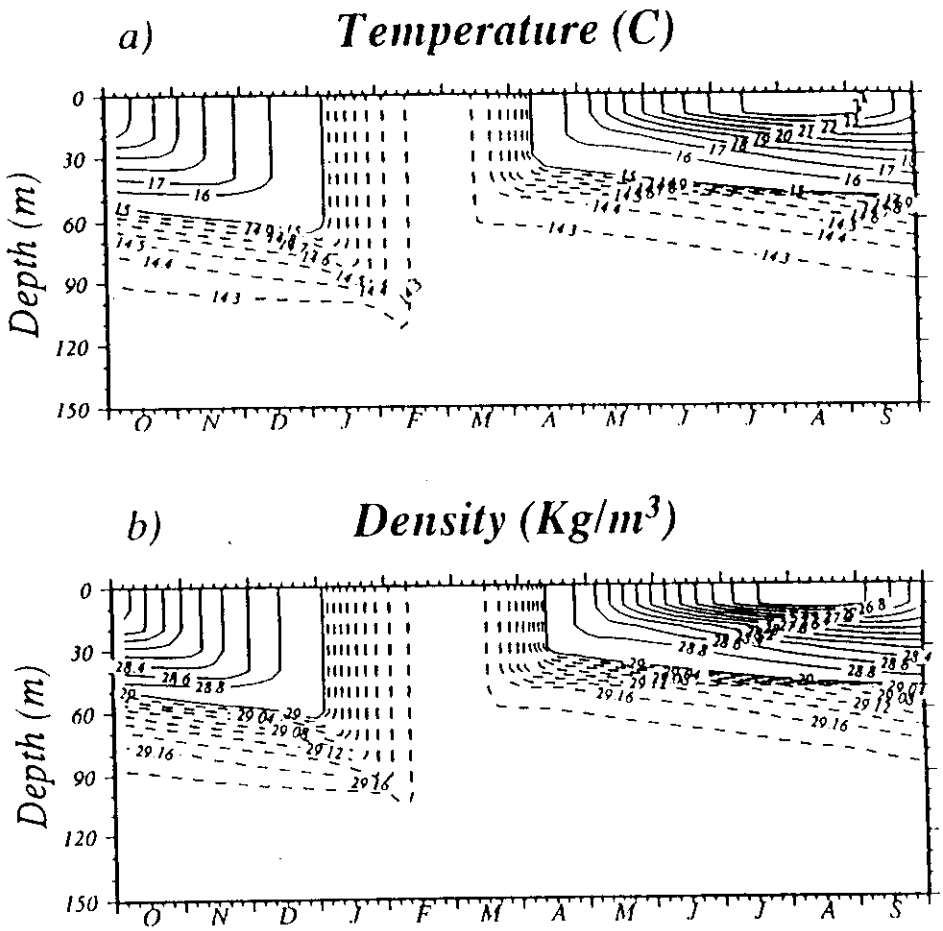

Figure 5.8 Simulated annual distributions of (a) temperature and (b) density within the upper 150 m depth of the water column. For temperature, contours with continuous lines are at intervals of 1° C, and with broken lines at 0.1° C. For density, contours with continuous lines are at intervals of 0.2 kg/m^3, and with broken lines at 0.02 kg/m^3. In both plots the time axis starts at October 1 and ends at September 30.

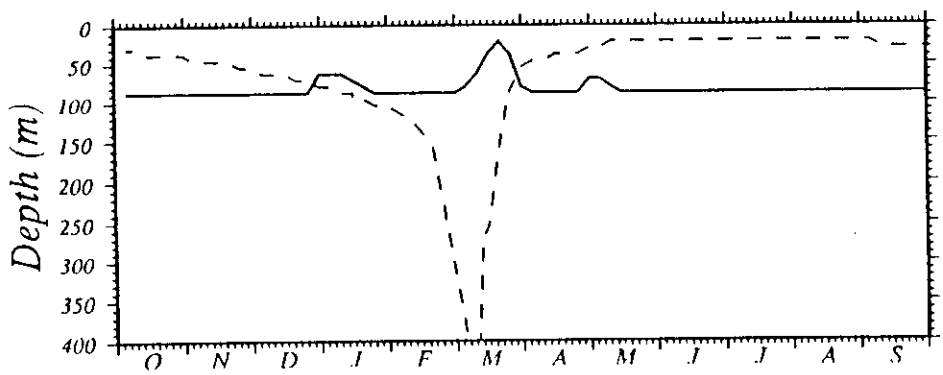

Figure 5.9 Simulated annual cycles of the mixed layer depth (broken line) and the euphotic zone depth (continuous line).

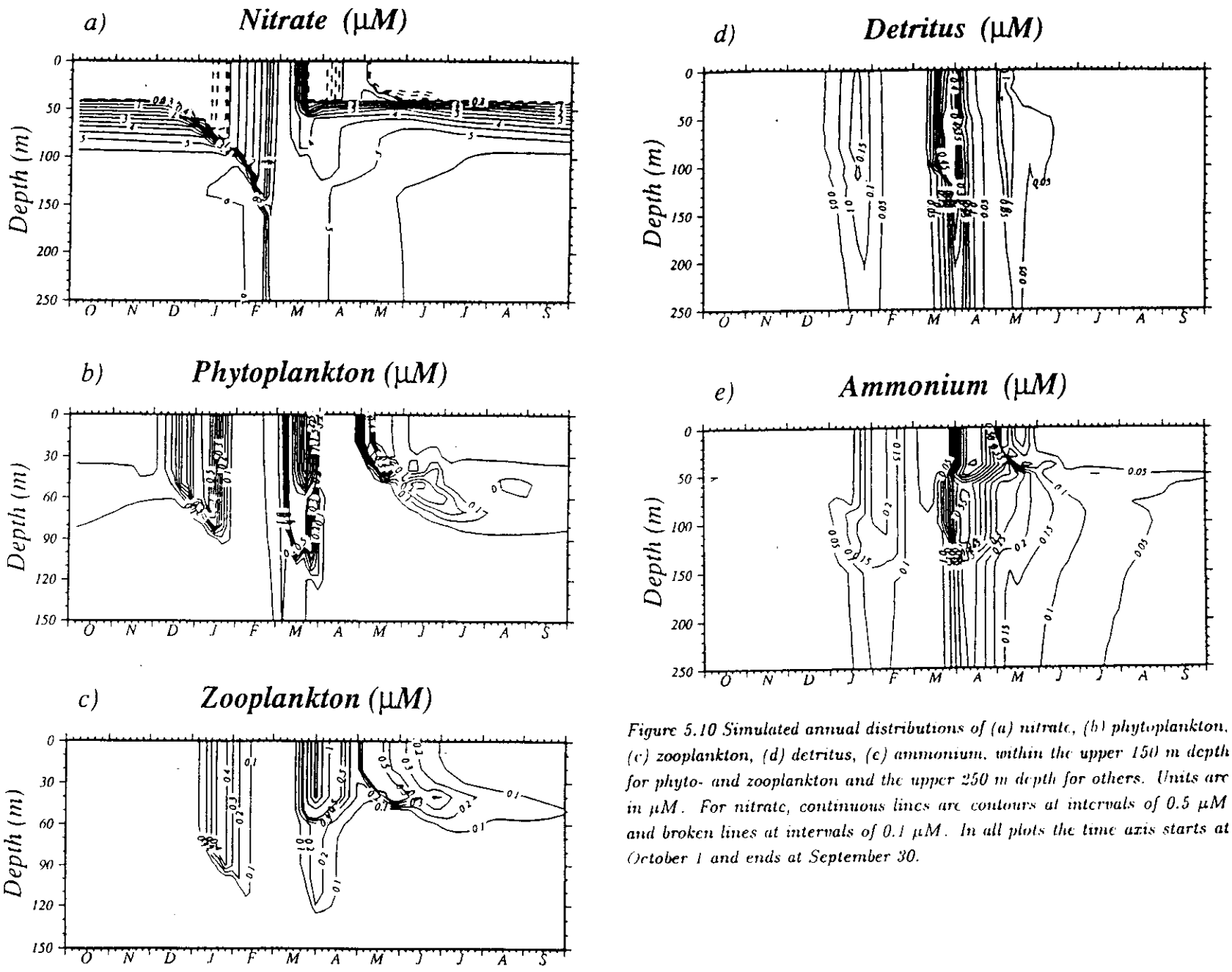

Figure 5.10 Simulated annual distributions of (a) nitrate, (b) phytoplankton, (c) zooplankton, (d) detritus, (e) ammonium, within the upper 150 m depth for phyto- and zooplankton and the upper 250 m depth for others. Units are in μM. For nitrate, continuous lines are contours at intervals of 0.5 μM and broken lines at intervals of 0.1 μM. In all plots the time axis starts at October 1 and ends at September 30.

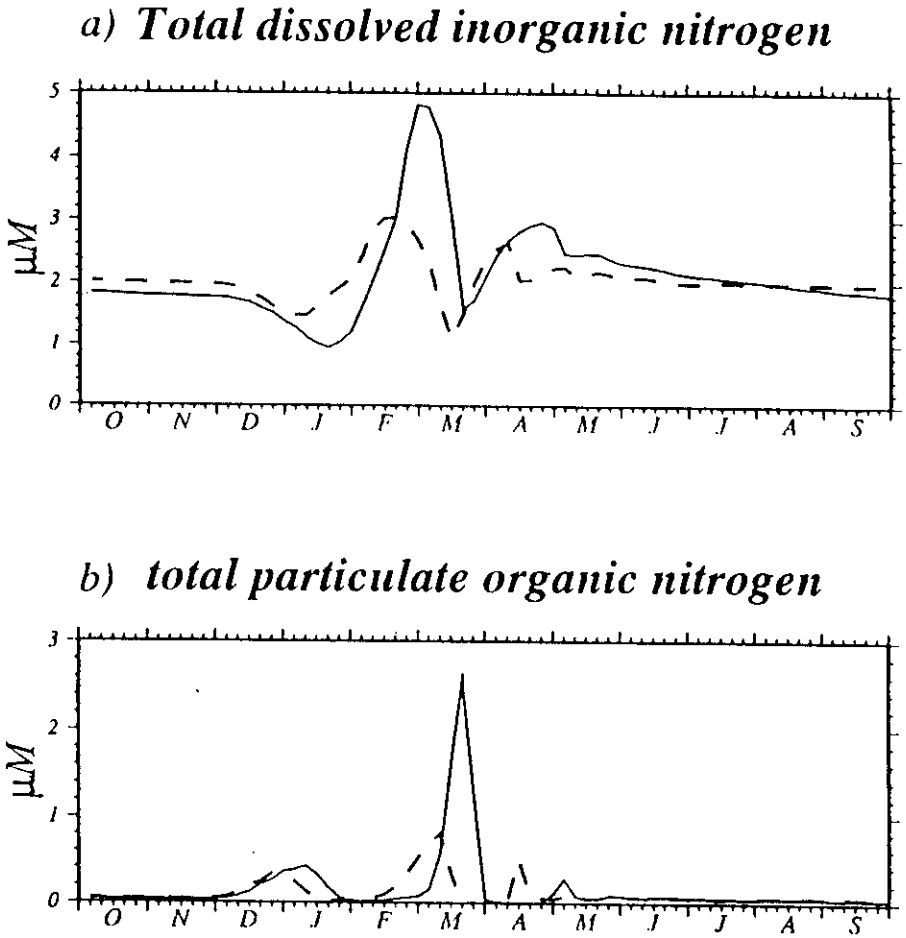

Figure 5.11 Simulated annual distributions of (a) total dissolved inorganic nitrogen, and (b) total particulate organic nitrogen averaged over the upper 100 m depth of the water column. The continuous line represent the solutions for the standard experiment and the broken lines for the experiment with the weaker heat flux forcing. The time axis starts at October 1 and ends at September 30.

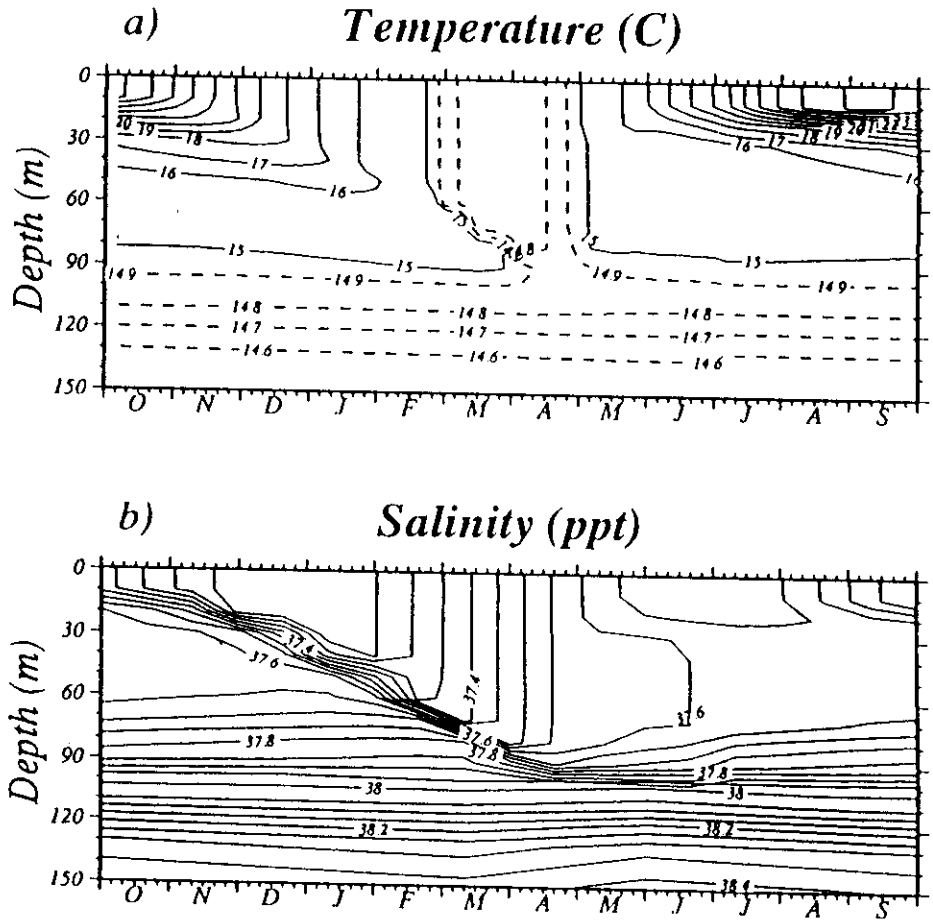

Figure 5.12 Simulated annual distributions of (a) temperature and (b) salinity within the upper 150 m depth of the water column. For temperature, contours with continuous lines are at intervals of 1° C, and with broken lines at 0.1° C. For salinity, contours are at intervals of 0.05 ppt. In both plots the time axis starts at October 1 and ends at September 30.

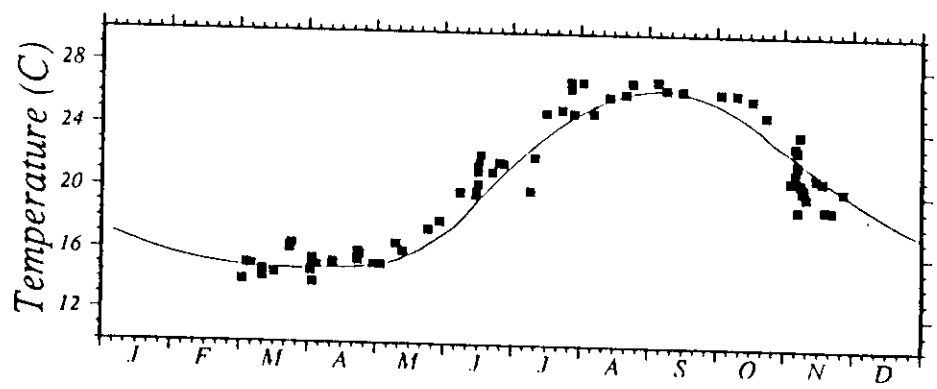

Figure 5.13 Simulated annual mixed layer temperature distribution for the western Ionian basin (continuous line) and the observed surface temperatures taken from Mediterranean Oceanographic Data Base system (solid squares) for the same region.

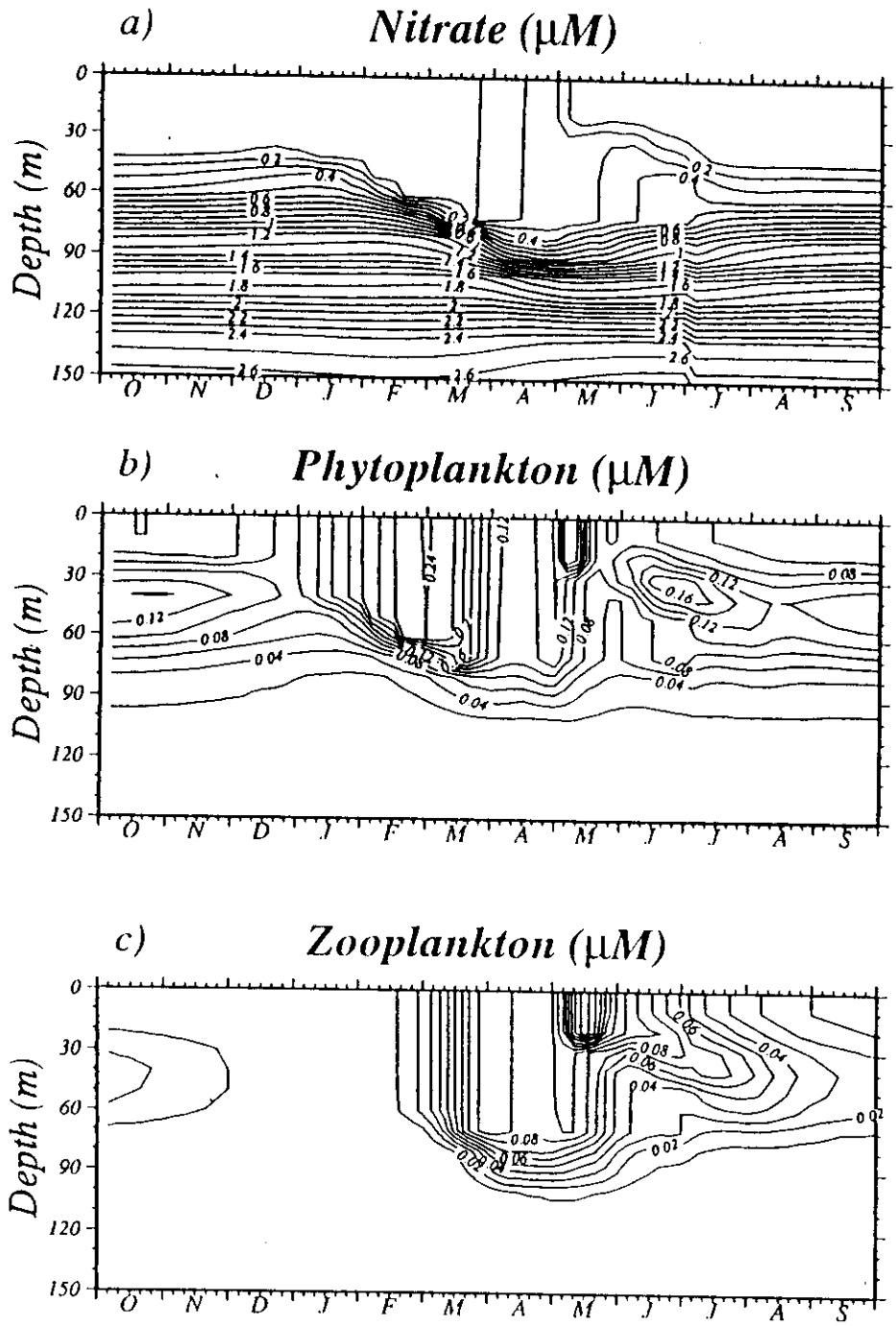

Figure 5.14 Simulated annual distributions of (a) nitrate, (b) phytoplankton and (c) zooplankton for the western Ionian basin within the upper 150 m depth of the water column. Units are in μM. For nitrate, the contours are at intervals of 0.1 μM, for phytoplankton at 0.02 μM and for zooplankton at 0.01 μM. In all plots the time axis starts at October 1 and ends at September 30.

5.3 Models of Primary Roduction dynamics in the Northwestern Mediterranean

Lacroix and Nival (1998) Model

It is very similar to the models described in the previous section. It is applied to the Ligurian Sea (Fig. 5.15) known as the region of deep convection, and one of the most productive area in the entre Mediterranean. Its biological module involves two phytoplankton groups (diatoms and flagellates), one zooplankton group (characterized mainly by copepods), particulate organic matter and dissolved inorganic nitrogen as being the limited nutrient (Fig. 5.16). The model formulation is very similar to that described in section 5.1. The model investigates the response of high variability on the meteorological forcing to primary productivity characteristics of the region. One of the model ezperiments is to simulate the 1985 conditions and compare the simulations with the observations.

The model is able to reproduce reliably the establishment and decay of the thermocline. During the autumn and the begining of the winter, the mixing leads to a cooling of the surface layer (Fig. 5. 17a,b). The mixed layer deepens to about 150 m in January and more in February and March. The intense winter mixing terminates towards the end of March and stratification begins to developed by April. Fig. 5.17c shows the temporal evolution of the turbulent diffusion coefficient. It is greater than 0.01 m^2/s during the major part of the winter (January to March) until about 150 m. In Fig. 5. 17d, we can see that the mixing depth reaches 150 m during this period. In April, the mixed layer depth decreases rapidly as a result of the weakeninfg of the vertical mixing, as shown in Fig. 5.17c. From May to September the strong warming causes establishment of a strong stratification in the upper layer water column. The mixing depth varies typically from surface to 15 m, except in the mid-june and in August where it reaches, respectively, 30 m and 25 m in response to short term wind events. In October, as the wind stress increases and the heat flux (warming) decreases, the mixing depth begins to increase. This leads to the destabilization of the seasonal thermocline.

The results of the biological model are presented in Fig. 5.18. Fig. 5.18a shows the replenisgment of dissolved inorganic nitrogen (DIN) during the winter caused by the strong mixing. It is followed by a depletion in the surface layer in relation to the uptake by phytoplankton. DIN concentrations remain rather weak ($<$0.5 $mmol/m^3$) in the surface layer during all the year. At the end of the year, a slight increase in the DIN concentrations dy diffusion takes place in the surface layer, but this is not very clearly seen in the figure because this process is masked by phytoplankton nutrient uptake (see Fig. 5.18d).

Fig. 5.18b,c show diatom and flagellate biomass distributions, respectively. The diatoms begins to grow in January (following the increase in solar radiation) and reach a maximum at the end of March as a consequence the replenishment of nutrients. During the spring bloom, the maximum biomass can cover the upper 50 m deep layer (around 0.5 $mmol/m^3$). The diatom biomass of 0.2 $mmol/m^3$ can be found to about a depth of 200 m. From early April, when the nutrients become rare, the diatom biomass decreases in the surface layer.

The flagellates are present during the major part of the year, but they reach a maximum biomass in the summer (June-October). A slight increase in biomass is observed at the begining of the year. At this moment, the competition between diatoms and flagellates turns to the advantage of the diatoms since they have a larger growth rate. In the summer, when the surface nutrients become rare, the flagellates gradually replace the diatoms as they can feed on nitrogen coming from excretion and mineralization. The flagellate maximum biomass during the summer (0.3 mmol/m^3) is confined between the depth of 50 and 100 m following the nutrient distribution. In December, the supply of nutrients resulting from the mixing leads to an increase in the flagellate biomass, whereas this nutrient supply is too weak to reinitiate an increase in the diatom biomass. The diatoms start growing during February.

Fig. 5.19 shows the total gross primary production. This begins in January following the solar radiation increase and reaches a maximum (6 mg C m^{-3} day^{-1}) at the end of March in the first 50 m. During the summer, the primary production is only observed between 50 and 100 m, where nutrients are not totally depleted. at the end of the year, the supply of nutrients by diffusion allows the primary production to increase. The total gross primary production integrated over 200 m computed by the model for the year 1985 is 46 g C m^{-2} year^{-1}. This is weaker than the measured value of 180 g C m^{-2} year^{-1} during the year 1986.

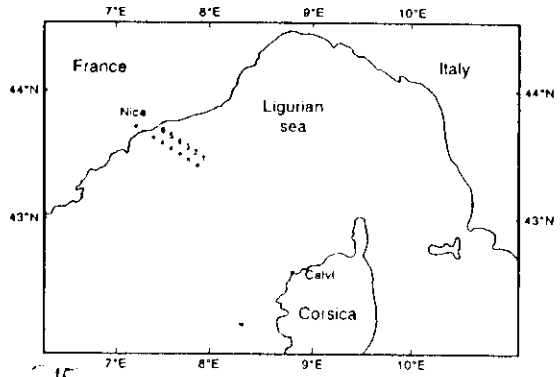

Fig. 1. Map of the Ligurian Sea (North Western Mediterranean Sea) showing the position of FRONTAL stations (1-6) along the Nice-Calvi transect.

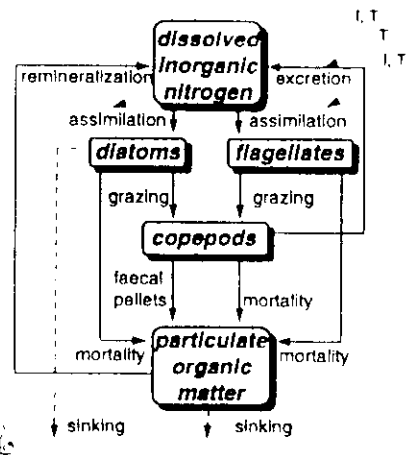

Fig. 3. Representation of interactions between biological state variables.

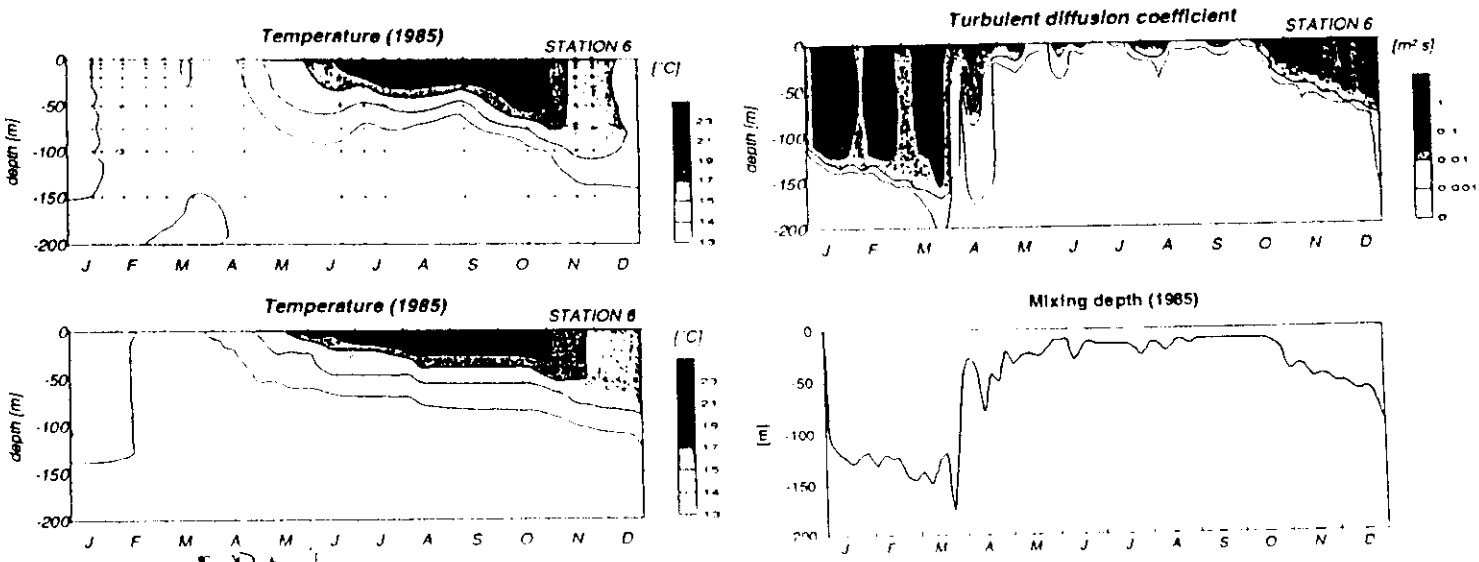

Fig. 4. (a) Temperature (°C) at station 6 during FRONTAL missions (following data from Nival et al., 1989) – dots represent data points. (b) Temperature (°C) computed by the model with meteorological conditions for 1985. (c) Turbulent diffusion coefficient (m^2 s^{-1}) computed by the model with meteorological conditions for 1985. (d) Mixing depth (m) computed by the model with meteorological conditions for 1985.

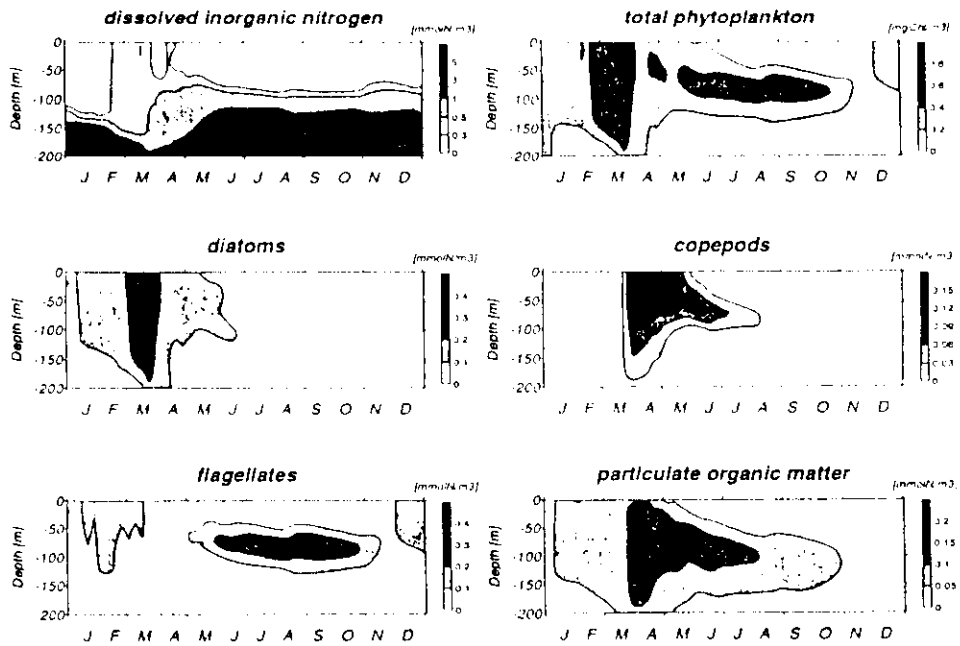

Fig. 5. Biological state variables computed by the model with atmospheric conditions for 1985. From upper left to lower right panels: dissolved inorganic nitrogen, diatoms, flagellates, total phytoplankton, copepods and particulate organic matter.

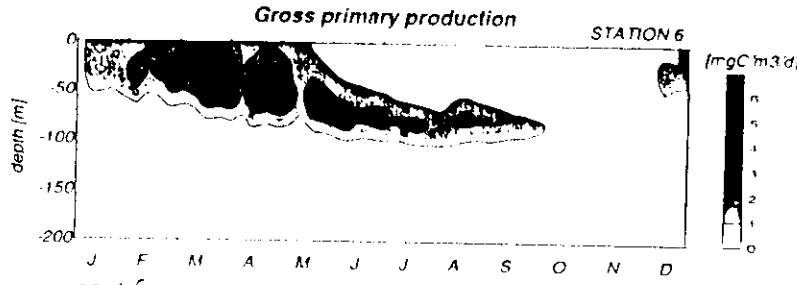

Fig. 8. Gross primary production (mg C m^{-3} day^{-1}) computed by the model

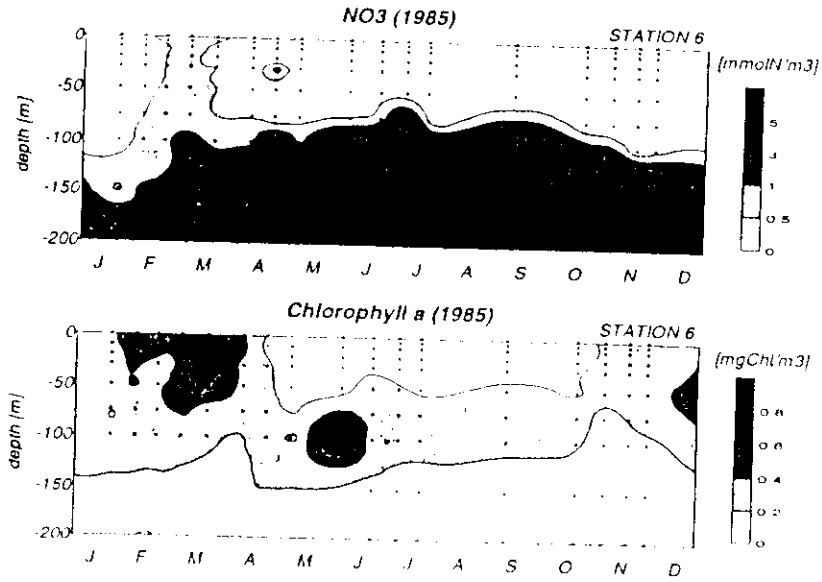

Upper panel: nitrate (mmol N m^{-3}) at station 6 during FRONTAL missions. Lower panel: chlorophyll a (mg Chl m^{-3}) at station 6 FRONTAL missions. Dots represent data points. Following data from Nival et al. (1989)

Levy et al (1998) Model

A slightly more complex model is used to study the annual plankton production characteristics for the same region using the data from 1991. The region of interest and the schematic representation of the model structure are shown in Fig's 5.20 and 5.21, respectively. The model involves a single phytoplankton group, two zooplankton groups (microzoo- and mesozoo-), bacteria, two groups of detritus (small and large particulate organic materials), dissolved organic material (DOM), ammonium and nitrate. The physical model involves the mixed layer dynamics similar to the one decsribed earlier by Oguz et al. (1996). The model is forced by 1991 atmospheric forcings (the wind stress and heat flux). The resulting temperature structure over the year (Fig. 5.22a) reproduce rather well most of its observed characteristics (Fig. 5.22b). In winter, the temperature is uniform in the water column and below 13 °C. In spring, isotherms rapidly deepen as the water column is stratified due to the onset of warming in the water column. Between the spring and summer, the progressive warming of the surface induces maximum stratification of the water column. Destratification in fall is more progressive than the stratification in spring. The model, however, predicts a more diffusive summer thermocline as compared with the data. This suggests that the turbulent diffusion coefficient computed by the model might be overestimated for summer conditions. The simulated mixed layer is also in good agreement generally with the mixed layer estimated from in situ density profiles (Fig. 5.23).

The time evolution of the simulated nitrate, phytoplankton and chlorophyll are shown in Fig.s 5.24a, 5.25a,b, respectively. Phytoplankton evolution is mainly controlled by nutrient and light (mixed-layer depth) availability, and grazing. From mid-January to the end of February, nutrients that have been brought up to the surface by winter mixing are fully available (Fig. 5.24a), and the strong and permanent mixing inhibits photosynthesis. It is a typical winter regime. As soon as the water column is stratified (i.e. the mixed layer shallows; Fig. 5.23) phytoplankton start to grow and a bloom occurs, followed by a strong microzooplankton production (Fig. 5.26a) about a month later, and mesozooplankton production one month after that (Fig. 5.26b). A high biological production taking place in spring and early summer gives rise to maximum phytoplankton debris (POM) in March-april, and highest zooplankton debris in late June and July.

In summer and early autumn, the system has an oligotrophic character, with surface depleted nutrients (Fig. 5.24a), a subsurface phytoplankton production below the seasonal thermocline (Fig. 5.25a,b). Destratification causes new nutrient supply and a late autumn secondary bloom as also seen in the observations.

Above 50 m, the model simulates a strong nitrate depletion in April, followed by an increase in nitrate concentrations in May. The depletion is correlated to the spring phytoplankton bloom. The increase in May is due to nitrification, the major nitrate source at this time of the year.

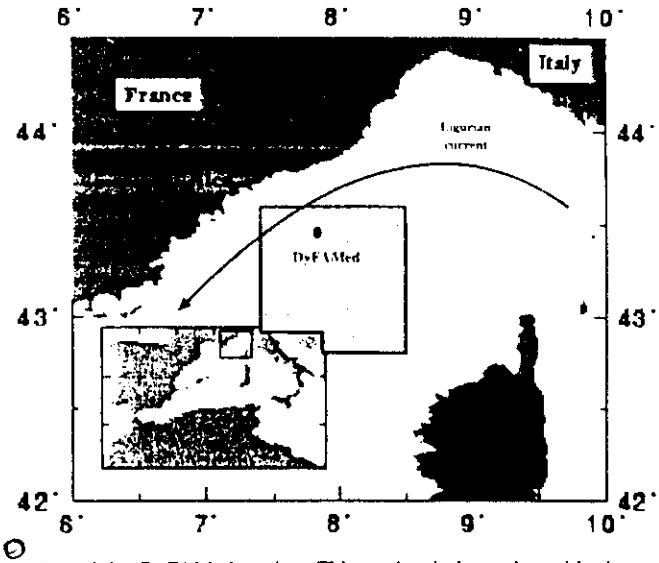

Figure 1. Location of the DyFAMed station. This station is located outside the coastal Ligurian current, and is typical of the offshore Northwestern Mediterranean Sea. The main cyclonic circulation is shown by arrows. The area over which ECMWF atmospheric model heat flux and wind data have been extracted for the use of this study is shown by the speckled square.

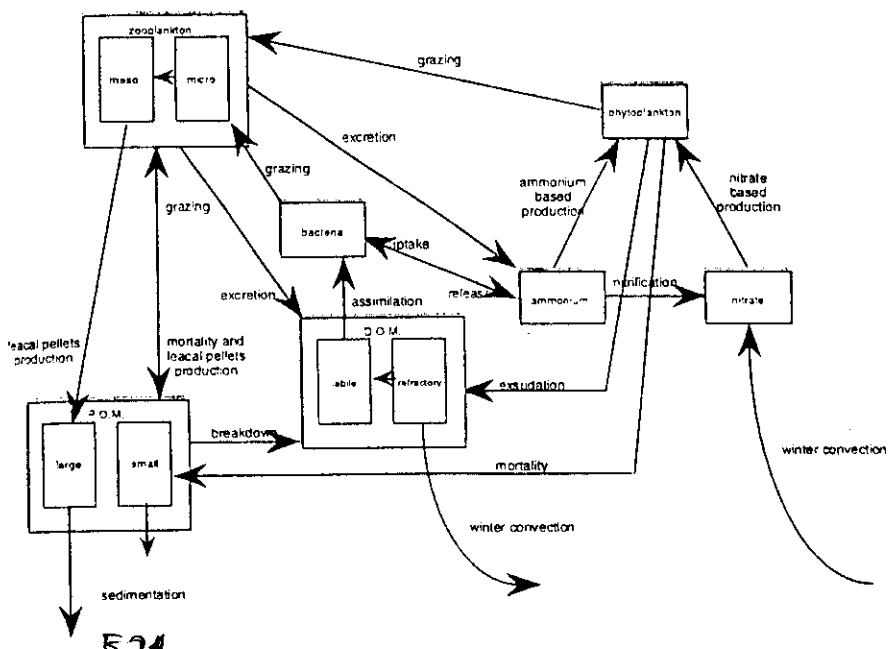

Figure 2. Schematic representation of the compartments and processes of the BIOMELL.

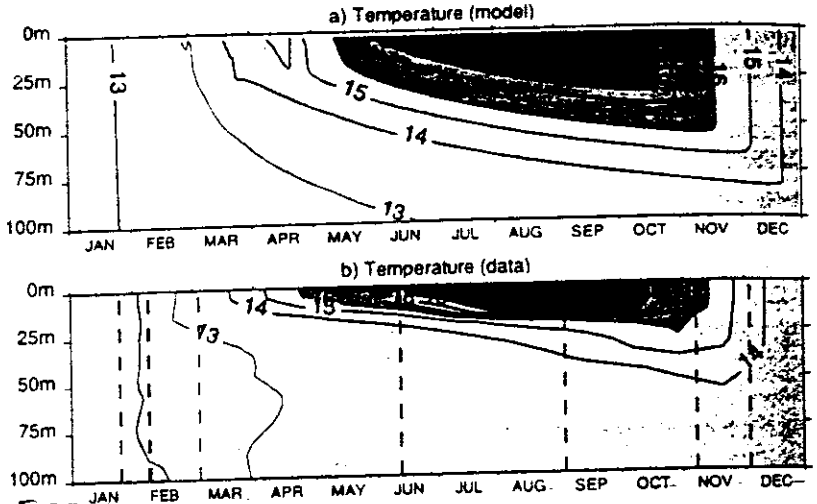

522

Figure 4. (a) Simulated temperature for 1991. (b) Temperature data measured at the DyFAMed station in 1991, interpolated in time and depth. Dotted lines show the eight measured profiles.

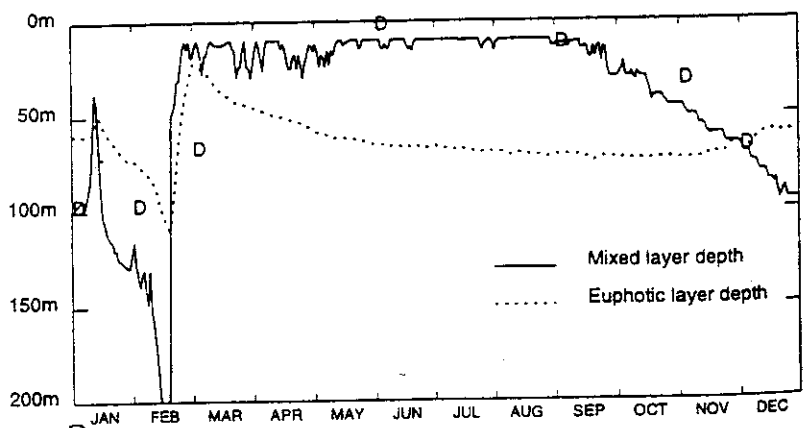

523

Figure 8. Simulated mixed layer depth (solid line, using the criteria that $k_z > 10^{-5}$ m^2 s^{-1}) and euphotic layer depth (dotted line, 1% of incident illumination). Mixed-layer depth estimates from CTD data (using the criteria that the density gradient between the surface and the base of the mixed layer is 0.05) are shown by the capital letter D.

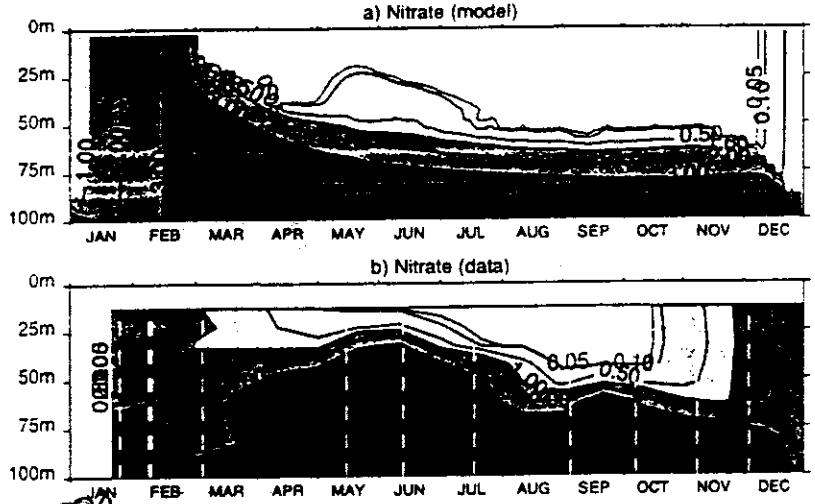

524

Figure 6. (a) Simulated nitrate for 1991. (b) Nitrate data measured at the DyFAMed station in 1991 (with a detection limit of 0.05 mmole N m^{-3}) interpolated in time and depth. Dotted lines show the ten measured profiles. (c) Simulated nitrate in a sensitivity experiment where nitrification is not accounted for. Units are mmole N m^{-3}.

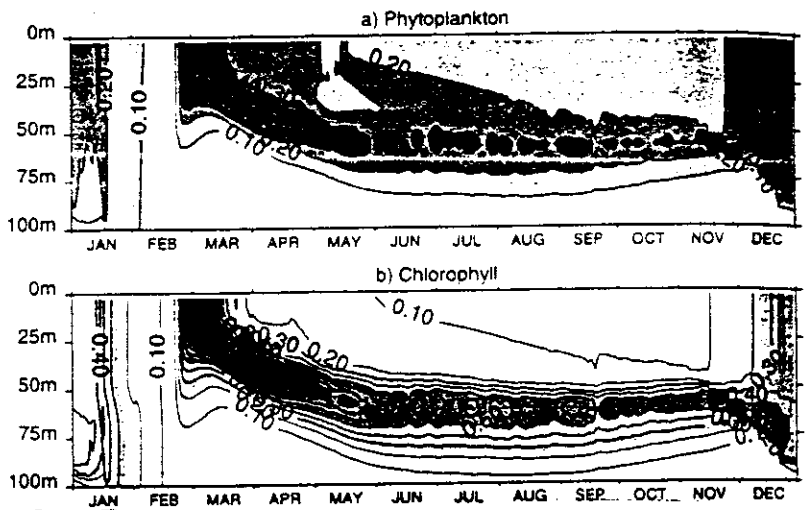

525

Figure 7. Annual cycle of simulated (a) phytoplankton (in mmole N m^{-3}), (b) chlorophyll (in mgChl m^{-3}) and (c) C:Chl ratio (in mgC(mgChl)$^{-1}$) for 1991.

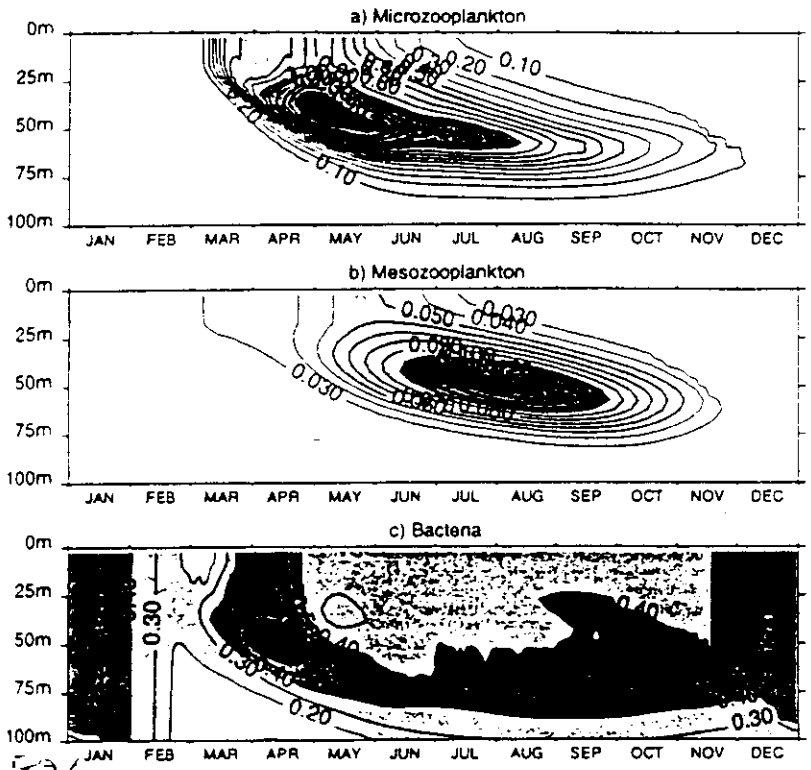

Figure 8. Annual cycle of simulated (a) microzooplankton, (b) mesozooplankton and (c) bacteria for 1991. Units are mmole N m^{-3}.

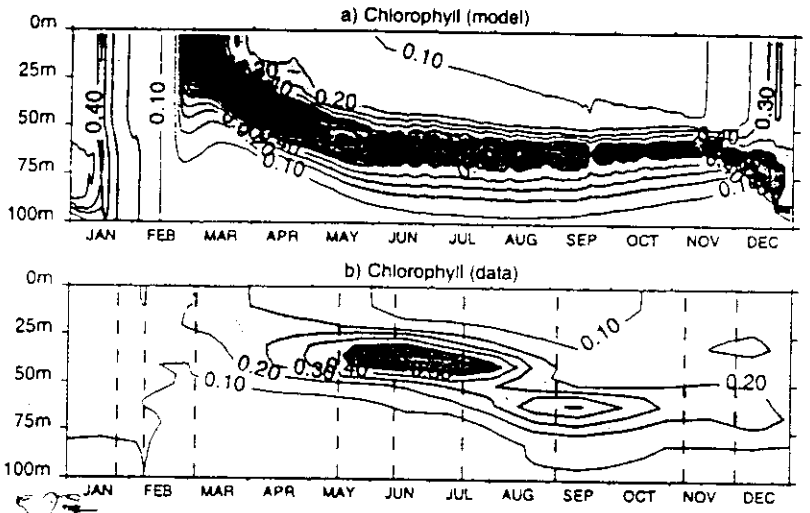

Figure 9. (a) Simulated chlorophyll for 1991. (b) Chlorophyll data measured at the DyFAMed station in 1991, interpolated in both time and depth. Dotted lines show the nine measured profiles. Units are in mgChl m^{-3}.

5.4 Multi-layer biological model coupled with mixed layer dynamics

In one dimensional water column models, fine resolution of the vertical biochemical structure by a sufficiently high number of vertical levels can be afforded easily. But, it becomes a formidable task in the three dimensional context, because of the amount of computational time involved for such simulations. Furthermore, since biological models contain a large number of externally-specified parameters, such three dimensional simulations need to be repeated many times in order to explore sensitivy of results to key parameters. Therefore, development of a three dimensional biochemical model of intermediate complexity between complex and computationally expensive multi-level models and oversimplified mixed-layer models is highly desirable to study efficiently the basinwide variability of the plankton production, related processes and their interactions with the mesoscale dominated circulation dynamics in the Black Sea. A recent example of this approach was given by McCreary et al. (1996) for studying the biological activity in the Arabian Sea.

Here we give an example of this approach for the Black Sea. The three layer idealization of its vertical biogeochemical structure is shown in Fig. 5.28a,b. The first two layers comprise the euphotic zone where the main pelagic food web cycling occurs. The third layer signifies the aphotic layer extending from the base of the euphotic layer to the anoxic interface. This layer is denoted here as the "chemocline zone" (Fig. 5.28a).

The first layer characterizes the seasonally varying "mixed layer", regulated by the atmospheric forcing. The second layer represents the water column below the seasonal thermocline up to the base of the euphotic zone, and is referred to as the "intermediate layer". Its thickness varies during the year depending on the vertical structure of the solar radiation. The euphotic zone attains a thickness of at most 50 m in the Black Sea. The mixed layer may deepen below this layer under the conditions of strong surface cooling and/or wind forcing during some periods of the winter season. Under such conditions, the mixed layer depth is set to the euphotic zone depth. The biological model then reduces to a two-layer case with vanishing the intermediate layer (see Fig. 5.28b).

In such a simplest possible idealization of the vertical biogeochemical structure of the upper layer water column in the Black Sea, the first two layers represent the region of plankton production and organic matter generation. The third layer acts as the principal nitrate pool where the sinking particulate material are constantly remineralized and converted to inorganic nitrogen form. The subsurface nitrate will then be made available for plankton production when they are entrained and/or diffused into the euphotic zone.

The biological structure of the model is described by two phytoplankton (diatoms and flagellates) and two zooplankton groups (microzoo- and mesozoo-), detritus, ammonium, and nitrate. Particulate organic detritus is assumed to be converted directly to ammonium without explicitely considering the microbial loop mediating the remineralization process.

The necessity of having at least two different phytoplankton groups in order to represent properly the annual variations of phytoplankton standing stock in the euphotic zone was noted earlier. The diatoms typically grow in nutrient-rich conditions of the early spring

period following the intense winter mixing in the water column. As the nutrient content in the mixed layer is deprived gradually in spring, diatom blooms are replaced by the growth of flagellates in warmer and relatively poor nutrient environment using the regenerated nutrients in the euphotic zone. In the model, diatoms are mainly consumed by mesozooplankton whereas microzooplankton are fed on dinoflagellates with a greater efficiency as compared with the diatoms.

The local temporal variations of all biological variables are expressed by advective-diffusive equations of the general form (McCreary et al., 1996)

$$\frac{\partial F_i}{\partial t} + \mathbf{v_i} \cdot \nabla F_i = A_h \nabla^2 F_i + \frac{Q_i}{H_i} + \Re_i \qquad (i = 1, 2, 3) \tag{24}$$

which implies that the local changes in the plankton biomass and nutrient concentrations occur as a result of horizontal advection and diffusion, vertical mixing associated with the entrainment process and turbulent diffusion and a series of particular biological processes. In eq. (24) F_i is the concentration of any biological variable in layer i, $\mathbf{v_i}$ is the horizontal velocity field, H_i is the layer thickness, $\Re_i$ and Q_i are the biological source-sink and vertical flux terms, respectively. A_h denotes the horizontal diffusion coefficient, t is time, ∇ is the horizontal gradient operator and ∂ represents the partial derivative. In the presence of finite intermediate layer (i.e when $H_2 > 0$), interfacial transports are given by

$$\begin{aligned} Q_1 &= (F_2 - F_1)\left[w_e^* + K_{21}\right], \\ Q_3 &= -(F_3 - F_2)\, K_{32}, \\ Q_2 &= -(Q_3 + Q_1) \end{aligned} \tag{25}$$

In the case of vanishing H_2 (i.e. no intermediate layer, and the mixed layer comprises the entire euphotic zone), the model reduces to a two layer case in which the interfacial transports are

$$Q_1 = -Q_3 = (F_3 - F_1)\left[w_e^* + K_{31}\right] \tag{26}$$

In these equations, the terms proportional to w_e^* and K_{ij} parameterize the transports across the layer interfaces due to entrainment and vertical diffusion, respectively. We note that the turbulence is generated only within the mixed layer by means of the surface buoyancy fluxes and the wind stress. Thus, there is no entrainment flux across the interface between the second and third layers. Furthermore, the chemocline layer is completely decoupled from the anoxic pool below. This is accomplished by specifying the zero nitrate, ammonium and particulate organic matter fluxes at the base of the third layer. This assumption implicitely specifies a complete remineralization without any loss of organic material to deep basin across the anoxic interface. w_e^* is expressed by

$$w_e^* = max\,(w_e, 0) \tag{27}$$

This specification of the entrainment velocity implies that concentrations in the mixed layer are unaffected by the processes of detrainment and the mixed layer shallowing. We consider

that this condition applies for all motile and non-motile state variables of the biological model, including zooplankton.

The entrainment velocity, w_e, is computed by the Krauss and Turner (1967) mixed layer model. Accordingly, the mixed layer entrains ($w_e > 0$) water due to vertical mixing maintained by turbulence generated at the sea surface. The total turbulent kinetic energy (TKE) production in the mixed layer is expressed by

$$PROD = mu_*^3 + \frac{1}{2}gH_1\left[\frac{\alpha Q_s}{\rho_0 C_p} + \lambda S_0\,(E-P)\right] \tag{28}$$

where $u_*^2 = |\tau|/\rho_0$ denotes the friction velocity with $|\tau|$ representing the magnitude of the wind stress, Q_s the net surface heat flux, $S_0\,(E-P)$ the net surface fresh water flux. The first term on the right hand side represents the TKE production due to work done by the wind stress, the second term is associated with the buoyancy production due to cooling ($Q_s > 0$) and net surface fresh water flux [$S_0(E-P) > 0$].

The case with $PROD > 0$ signifies the mixed layer deepening for which the entrainment rate is defined by

$$w_e = \frac{PROD}{[1/2gH_1\Delta\rho/\rho_0]} \tag{29}$$

where $\Delta\rho$ is the density contrast at the base of the mixed layer. The mixed layer thickness can then be computed by

$$\frac{dH_1}{dt} = \frac{\partial H_1}{\partial t} + \mathbf{v}_1 \cdot \nabla H_1 = w_e \tag{30}$$

When $PROD \leq 0$, corresponding to the case of mixed layer shallowing, the mixed layer depth is computed by setting $PROD = 0$ in eq. 28 as

$$H_1 = -\frac{mu_*^3}{1/2g\left[\frac{\alpha Q_s}{\rho_0 C_p} + \lambda S_0\,(E-P)\right]} \tag{31}$$

The thickness of the intermediate layer is then related to the euphotic zone depth, H_e, by the relation

$$H_2 = H_e - H_1 \tag{32}$$

where H_e is determined by the position of the 1% level of the photosynthetically available radiation at the surface for given values of the exctinction coefficients of pure water and living and nonliving substances. Finally, the difference between the upper layer water column depth and the euphotic zone depth yields the thickness of the third layer.

The model is initialized by a horizontally uniform nitrate structure (similar to the one shown in Fig. 5.28a) by specifying the concentrations of 0.1, 1.0 and 6.0 mmol/m3 in the first, second and third layers, respectively. The third layer thus signify the major nitrate pool in the model. The first two layers have initial thicknesses of 20 m, whereas the lowest layer has a thickness of 80 m. The small finite values are assigned initially for all other

state variables of the biochemical model. The model is integrated until all biological fields reache an equilibrium state, which will be independent from the initial conditions and develop solely in response to internal trophodynamic conditions. The transient adjustment is accomplished after two years of integration. The analyses of results here are based on the fourth years of integration.

The basin-averaged mixed layer structure computed by the model is shown in Fig. 5.29. Starting from October, the mixed layer deepens gradually to the maximum depth of aboout 45 m in February at the times of intense vertical mixing associated with the surface cooling, and subsequent entrainment of lower layer waters into the mixed layer. The mixed layer is, on the other hand, shallows abruptly in March due to the onset of the vernal warming. The typical mixed layer depth is 10 m during the summer.

The basin averaged annual plankton distributions within the euphotic zone are shown in Fig. 5.30a-d. The mixed layer (i.e the layer 1) reveals two major enhanced phytoplankton activity during the year (Fig. 5.30a). The first one occurs at the end of the winter mixing and corresponds to the period of abrupt mixing layer shallowing. The abrupt increase of the phytoplankton biomass around at day 160 corresponds with the abrupt MLD changes. The peak biomass of 1.0 mmol/m3 occurs at mid-March, after which the biomass decreases steadily until the end of April. The summer season is characterized by lack of any plankton production within the mixed layer beccause of the absence of sufficient nitrate stocks to maintain the productivity. The begining of autumn corresponds to the period of a secondary phyoplankton production as a result of initiation of vertical mixing, mixed layer deepening and nitrate entrainment from the intermediate layer. The maximum phytoplankton biomass of 0.6 mmol/m3 occurs during the begining of October. The bloom terminates towards the last week of October.

Contrary to the biologically poor mixed layer waters, the intermediate layer confined between the seasonal thermocline and the base of the euphotic zone possesses considerable biological activity during the summer months (Fig. 5.30b). A major bloom is generated during May-June period with a typical basin averaged maximum biomass value of about 0.8 mmol/m3. Two smaller peaks follows this event during the end of July and mid-September. The origin of these blooms will be made clear in the following.

As noted from Fig. 5.30c, ammonium and nitrate are depleted all together within the mixed layer during the summer months. This implies unavailability of nitrate uptake to support the primary production inside the mixed layer. The nitrate concentrations begin to increase gradually after September, as the cooling starts to initiate some mixing within the water column. The nitrate builds up steadily throughout the autumn and early winter, reaching to a typical mixed layer concentration of 0.6 mmol/m3 in January. The nitrate concentrations then increase suddenly and dramatically (up to 2.0 mmol/m3) during February which corresponds to the period of deepest mixed layer formation, vanishing of the second layer (see Fig. 5.29) and entrainment from the nitrogen-rich third layer directly. The nitrate concentrations decrease abruptly in March as they are utilized in the spring pytoplankton production event. The isolated nitrate peaks during the summer and autumn periods in

the layer 2 (Fig. 5.30d) are mostly of the regenerated origin with some contribution due to the vertical diffusion from the subsurface (layer 3) nitrate pool.

According to Fig. 5.30a,b, the major phytoplankton bloom periods are followed by the biomass increases of the zooplankton community. Grazing of phytoplankton right after the autumn bloom event leads to an increase of the zooplankton biomass up to 0.3 mmol/m3. The corresponding increase after the spring bloom is smaller and the basin averaged value is not more than 0.2 mmol/m3.

The basinwide distributions of the phytoplankton in layer 1 during the spring bloom period are shown in Fig. 5.31. The bloom is initiated from the western coast of the basin during March 12, and spreads towards the interior of the basin within the next 6 days. During March 18, the most intense bloom with the biomass of 1.3 mmol/m3 occurs within the relatively quiesent water body of the eastern Black Sea. The bloom tends to weaken towards the periphery of the basin where horizontal advection by the boundary current system reduces the intensity of primary production. The spring bloom persist throught the basin until the end of March, after which it gradually decays all over the basin and terminates during the middle of the following month.

The late spring and summer phytoplankton production taking place within the intermediate layer resembles the March bloom development (Fig. 5.32). The phytoplankton begin to be populated more within the interior basin with a maximum intensity occuring in the center of the eastern part of the sea. While the phytoplankton biomass has relatively uniform distribution within the interior basin, its pronounced variations take place along the western coast and the northwestern region.

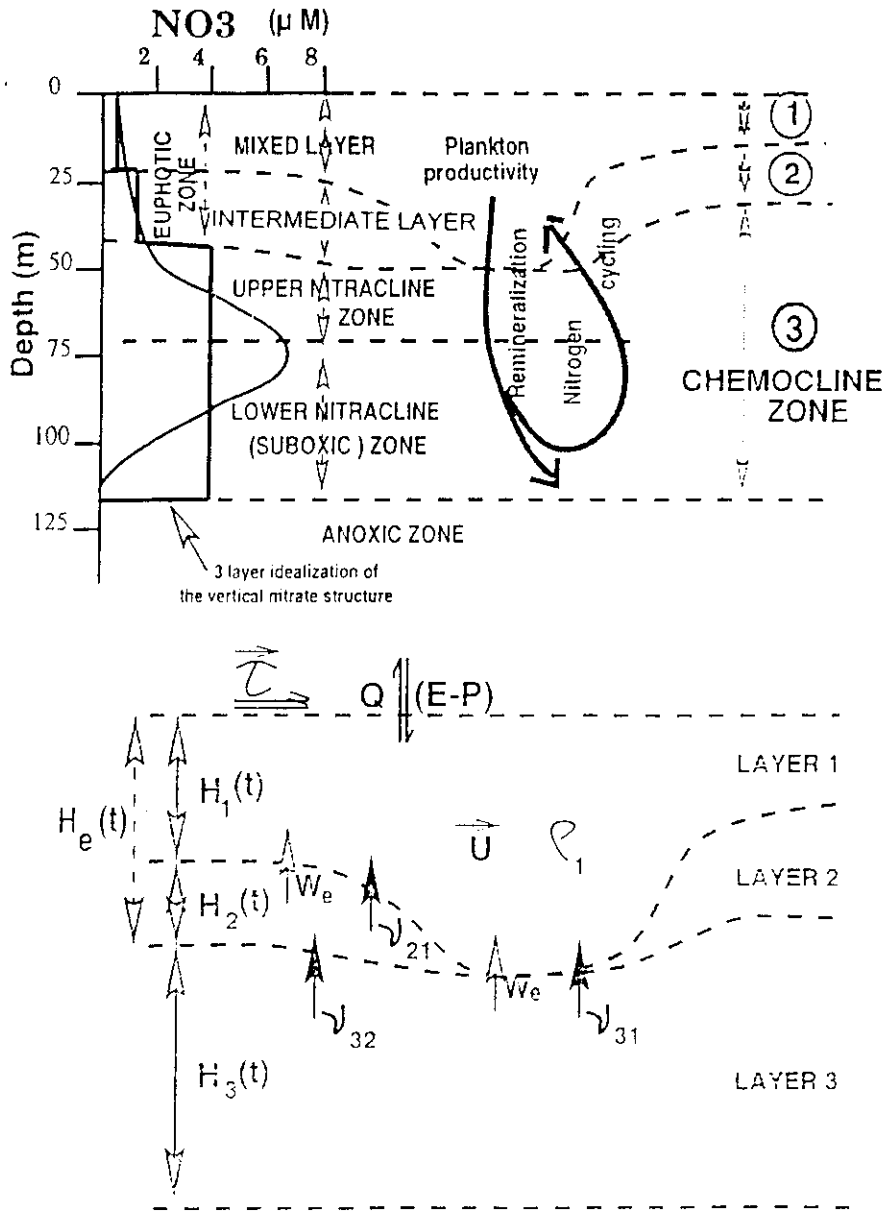

Figure 5.28 (a) Three layer idealization of the Black Sea upper layer biochemical structure, (b) a schematic representation of the model structure.

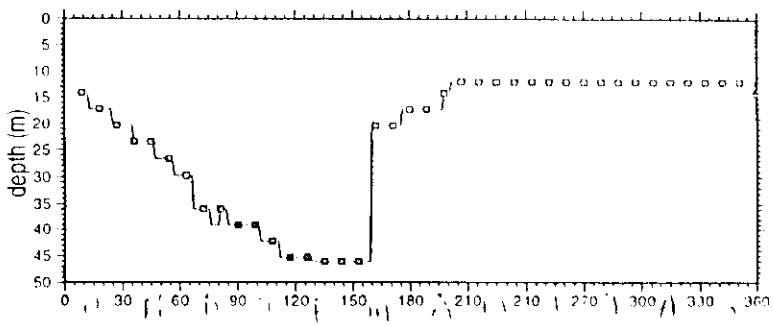

Figure 5.29 The basin-averaged annual cycle of the mixed layer variations.

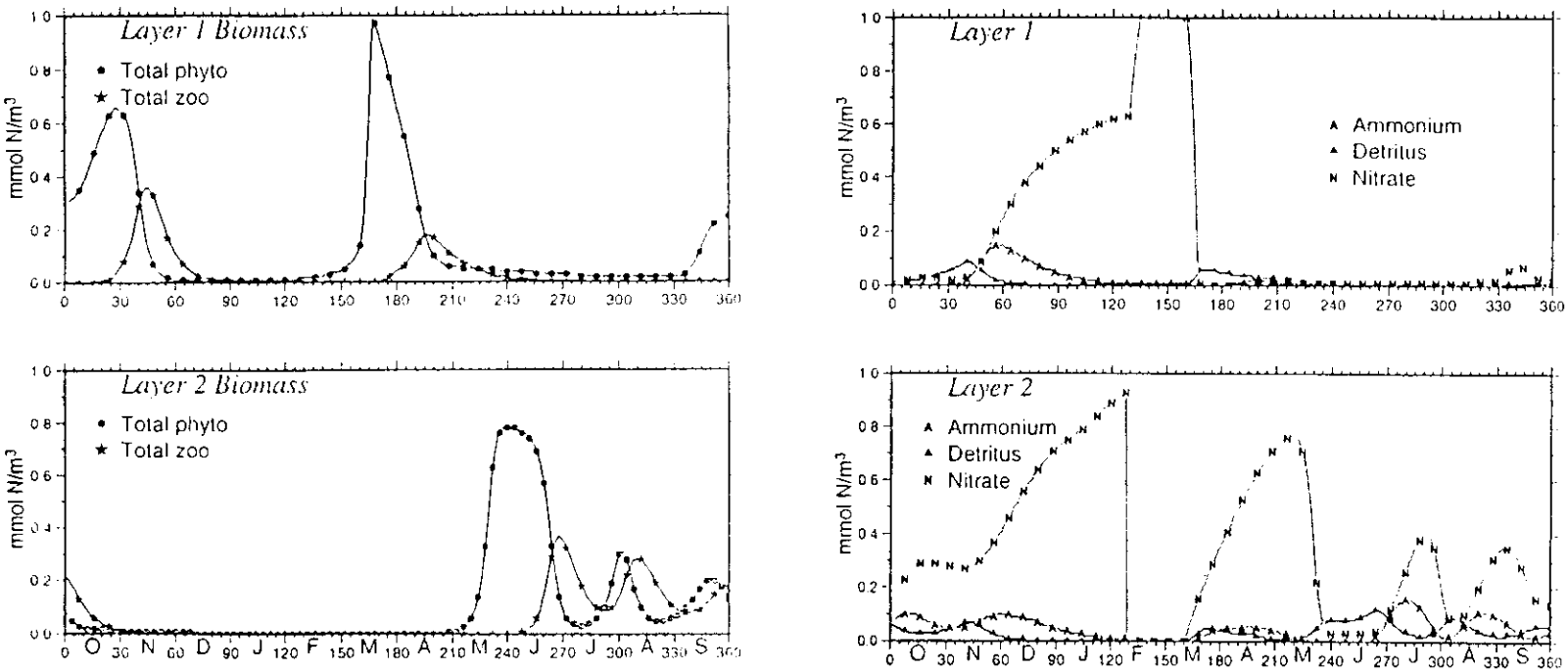

Figure 5.30 Basin averaged distributions of the total phytoplankton and zooplankton biomasses in the layer 1 (a), in the layer 2 (b), and of the detritus, ammonium and nitrate in the layer 1 (c), in the layer 2 (d).

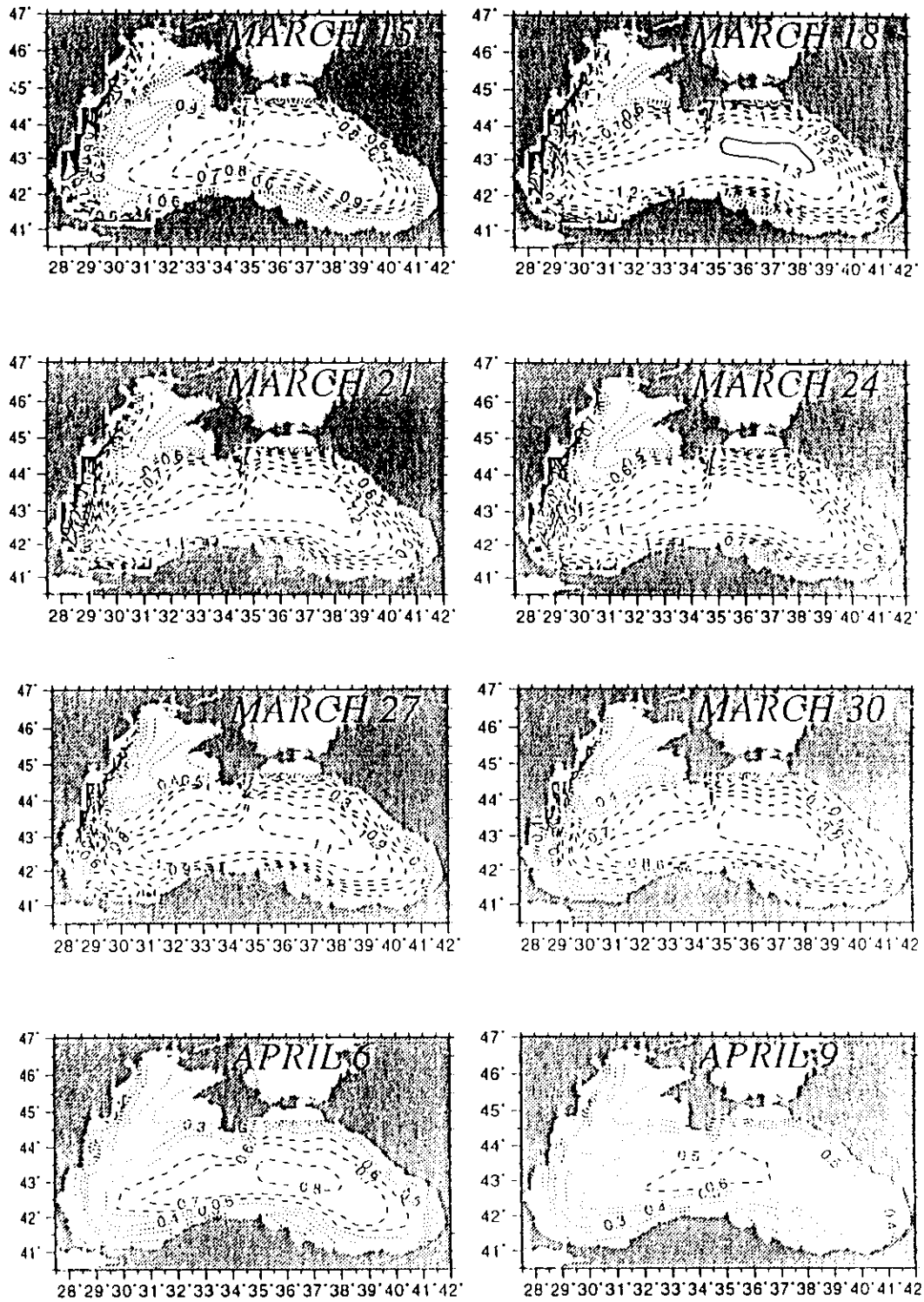

Figure 5.31 Basinwide distributions of phytoplankton biomass at layer 1 during the early spring bloom event.

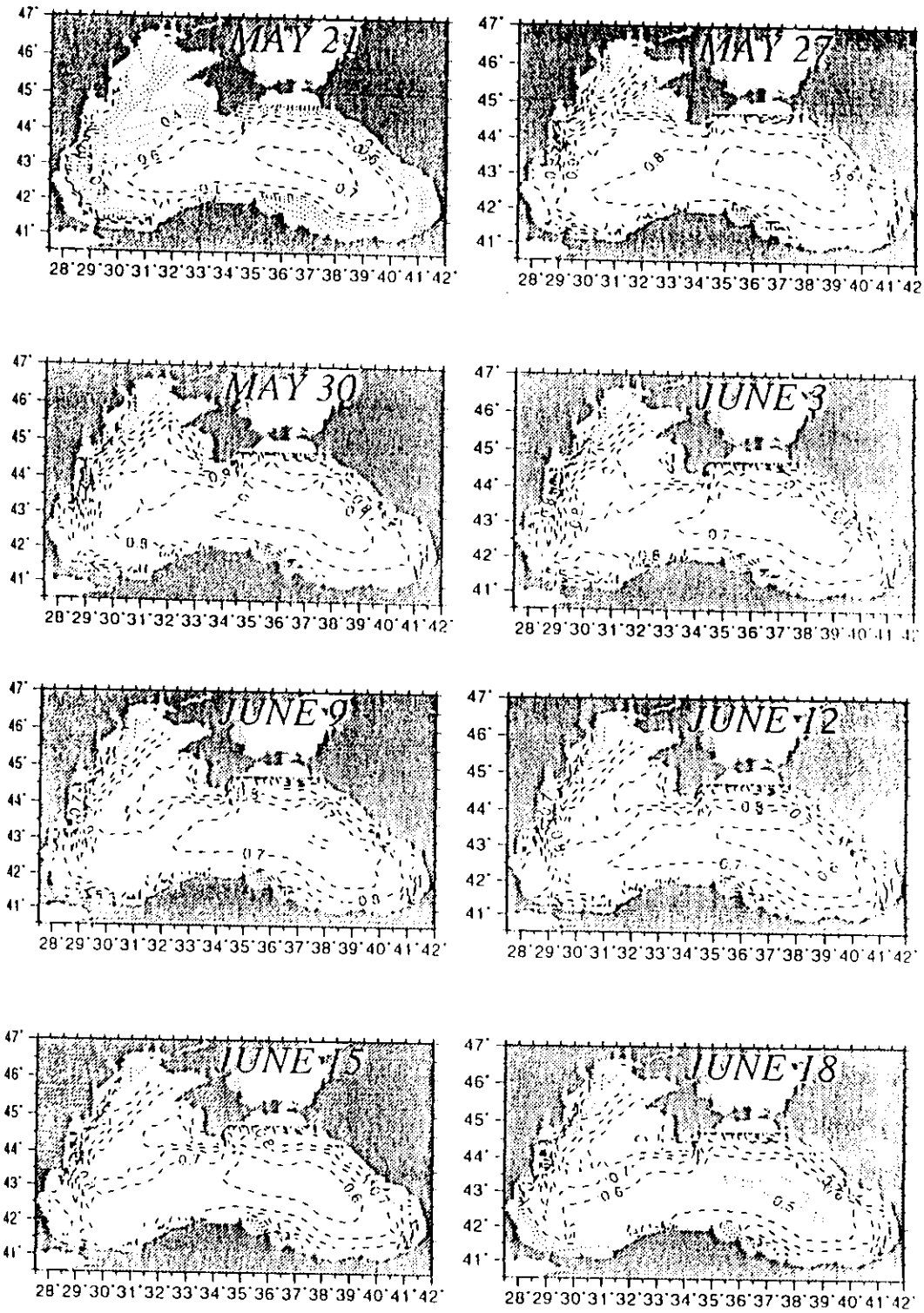

Figure 5.32 Basinwide distributions of phytoplankton biomass at layer 2 during the late spring-early summer bloom event.